COLLOIDAL PHOTONICS OF SEMICONDUCTOR NANOCRYSTALS: FROM POLARIZED COLOR CONVERSION TO EFFICIENT SOLAR CONCENTRATION

A DISSERTATION SUBMITTED TO

THE GRADUATE SCHOOL OF ENGINEERING AND SCIENCE

OF BILKENT UNIVERSITY

IN PARTIAL FULFILLMENT OF THE REQUIREMENTS FOR

THE DEGREE OF

DOCTOR OF PHILOSOPHY

IN

ELECTRICAL AND ELECTRONICS ENGINEERING

By

Kıvanç Güngör

July 2018

COLLOIDAL PHOTONICS OF SEMICONDUCTOR NANOCRYSTALS: FROM POLARIZED COLOR CONVERSION TO EFFICIENT SOLAR CONCENTRATION

By Kıvanç Güngör

July 2018

We certify that we have read this dissertation and that in our opinion it is fully adequate, in scope and in quality, as a dissertation for the degree of Doctor of Philosophy.

Hilmi Volkan Demir(Advisor)

Fatih Ömer İlday

Mehmet Selim Hanay

Sefer Bora Lişesivdin

Emre Sarı

Approved for the Graduate School of Engineering and Science:

Ezhan Karaşan
Director of the Graduate School

ABSTRACT

COLLOIDAL PHOTONICS OF SEMICONDUCTOR NANOCRYSTALS: FROM POLARIZED COLOR CONVERSION TO EFFICIENT SOLAR CONCENTRATION

Kıvanç Güngör
Ph.D. in Electrical and Electronics Engineering
Advisor: Hilmi Volkan Demir
July 2018

Effective photon management is pivotal to the success of future photonic applications. The demand for high-performance electronic displays and solar light harvesters has been increasingly growing, ever with high expectations in advancing their power efficiencies. Semiconductor nanocrystals are highly promising for use in such advanced photonic applications. However, conventional device architectures and fabrication methods cannot fully exploit their potential. To address the need for their effective utilization, in this thesis, we proposed and demonstrated novel photon managing methods for colloidal nanocrystals to target polarized color conversion and efficient solar concentration. Nanocrystals possess an unmatched color purity for next-generation displays but color enrichment in displays suffers from the inherent random polarization in their photoluminescence. Instead of clipping the undesired polarization, we show a new class of v-shaped backlight unit (v-BLU) creating Fano resonances to enforce isotropic quantum emitters of the integrated color-conversion nanocrystals to emit polarized light. While enabling a front-panel configuration, the proposed v-BLU of nanocrystals allows for a strong modification of the density of optical states via resonance coupling. This control over the density of states for isotropic quantum dots empowers the realization of high polarization contrast ratios while sustaining their optical transmission. Similar to color conversion, colloidal nanocrystals are also instrumental to light harvesting, in particular using atomically flat nanocrystals with their step-like absorption profile making them potentially ideal candidates for luminescent solar concentrators (LSCs). Nevertheless, practically zero Stokes shift in their photoluminescence fundamentally limits their utilization. Here we overcame this limitation by proposing the doping of such colloidal quantum wells inducing a large Stokes shift with near-unity photoluminescence quantum efficiency. We developed and demonstrated high-performance LSC panels of the copper-doped

quantum wells outperforming the LSCs of their undoped counterparts and doped quantum dots. The LSCs of such Cu-doped quantum wells offer record optical flux gain compared to other colloids. We believe that the findings presented in this thesis will advance the applications of colloidal nanocrystals boosting the performance of their next-generation photonic devices to unprecedented levels.

Keywords: Semiconductor nanocrystals, colloidal quantum dots, colloidal quantum wells, nanoplatelets, photon management, color conversion, polarized light generation, light harvesting, luminescent solar concentration.

ÖZET

YARIİLETKEN NANOKRİSTALLERİN KOLOİDAL FOTONİĞİ: POLARİZE RENK DÖNÜŞÜMÜNDEN VERİMLİ GÜNEŞ IŞIĞI YOĞUNLAŞTIRILMASINA

Kıvanç Güngör
Elektrik ve Elekronik Mühendisliği, Doktora
Tez Danışmanı: Hilmi Volkan Demir
Temmuz 2018

Etkili foton yönetimi gelecekteki fotonik uygulamaların başarısı için çok önemlidir. Yüksek performanslı elektronik ekranlar ve güneş ışığı toplayıcılarına yönelik talep, özellikle güç verimliliğini artırmaya yönelik yüksek beklentilerle, birlikte giderek artmaktadır. Yarı iletken nanokristaller, bu tür gelişmiş fotonik uygulamalarda kullanım için oldukça ümit vericidir. Ancak, geleneksel cihaz mimarileri ve üretim yöntemleri bu nanokristallerin potansiyellerini tam olarak kullanamamaktadır. Etkili kullanım gereksinimini karşılamak amaçlı, bu tezde polarize renk dönüşümü ve verimli güneş konsantrasyonunu hedefleyen koloidal nanokristaller için yeni foton yönetme yöntemlerini önerdik ve gösterdik. Nanokristaller, yeni nesil ekranlar için eşsiz bir renk saflığına sahip olmakla birlikte, görüntülerdeki renk zenginliği, kuantum noktacıkların rasgele polarizasyona sahip fotolüminesansından muzdariptir. İstenmeyen polarizasyonu kesmek yerine, tümleşik renk dönüştürücü nanokristallerin izotropik kuantum yayıcılarını polarize ışık yaymaya zorlayan, Fano rezonansları yaratan yeni bir sınıf v-şekilli arka ışık birimi (v-BLU) gösterdik. Ön panel konfigürasyonuna imkan verirken, önerilen v-BLU nanokristalleri, rezonans eşleşmesi yoluyla optik durum yoğunluğunun kuvvetli bir modifikasyonunu mümkün kılmaktadır. İzotropik kuantum noktacıklarının durum yoğunluğu üzerindeki bu kontrol, optik iletimlerini sürdürürken yüksek polarizasyon kontrast oranlarının elde edilmesini sağlar. Renk dönüşümüne benzer şekilde, koloidal nanokristaller ışıyan güneş ışığı yoğunlaştırıcılarında (LSC'ler) kullanım için oldukça etkilidir. Özellikle basamak benzeri soğurma profiline sahip atomik olarak düz nanokristaller, LSC'ler için potansiyel olarak ideal adaylardır. Bununla beraber, fotolüminesanslarında pratikte sıfır olan Stokes kaymaları, kullanımlarını sınırlandırmaktadır. Bu sınırlamanın, %100'e yakın bir fotolüminesans kuantum verimliliği ile büyük bir Stokes kayması sağlayan koloidal kuantum kuyucuklarının katkılanması yoluyla

üstesinden geldik. Geliştirdiğimiz bakır katkılı kuantum kuyucuklarından yapılan LSC panellerinin, katkısız muadillerinin ve katkılı kuantum noktacıklarının LSC'lerinden daha yüksek performanslı olduğunu gösterdik. Bu tür bakır katkılı kuantum kuyucuklarının LSC'leri, diğer koloidlere kıyasla rekor düzeyde optik akı kazancı sunmaktadır. Bu tezde sunulan bulguların, yeni nesil fotonik cihazların performansını daha önce görülmemiş seviyelere taşıyacak koloidal nanokristallerin uygulamalarını ilerleteceğine ve geliştireceğine inanıyoruz.

Anahtar sözcükler: Yarıiletken nanokristaller, koloidal kuantum noktacıkları, koloidal kuantum kuyucukları, nanolevhacıklar, foton yönetimi, renk dönüşümü, polarize ışık üretimi, ışık hasadı, ışıyan güneş ışığı yoğunlaştırılması.

Acknowledgement

First, I would like to thank my advisor Prof. Hilmi Volkan Demir. It was 2008 summer when I first met with Prof. Demir trying to introduce myself as a fellow Ankara Science High School graduate and I was impressed with his passion and excitement about his research. Looking back after ten years, I can clearly say that it was a life-changing moment for me. I was enthusiastic to achieve greater things and lucky to have a mentor like him who has been a great role model and visionary scientist. I hope that I have learned a lot from him and I would like to express my sincere gratitude to him for his positive attitude.

I would like to thank my thesis monitoring committee members Prof. Fatih Ömer İlday, Asst. Prof. Selim Hanay and Prof. Ayhan Altıntaş for their support and valuable discussions. I would like to sincerely thank my jury members Prof. Sefer Bora Lişesivdin and Asst. Prof. Emre Sarı for serving in my Ph.D. jury and for their comments and suggestions. I would like to also thank Prof. Orhan Aytur, Prof. Dönüş Tuncel and Prof. Özay Oral for their support during my Ph.D. and Prof. Sergey V. Gaponenko and Asst. Prof. Sedat Nizamoğlu for their support during my postdoctoral position applications.

I would like to acknowledge and thank TUBİTAK-BİDEB for the financial support throughout this thesis.

Ph.D. is a team work and I had the best team; I would like to thank my brothers and sisters from Office 306: Emre Ünal, Özgün Akyüz, Dr. Yusuf Keleştemur, Dr. Burak Güzeltürk, Dr. Can Uran, Dr. Talha Erdem, Dr. Zeliha Soran Erdem, Dr. Aydan Yeltik, Onur Erdem and Dr. Murat Olutaş for all the fun and friendship. My deepest gratitude goes to Dr. Manoj Sharma who has been a friend and mentor to me. I also thank past and present Demir Group members: Dr. Sedat Nizamoğlu, Dr. Evren Mutlugün, Dr. Emre Sarı, Dr. Rohat Melik, Dr. Ahmet Fatih Cihan, Dr. Urartu Özgür Şafak Şeker, Dr. Nihan Kosku Perkgöz, Dr. Pedro Ludwig Hernandez-Martinez, Dr. Vijay Kumar Sharma, Ashma Sharma, Dr. Savaş Delikanlı, Dr. Tuncay Özel, Dr. İlkem Özge Özel, Dr. Akbar Alipour, Berkay Bozok, Halil Akcalı, İbrahim Akcalı, Cüneyt Eroğlu, Dr. Onur Akın, Dr. Mustafa Akın Sefünç, Yasemin Coşkun, Dr. Sayım Gökyar, Dr. Veli Tayfun Kılıç, Dr. Refik Sina Toru, Hatice Ertuğrul, Dr. Durmuş Uğur Karatay, Ozan

Yerli, Didem Dede, Shahab Akhavan, Nima Taghipour, Togay Amirahmadov, Can Fırat Usanmaz, Dr. Negar Gheshlaghi, Dr. Volodymyr Sheremet, Dr. Yemliha Altıntaş, Muhammad Hamza Humayun, Selim Bozdoğan, Farzan Shabani, Ulviyya Quliyeva, Mustafa Sak and İbrahim Tanrıöver. I strongly believe that Dr./non-Dr. ratio in this list will tremendously increase in the near future. Also, Birsen Bilgili deserves a special thank for taking care of us and delicious organizations.

I thank all the technical and administrative staff at UNAM, Advanced Research Labs and EEE Department, especially Mürüvet Parlakay, Duygu Kazancı, Ayşegül Torun, Mustafa Doğan, Mustafa Güler and Murat Güre, who made everything easier.

There is no way I can truly express my gratitude to my parents -Aynur and Mehmet- and my brother İnanç. I have the best family one can imagine, and their support is invaluable. I am fortunate to have a brother that knows and understands me better than anyone else, I hope that our fun never ceases.

Finally, my special thanks go to my lovely wife, Yasemin. I also would like to thank my family-in-law for their support and sharing Yasemin with me. She is the joy and color of my world. In my M.S. thesis, I had written “I miss our undergraduate years a lot, yet too excited to see forthcoming years.”, now, after all these years, I am more excited than ever. Together with her, we are the best team and our journey just began.

This thesis is dedicated to my Yasemin.

Contents

List of Figures

Chapter 1

Introduction

Photonics is an enabling tool in numerous field of applications. Among them, one of the most important is the field of electronic displays. The growing demand for high color purity, high-resolution and high-brightness electronic displays is a driving force in photonics research for displays. Color quality and comfort requirements of future displays cannot be achieved with current lighting technologies. Increasing energy demand and environmental concerns require efficient photonic solutions. To this end, colloidal semiconductor nanocrystals offer key potential solutions to reach these targets. Three decades of research in semiconductor nanocrystal [1] resulted in colloidal quantum emitters having near-unity efficiency, [2] high stability [3]–[5], and strongly tailorable emission characteristics. [6] Organic synthesis routes allow to tune the size, the shape, the composition and the structure of colloidal nanocrystals. Effective utilization of the quantum confinement effects at nanoscale in semiconductor nanocrystals is instrumental to control optical and electrical properties.

Color conversion in electronic displays is the first successful large-scale commercial application of nanocrystals. [7]–[9] Unlike phosphors with spectrally broadband

photoluminescence, colloidal nanocrystals offer very narrow emission enriching color purity and boosting spectral energy efficiency in electronic displays. Nevertheless, conventional architecture in electronic displays for the integration of color converters cannot exploit fully the potential of nanocrystals. Existing nanocrystal-based color-converting displays have similar architectures with the conventional phosphor-based displays. Liquid crystal displays require linearly polarized light coming from the backplane. Polarization state of this linearly polarized light can be controlled by liquid crystal cells. Therefore, a rear polarizer at the back clips the undesired polarization state if the backlight illumination is unpolarized. In this way, each liquid crystal cell provides switching capability for each individual pixel. The process of eliminating the undesired polarization of the randomly polarized back illumination naturally wastes half of the generated light.

Randomly polarized light generation is inherent to isotropic colloidal quantum dots having spherical shape. In this thesis, we propose and show that such isotropic nanocrystal emitters coupled to a special patterned surface are forced to radiate polarized light by modifying their density of optical states. On our designed and fabricated structure, one polarization state is favored by Fano resonance coupling. Modifications in the emission kinetics of these nanocrystals were monitored with time-resolved fluorescence measurements and the emission dipole orientation were observed with back focal plane imaging. Experimental observation of highly polarized emission into the farfield encouraged us to realize a proof-of-concept display demonstration using our nanocrystal architecture as the back-illumination source.

Similar to the growing demand for densely populated city centers with a growing number of consumers accessing high-technology products have increased the energy demand and costs tremendously and are now in need of energy solutions. Photovoltaics is one of the best environmental-friendly solutions for energy generation. However, high-power generating "solar farms" require very large areas which cannot be found near the densely populated city centers and rooftop installations of photovoltaic cells are not sufficient. [10] Luminescent solar concentrators (LSCs) offer a remedy to convert all windows and building façades into electrical power generators at reduced costs without disturbing the aesthetics of buildings. Incorporated with luminescent particles having preferably zero self-absorption of their emission, LSCs are semitransparent panels and may be the key technology for the envisioned zero-energy buildings concept. LSCs were first proposed over four decades ago [11] and since then, a variety of different emitters have been tested to create high-performance LSCs including dyes, phosphors and fluorescent proteins. Among these materials, inorganic semiconductor nanocrystals have the potential to provide the best stability and optical performance that can lead to the commercialization of LSCs. [12]–[14] A good LSC emitter should feature nearly zero absorption around the photoluminescence while being very strong across most of the solar spectrum. Among different nanocrystals, atomically flat ones, commonly known as colloidal quantum wells (CQWs) are ideal LSC materials thanks to their step-like absorption spectrum inherent to one-dimensional quantum confinement. However, this step-like absorption profile coincides with almost zero Stokes-shifted emission spectrum in CQWs. In this thesis, we employed copper doping in CQWs to artificially induce a large Stokes shift and reduce the reabsorption losses. The Cu-doping also increases the spectral matching of the emission with the peak power conversion efficiency of silicon

photovoltaic cells, which in turn increases the overall efficiency. We characterized the reabsorption losses and our findings enabled prediction of the efficiency levels of LSC panels. Characterization of our fabricated LSCs showed that copper-doped CQWs outperform undoped CQWs and doped quantum dots, which is a benchmark prior to our work for the doped nanocrystals.

In this thesis, we studied and demonstrated innovative techniques to engineer photon management using colloidal semiconductor nanocrystals. Here, plasmonically coupled emission of isotropic quantum dots is shown to be an effective way of generation polarized light, which is critical for efficient electronic display operation. Also, we showed that copper doping in CQWs creates an instrumental material class for LSC emitters which can pave the way for high power conversion efficiency LSCs and realization of environmental friendly zero-energy buildings.

1.1 Organization of the thesis

This thesis work is organized as follows:

In Chapter 2, we introduce the basic concepts and physics required to realize this thesis with examples of various semiconductors, quantum confinement effects and plasmonics.

Chapter 3 presents the fabrication and characterization techniques used throughout the thesis work. Fabrication techniques on patterning and etching methods are explained and characterization techniques are introduced through electron-beam and optical imaging methods. Also, information on back focal plane imaging, which is an important

method to identify dipole orientations of quantum emitters, along with its experimental setup and underlying physics is given.

In Chapter 4, we presented our results on polarized color conversion of isotropic semiconductor quantum dots coupled to our designed plasmonic surface. Working principle, fabrication steps and optical characterizations are provided. Using our designed structure, a proof-of-concept display application is demonstrated. This study is a successful output of a Global Research Outreach program project supported by Samsung.

In Chapter 5, we demonstrated that copper-doping is a useful method to utilize step-like absorption profile of two-dimensional colloidal nanocrystals in luminescent solar concentrators. Without altering absorption characteristics, we introduced highly Stokes-shifted emission and fabricated luminescent solar concentrator panels showing promising efficiency values.

Finally, in Chapter 6, we make concluding remarks and give a future outlook related to this thesis.

Chapter 2

Basics

In this chapter, we will briefly explain the basic physics behind the research work presented in this thesis. To understand the properties of colloidal semiconductor nanocrystals, first we will explain what semiconductor is and discuss the necessary conditions to make a material semiconductor. Then we will review the solutions of the simplest quantum mechanical problems to understand quantization effects observed in nanocrystals. It is possible to obtain different shapes of nanocrystals having anisotropic quantum confinement, and dimensionality of the quantum confinement significantly changes the properties of semiconductors. We will derive three-dimensional to zero-dimensional density of states to differentiate the dimensionality effects. After discussing possible advanced heterostructures of colloidal nanocrystals on the foundations of the given concepts in semiconductor physics, we will finally introduce the theory of plasmonic interaction between metallic structures and quantum emitters to understand possible enhancement mechanisms for plasmon-coupled quantum emitters, as presented in this thesis.

2.1 Semiconductors

The basic understanding of band formation in semiconductors requires quantum mechanical calculations of an electron. In this section, we will briefly introduce the band formation mechanism and the related basic semiconductor properties. For this reason, we start with the time-independent Schrödinger equation for a free electron having mass m. The solution gives a well-known parabolic relation between the electron's energy (E) and its wavenumber (k) as $E = \hbar^2 k^2/2m$. Unlike ideal free electron model, an electron in a semiconductor always "feels" the presence of a potential especially in the vicinity of an atom. Attractive potentials for electrons can have various forms, however, the simplest potential barrier is taken to be infinite, resulting in an infinite well for bounded particles, which will be briefly explained in the next section. In an infinite potential well, the energy levels of an electron are discretized by the square of integer steps. If the potential barriers become finite, electron acts like in an infinite well inside the potential well with slight tunneling into the barriers. Above the barrier, although there is a probability of scattering at the barrier, it is similar to a free electron. A crystalline structure, which contains an ordered stacking of many atoms, can be approximated as a periodic array of finite square potential wells using the Kronig-Penny model, which is a reasonable assumption for atomic potentials. In this periodic potential, electron is quasi-free particle implying that it has a parabolic energy dependence similar to that of a free electron, however, its energy dispersion curve is not continuous. Forbidden regions between these allowed energy states open up bandgaps for electrons. Even with this simple approach, we can obtain a basic understanding of the crystalline structure band formation. By using more advanced formalisms such as ***k•p*** band theory, pseudopotential

and *ab initio* calculations, it is possible to compute and predict the band diagrams of different materials.

Using the relation between the energy and the wavenumber ($E = \hbar^2 k^2 / 2m$), we can assign an effective mass (m_{eff}) for each band as:

$$m_{eff} = \left(\frac{1}{\hbar^2} \frac{\partial^2 E}{\partial k^2} \right)^{-1} \quad 2.1$$

The effective mass is an important parameter that defines the main characteristic of an electron in a specific band and it will be required in many calculations in the following parts. In most of the semiconductors, the effective mass of electrons is smaller than the free electron mass, meaning that it is easier for electrons to accelerate in a semiconductor.

Electrons, being fermions, obey the Fermi-Dirac distribution and the electron concentration inside a solid strictly determines its Fermi level. A change in the Fermi level significantly modifies the material properties. As illustrated in Figure 2.1, the Fermi level dictates the lowest energy state that an electron can occupy and, according to this level, a material can become insulator, metal, semimetal, or semiconductor. While an insulator does not allow any electron movement under electric field, a metal allows for electron movement even at absolute zero. The difference between a semimetal and semiconductor comes from this absolute zero behavior: a semiconductor becomes an insulator at absolute zero, but semimetal can still transfer electrons. Also, increasing the temperature of a semiconductor increases its conductivity in contrast with metals. This

difference was one of the first observations for semiconductors as a new class of materials.

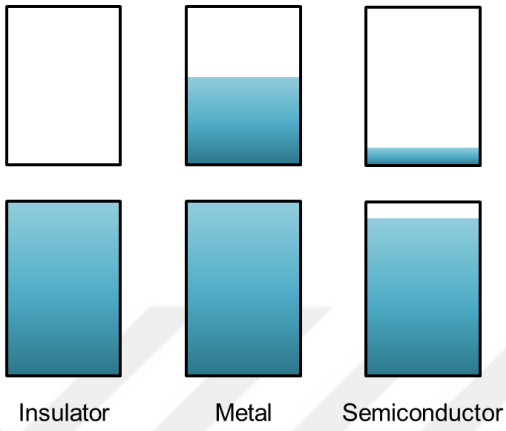

Figure 2.1 Illustration of the band filling for different types of materials.

In semiconductors, the lowest unoccupied molecular orbit and the highest occupied molecular orbit are known as the valence and conduction bands, respectively. At this point, we introduce a pseudoparticle called “hole” for the deficiency of an electron to simplify the understanding and make calculations easier. Holes are also fermions and obey the Fermi-Dirac statistics. Their energy increases in the negative direction of electrons and holes have their own effective masses, typically much larger than the electrons. In comparison to Figure 2.1, a more realistic band structure of a direct bandgap semiconductor is shown in Figure 2.2. While there is only one conduction band with two-fold degeneracy due to spin, the valence band structure consists of three different bands. Inside the semiconductor, interacting electron and hole create a hydrogen-like pseudoparticle called exciton. Excitonic interaction significantly changes the absorption and emission kinetics depending highly on the dimensionality of the semiconductor.

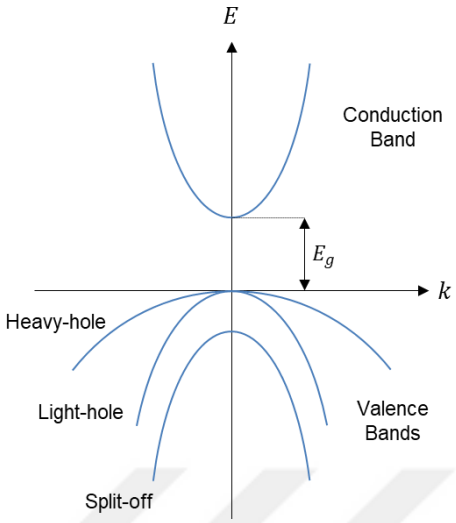

Figure 2.2 A more realistic band structure of a direct bandgap semiconductor.

Heating can increase the conductivity of semiconductors. Also, depending on the semiconductor bandgap, another approach to control the conductivity of a semiconductor is to apply a potential difference across the material to create electric field inside the material. This capability to switch the material conductivity can be considered as one of the milestones for today's semiconductor technology. By making a junction with different Fermi-level structures having similar bandgaps, it is possible to create a built-in electric field inside the material and control the electrical conductivity of the material with the applied potential from outside. Changing the Fermi level is possible via doping with various atoms in semiconductors. Doping with electron deficient materials is used in p-type doping and electron rich dopants, in n-type doping.

Fermi level dictates the material type; however, the electronic structure of materials also depends on the density of electronic states. In the quantum confinement regime, the density of states changes dramatically. In Section 2.3, we present the calculations for different dimensionalities of confinement.

2.2 Understanding Quantum Effects

At the end of 19th century, many observations remained unexplained with classical mechanics. The discoveries of electron and its bizarre wave-particle duality in addition to the discovery of wave-particle duality of light can be considered as the dawn of quantum mechanics. Later, many experiments strongly confirmed that unlike the predictions of classical mechanics, nature is quantized. Many new quantized particles are introduced theoretically and observed experimentally. Schrödinger equation provides the basic toolkit for quantum mechanics. Under constant potential V, a particle with mass m is subject to:

$$-\frac{\hbar^2}{2m}\frac{d^2\psi}{dx^2} + V\psi = E\psi \tag{2.2}$$

For a free electron, we take $V = 0$ since the potential is a relative quantity, we end up with $E = \hbar^2 k^2/2m$ as we presented in the previous section. The general solution of this equation is:

$$\psi = A\sin kx + B\cos kx \tag{2.3}$$

This general solution can be interpreted as the summation of stationary waves, which implies that the electron represented in this solution is everywhere. For physical problems with proper boundary conditions this picture will change.

In this thesis, we showed device applications of semiconductor nanocrystals and, as we discussed, many novel properties of these nanocrystals originate from the quantum confinement. Here we start with an infinite square well problem, which is the most basic derivation of quantized energy levels. This is analogous to Fabry-Perot cavity for electromagnetic waves. Instead of a refractive index difference, there is a potential barrier. For an infinite square well having a well width L, discrete energy levels are characterized by an integer $n = 1, 2, 3, ...$

$$E_n = \frac{n^2\pi^2\hbar^2}{2mL^2} \tag{2.4}$$

When we apply the infinite potential boundary conditions to the free electron, the wavefunction solutions become:

$$\psi_n(x) = \frac{\sqrt{2}}{L}\sin\left(\frac{n\pi}{L}x\right) \tag{2.5}$$

The first three energy levels and their corresponding wavefunction functions are illustrated in Figure 2.3 (left panel). Even the ground state has nonzero a energy and the wavefunctions are exactly zero at the potential barriers. An important result of the infinite well problem is the successful illustration of quantum confinement on the energy level separation: E_n is inversely proportional to the square of the well width. Narrower the well, higher the separation energies. This dependence is a direct consequence of quantum confinement. We observe this behavior with the size effect of nanocrystals:

smaller sizes of quantum dots (QDs) result in larger effective bandgaps, as we will discuss in the following sections.

Although, the infinite square well problem gives insight about the energy discretization, the infinite potential well is rather uncommon. Instead, a finite potential square well is more realistic and provides a good basic understanding on the core/shell heterostructures of nanocrystals. When coated over the core region, a higher bandgap shell creates a potential barrier for electrons and holes in the nanocrystal. The solution of the finite square well problem requires a slightly complicated approach and do not provide any significant understanding here. Instead, we will discuss the outputs of the solution. As shown in Figure 2.3 (right panel), wavefunctions inside the well have similar confined forms as the infinite well. However, above the potential barrier, electrons will be reflected and transmitted with corresponding probabilities, and they will be similar to free electrons. The states that reside within the energy of the well are the bound states and their energy levels change similar to the infinite well problem. Those outside the energy range of the well are the unbounded states.

There are two major observations for the finite well potential: there is always a bound state regardless of the potential depth and the particles always tunnel partially into the barrier. Indeed, the tunneling is another fascinating result of quantum formalism which classical physics cannot explain. Such tunneling of particles is an important concept to understand heterostructures of the semiconductor nanocrystals as well as various semiconductor devices.

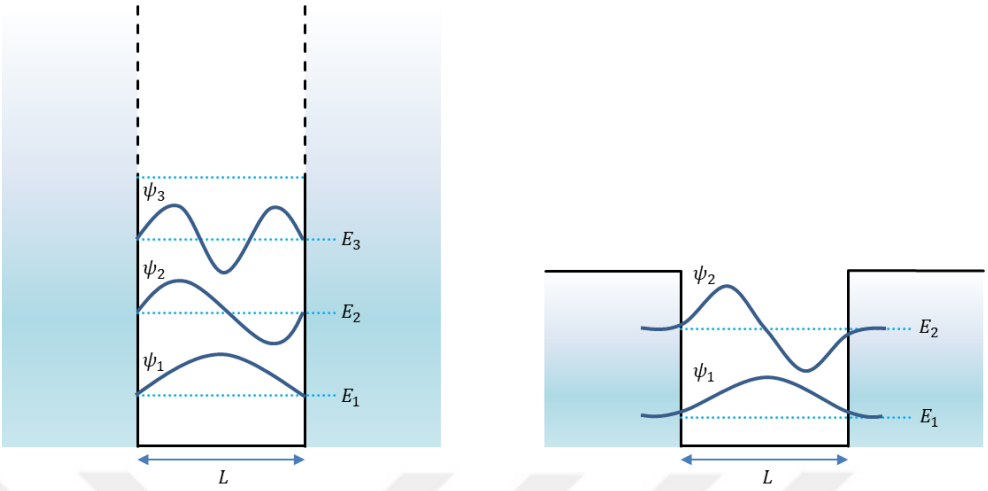

Figure 2.3 Illustration of infinite (left) and finite (right) square potential well problems for a particle with mass.

2.3 Density of States for Electrons and Holes

Absorption and emission processes in quantum emitters can be explained by using Fermi's golden rule. Quantum mechanical absorption rate for each allowed transition between discrete states is given by:

$$W_{i\to j} = \frac{2\pi}{\hbar}|\langle i|H'|j\rangle|^2\delta\left(E_j - E_i - \hbar\omega\right)$$

2.6

For continuum of states observed in semiconductors, Fermi's golden rule becomes

$$W_{i\to j} = \frac{2\pi}{\hbar}|\langle i|H'|j\rangle|^2 g(\hbar\omega)$$

2.7

where $g(\hbar\omega)$ is the density of available states. [15] The unitless term $|\langle i|H'|j\rangle|^2$ is called the oscillator strength related to the strength of the corresponding oscillation among all allowed oscillations in the system. H' is the interaction Hamiltonian between the states i and j. Using Fermi's golden rule for the upward transition (absorption process) and the downward transition (emission process), as a directly measurable quantity, we can calculate absorption coefficient (which is given per length) denoted as α for direct bandgap semiconductors. The difference between the upward and downward transitions per unit number of incident photons gives the net absorption [16]

$$\alpha(\hbar\omega) = \frac{\hbar e^2}{2m_0 c\epsilon_0}\frac{1}{n_r}\frac{E_p}{\hbar\omega}g_j(\hbar\omega)[1-(f_e+f_h)] \qquad 2.8$$

where n_r is the refractive index, E_p is a material parameter that comes from ***k•p*** theory, and $g_j(\hbar\omega)$ is the joint density of states of electron and hole. f_e and f_h are Fermi distributions of electrons and holes at the corresponding energy level and temperature defined as

$$f_e(E,T) = \left(1+e^{\frac{E-\mu}{k_B T}}\right)^{-1}, \qquad f_h(E,T) = 1-\left(1+e^{\frac{E-\mu}{k_B T}}\right)^{-1} \qquad 2.9$$

As stated, the absorption and emission processes of a semiconductor are directly related with the electronic band structure. Changing the carrier concentrations, hence the Fermi levels, can also modify the material properties significantly. It is possible to adjust the carrier concentration by changing the temperature and or by applying external electric

field, which in turn change the chemical potential μ. Under intense electrical or optical pumping, Equations 2.9 change significantly and $1-(f_e+f_h)$ term becomes negative in Equation 2.8, meaning that there is a net optical gain induced in the semiconductor instead of optical absorption. This relation is useful to understand the basic conditions to achieve optical gain in semiconductors.

Using this absorption coefficient and Einstein coefficients, the spontaneous emission rate per unit volume can be found as

$$r_{spont}(\hbar\omega)=\frac{8\pi n_r^2}{\hbar^3 c^2}[\hbar\omega]^2 f_e f_h \alpha(\hbar\omega) \qquad 2.10$$

In both the absorption and emission processes, the density of states has critical importance and strongly depends on the dimensionality of quantum confinement. To understand optical properties of highly confined nanocrystals in different shapes, we need to understand the density states behavior of carriers.

The solution for the density of states requires to work in the reciprocal space under the infinite crystal approximation. Three-dimensional reciprocal space wavevector components for lattice constants a, b and c are

$$k_x=\frac{\pi}{a}, \qquad k_y=\frac{\pi}{b}, \qquad k_z=\frac{\pi}{c} \qquad 2.11$$

In the reciprocal space, the density of states $g(k)$ is defined as $g(k)=dn/dk$. In three-dimensions, n is the number of states per real unit cell volume defined ($V=abc$) as

$$N = \frac{2\Omega}{8k_x k_y k_z} = \frac{Vk^3}{3\pi^2}, \qquad n = \frac{N}{V} = \frac{k^3}{3\pi^2}$$

2.12

where Ω is the octant of the reciprocal space

$$\Omega = \frac{4\pi}{3}k^3$$

2.13

and since the total number of states are fixed, $g(E)dE = g(k)dk$. Using the wavenumber and energy relation for a particle, we have

$$k = \frac{\sqrt{2mE}}{\hbar}, \qquad \frac{dk}{dE} = \frac{1}{\hbar}\sqrt{\frac{m}{2E}}$$

2.14

and the resulting three-dimensional density of states g_{3D} is calculated as

$$g_{3D}(k) = \frac{k^2}{\pi^2}, \qquad \boldsymbol{g_{3D}(E)} = \frac{\sqrt{2m^3(E - E_g)}}{\pi^2\hbar^3}$$

2.15

In bulk form, semiconductors have $1/2$ power dependence on the energy as sketched in Figure 2.4.

The two-dimensional density of states is the case under strong quantum confinement in one dimension. We have a real space unit cell area (A), the quadrant of reciprocal space for calculations and the number of states per unit cell area as follows

$$A = ab, \qquad \Omega = \pi k^2, \qquad N = \frac{2\Omega}{4k_x k_y} = \frac{Ak^2}{2\pi}, \qquad n = \frac{N}{A} = \frac{k^2}{2\pi}$$

2.16

The resulting two-dimensional density of states $g_{2D}(\hbar\omega)$ is give by

$$g_{2D}(k) = \frac{k}{\pi}, \qquad \boldsymbol{g_{2D}(E)} = \frac{m}{\pi\hbar^2}$$

2.17

which is energy independent. Under quantum confinement, each state energy will have abrupt jumps creating a series of step functions as shown in Figure 2.4.

Under the two-dimensional confinement, the one-dimensional density of states can be calculated using unit cell length l and half of the reciprocal space

$$l = a, \qquad \Omega = k, \qquad N = \frac{2\Omega}{2k_x} = \frac{lk}{\pi}, \qquad n = \frac{N}{l} = \frac{k}{\pi}$$

2.18

The one-dimensional density of states is then

$$g_{1D}(k) = \frac{1}{\pi}, \qquad \boldsymbol{g_{1D}(E)} = \frac{1}{\pi\hbar}\sqrt{\frac{m}{2(E - E_g)}}$$

2.19

Equation 2.19 shows the inverse square root energy dependence within and, like $g_{2D}(\hbar\omega)$, here the quantum confinement creates discrete energy states within this inverse square root dependence as shown in Figure 2.4. Finally, the density of states for

the zero-dimensional QDs, g_{0D}, consists of delta functions at the corresponding quantized energies as shown in Figure 2.4.

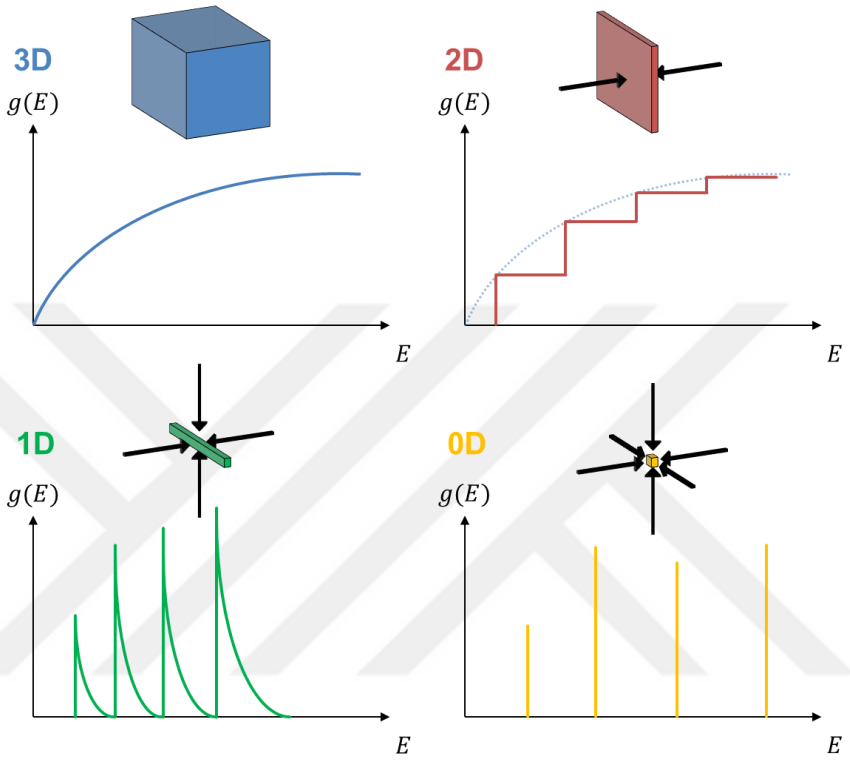

Figure 2.4 Different dimensionalities and their corresponding density of states illustrated from bulk to 0D.

In Figure 2.5, Fermi distributions at the absolute zero and elevated temperatures are illustrated. Since the net absorption coefficient α is a product of $(1 - f_e - f_h)$ and g_j, the change in the number of states with temperature is also shown here. $N(E)$ with respect to E for $T_2 > 0$ K case is quite similar to the absorption tail of semiconductors.

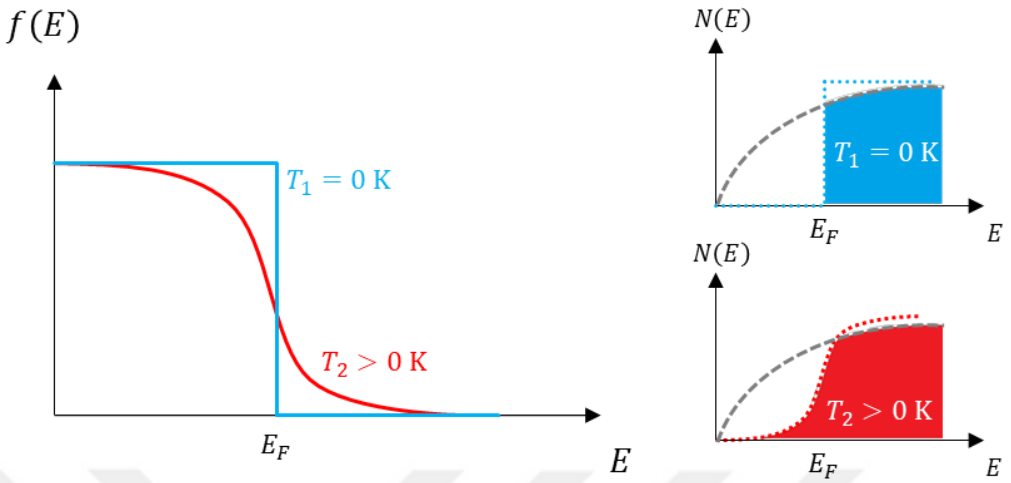

Figure 2.5 The product of Fermi distribution and the density of states determines the absorption profile. The product of $(1 - f(E))$ and the three-dimensional density of states $(g_{3D}(E))$ at $T_2 > 0$ K successfully illustrates a typical absorption tail of a semiconductor.

2.4 Colloidal Semiconductor Nanocrystals

Semiconductor nanocrystals can be obtained using different methods. Before colloidal synthesis of QDs, QDs were obtained in molten glass and their optical properties were correctly attributed to the quantum confinement effects. [17] the first systematic studies have been performed on these quantum confined nanocrystals, however, this method had inherently limited control over the shape, material composition and uniformity of the structures. These initial studies paved the way for semiconductor nanocrystal research and showed promising properties of nanocrystals including strong absorption [18], tunable PL emission even from indirect bandgap materials [19], and strong optical gain performance [20], which attracted attention of researchers and engineers. After the first colloidal synthesis of semiconductor nanocrystals, [1] tremendous research efforts have been made, which allowed for different sizes, various shapes and alloyed compositions of semiconductor nanocrystals. After 30 years of research, the commercialization of

colloidal QDs has created a promising market especially as primary color convertors in electronic displays. [7]–[9] The capability of size and shape control of nanocrystals through solution-processed synthesis methods make advanced heterostructures possible. Zero-dimensional atom-like QDs [1], one-dimensional quantum rods (nanorods) [21], [22] and two-dimensional quantum wells (nanoplatelets) [23] together provide us with an exciting toolbox for nanocrystal research.

In Figure 2.6, the effect of quantum confinement on semiconductor energy band diagram is shown. Unlike a continuous energy band diagram presented in Figure 2.2, the discretization of energy levels allows only certain transitions and due to the sharp curves of conduction and valence bands around the bandgap, the number of possible transitions is limited. This limited number of states require interaction of electrons and holes through the higher energy states, hence effectively leading to an increase in the energy bandgap.

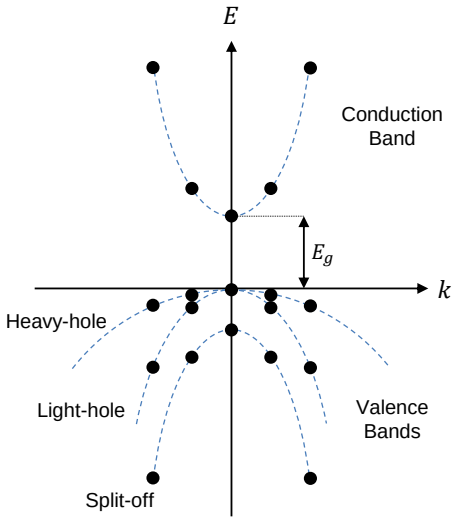

Figure 2.6 Effect of quantum confinement on bulk semiconductor energy band diagram given in Figure 2.2. Quantization restricts only certain k values on the band diagram.

The sizes of nanocrystals is in the order of exciton Bohr radius. Since an exciton is a quasi-particle consisting an electron and a hole, it resembles a hydrogen atom. [24] the 1s orbital energy of hydrogen and its orbital radius (Bohr radius) can be calculated for an exciton in bulk semiconductor as

$$E_{ex} = \frac{1}{4\pi\epsilon_0}\frac{\mu e^4}{2\epsilon^2\hbar^2} \tag{2.20}$$

$$a_B^* = 4\pi\epsilon_0\frac{\epsilon\hbar^2}{\mu e^2}. \tag{2.21}$$

In Equations 2.20 and 2.21, ϵ is the dielectric constant of the semiconductor medium and μ is the reduced effective mass of the electron-hole pair. Under the one-dimensional confinement, E_{ex} and a_B^* take their two-dimensional form related to their three-dimensional values as [25]

$$E_{ex,2D} = 4E_{ex,3D}, \qquad a_{B,2D}^* = \frac{a_{B,3D}^*}{2} \tag{2.22}$$

Four-fold increase in the exciton binding energy is a strong modification for two-dimensional systems and allows to observe strong excitonic features in the absorption spectrum even at room temperature. Generally low exciton binding energies of semiconductors are below k_BT value at room temperature (~26 meV) and cannot be observed in the absorption spectrum. In Chapter 5, colloidal quantum wells will be introduced and their quasi-two-dimensional nature dictates an exciton binding energy

between $E_{ex,2D}$ and $E_{ex,3D}$. Heavy-hole, light-hole and split-off excitonic features are clearly visible in their absorption spectra.

In addition to the size tuning to control the electronic band structure of nanocrystals, heterostructures can add another degree of freedom for the-so-called bandgap engineering. In Figure 2.7, bandgaps and relative positions of the band offsets are shown for commonly used semiconductor compounds. Effective positioning of different materials allows for designing nanocrystals with high stability [3]–[5], enhanced optical gain performance [26], extremely Stokes-shifted emission and increased charge separation [2], [6]. Different combinations of heterojunctions are illustrated in Figure 2.8. According to the barrier height, the localization of electrons and holes varies. Like core-only nanocrystals, the localization of electron and hole in the same core region is referred to as Type I structure. The opposite is also possible when the localization of both carriers occurs in the shell region, which is known as the inverse Type I. When carriers are separated in different regions of the nanocrystal, e.g., electrons in the core and holes in the shell or vice versa, the structure exhibits Type II band alignment. If the barrier is shallow for one carrier allowing to delocalize through the entire structure and the other carrier is strongly localized in one region, the structure is called as quasi-Type II structure. This control over the distributions of the carriers changes the overlap between them and directly effects the oscillator strength. For example, while the oscillator strength is quite strong in Type I structures, this tight confinement in the same region increases the nonradiative Auger recombination losses, creating a killer effect for the optical gain performance. Type II and quasi-Type II band alignments offer a remedy for Auger recombination at a cost of considerably reduced oscillator strength and broadened PL emission. In Figure 2.9, various different types of CdSe quantum well

colloids are shown under ambient and UV illumination exemplifying the possible engineering of the absorption and emission properties of these nanocrystals.

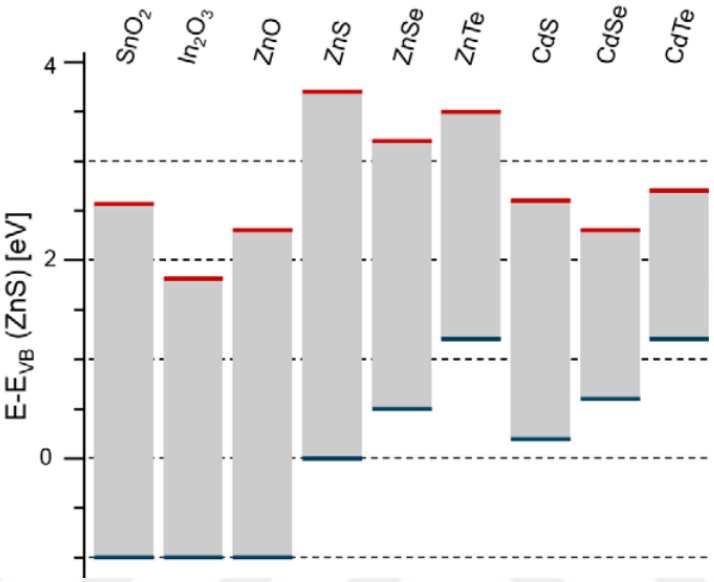

Figure 2.7 Bandgaps and relative band alignments of commonly used semiconductors for colloidal nanocrystals. After [27] © IOP Publishing. Reproduced with permission. All rights reserved.

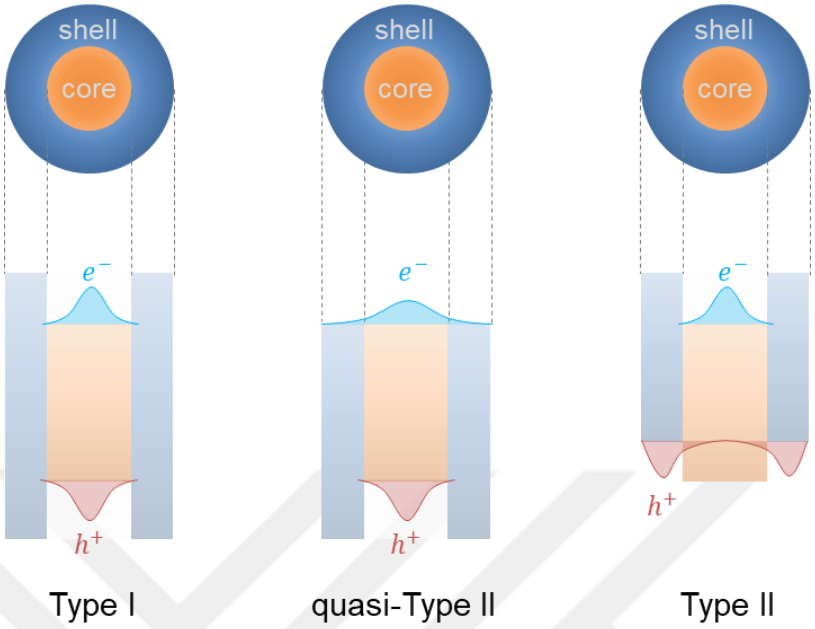

Figure 2.8 Illustration of different types of the band alignments and their corresponding electron and hole wavefunction across the heterostructures of each nanocrystal.

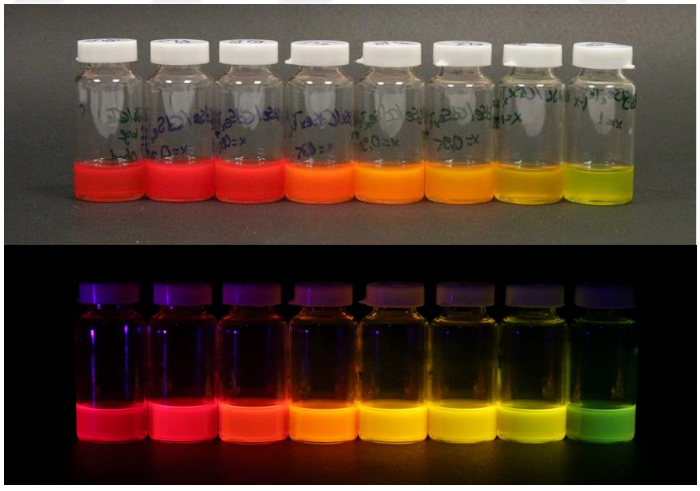

Figure 2.9 Various 4 ML Type I and Type II CQWs under ambient lighting (top) and UV illumination (bottom) showing bright colors all across the visible spectrum from green to red (Demir Group).

2.5 Plasmonics: Colorful Metals of Nanoworld

Semiconductor nanocrystals show novel physical properties at the nanoscale thanks to the quantum confinement. In metals, electrons are nearly free and does not experience periodic potential of ordered atoms as electrons do in semiconductors. Yet, physical properties of metals significantly change at the nanometer scale as well. One of the first observations was the color change in the beaten metallic leaves of gold and silver by Michael Faraday in 1857. [1] This effect was due to the collective oscillations of nearly-free electrons inside the tens of nanometers thick metallic films. Like a plasma, electrons are free to move in a collective oscillation at a frequency called plasma frequency in bulk form. Hence the name plasmon is coined for the quanta of collective electron oscillation in an electron-rich material and plasmonics has become one of the very active fields of nanoscience research. [28] One of the first applications of plasmonic interactions goes back to the 4^{th} century AD. Lycurgus Cup is one of well-known ancient artifacts in plasmonics community, for it can change its color depending on the illumination location. As shown in Figure 2.10, when illuminated from the inside, the cup is red and its color changes to green when illuminated from outside. This is the result of absorption and scattering behavior of the metallic nanoparticles embedded in the glass. Such metallic nanoparticle-incorporated glasses are still being used for stained glass manufacturing but this time we know its underlying physics.

Figure 2.10 The first known example of a plasmonic application: Lycurgus Cup. Dichroic behavior of the glass is originated from the incorporated metallic nanoparticles. © Trustees of the British Museum [29].

Bulk volume plasma frequency (ω_p) of electrons in a metallic structure depends on the number of electrons per unit volume (n) and the effective mass of electron in the material (m_{eff}):

$$\omega_p^2 = \frac{ne^2}{\epsilon_0 m_{eff}} \qquad 2.23$$

Equation 2.23 gives the resulting frequency of the nearly free electron oscillations under the restoring force created from the electric field of electron motion in Drude model. The solution to this restoring force problem comes from a simple harmonic oscillator and it is purely classical. Even though the plasmonic effects can be observed at the nanometric scale, the plasmonic response of metals can be predicted by classical mechanics with high precision. Quantum mechanics is only involved in the density of electrons and

effective mass calculations as well as in geometries when charge tunneling is involved. ω_p can be used to predict macroscopic properties of the plasmonic materials using the dielectric function calculation in Drude model as follows [24]

$$\epsilon(\omega) = \epsilon_\infty - \frac{\omega_p^2}{\omega^2 + i\gamma\omega}$$

2.24

However, the dielectric function given in Equation 2.25 does not take into account the interband contribution for noble metals. [30] A Lorentzian lineshape for the dielectric function can account and model all these contributions for a resonance mode n

$$\epsilon_n(\omega) = \frac{C_n}{\omega_n^2 - \omega^2 - i\gamma_n\omega}$$

2.25

In Equations 2.24 and 2.25, γ is the dephasing factor originated by the lossy behavior of the plasmonic material. C_n is the amplitude and ω_n is the angular frequency for each oscillation in the metal.

Although volume plasmons can explain the electromagnetic response of metals in bulk form, interactions generally occur at the interfaces. Therefore, it is critical to understand the plasmonic response on the surface of metals. Using the dielectric function of metals, it is possible to obtain an electromagnetic field solution at the dielectric-metal interface. This solution is only valid for the TM polarization since the TE polarization cannot satisfy the continuity equation on the interface and the resulting parallel wavevector:

$$k_x = k_{SPP} = \frac{\omega}{c}\sqrt{\frac{\epsilon_1\epsilon_2(\omega)}{\epsilon_1 + \epsilon_2(\omega)}}$$

2.26

where ϵ_1 is the dielectric constant of vacuum or the dielectric environment and $\epsilon_2(\omega)$ is the dielectric function of the metal. In the limit $k_x \to \infty$, the group velocity goes to zero and in this limit, we have a limiting surface plasmon frequency given by

$$\omega_{SP} = \frac{\omega_P}{\sqrt{1 + \epsilon_d}}$$

2.27

Dispersion relations are illustrated in Figure 2.11 for the air-metal and the dielectric-metal interfaces for surface plasmon polaritons (SPP). SPP, being a quasiparticle for interaction with a photon, has a similar dispersion with the transverse branch of phonon polariton. Although we did not include the volume plasmon polariton curve here, it lies above ω_{SP} value and has longitudinal wave nature, which cannot be excited under electromagnetic interaction. The volume plasmon polariton dispersion curve can be measured with electron energy loss spectroscopy measurements. [31] Another observation from the dispersion relation of SPPs is the mismatch between the light line ($\omega = ck/\sqrt{\epsilon}$) and the SPP line obtained from Equation 2.26. Due to negligible momentum of photons, electromagnetic excitation cannot excite SPPs at the same interface. Kretschmann prism configuration is sketched in Figure 2.11 to excite SPPs. The light line of dielectric medium can intersect with the SPP line of the air-metal interface. Impinging light from air side cannot excite SPPs but light coming from the dielectric side at a certain angle can excite SPPs on the air-metal interface. It is important

to emphasize that it is not possible to excite SPPs in the dielectric-metal interface for this configuration. Excited SPPs on the air-metal interface can be characterized by the propagation distance L_{SPP} having a mode wavelength λ_{SPP} [32]

$$L_{SPP} = \frac{2\pi}{2\mathrm{Im}(k_{SPP})}, \qquad \lambda_{SPP} = \frac{2\pi}{\mathrm{Re}(k_{SPP})}$$

2.28

which constitute the decaying and propagating parts of an evanescent waveform, respectively. This evanescent wave confines the incident electromagnetic radiation at the interface and can propagate in micrometers scale range for metals having reduced damping or dephasing factor γ in the dielectric function. [30] The momentum matching condition can be overcame using different methods other than the prism coupling. Gratings and other periodic structures provide the necessary momentum to excite surface plasmons on continuous metallic films. [30] Also a localized disturbance on the smooth metallic film can create the required momentum uncertainty for the SPP creation.

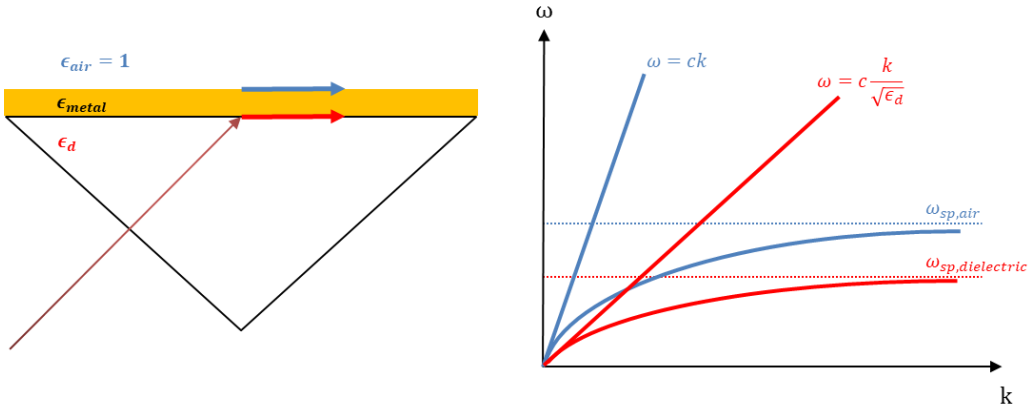

Figure 2.11 Kretschmann prism configuration for creating of SPPs (left) and the dispersion curve illustration (right) for the excitation mechanism.

Another type of plasmonic effect can be seen at nanoscale using isolated metallic nanoparticles, which is commonly known as localized surface plasmons (LSP). In this case, highly localized particles do not require a momentum matching requirement to launch propagating SPPs; instead, electron oscillation is confined into a small volume. Bounded oscillation of coherent electron movement is highly size and shape dependent. Analytical solutions are present for spherical [33] and ellipsoid [34] nanoparticles, but advanced shapes enabled by fabrication and synthesis methods require numerical solutions. [35] Shape and size modifications on metallic nanoparticles significantly change their physical and chemical properties. [36] For particle sizes smaller than the skin depth of corresponding metals, electrons experience almost no retardation effect during the oscillations. [30], [37] Increasing the size of the particle dampens the oscillation and this reduced strength of the oscillation is directly observed in the full-width at half-maximum (FWHM) value of the resonance peak. A quality factor can account for the strength of this oscillation:

$$Q = \frac{\omega}{\Delta\omega},$$

2.29

where $\Delta\omega$ is FWHM value of the oscillation located at ω.

Both SPPs and LSPs exhibit evanescent wave nature on the surface. Creation of evanescent waves confines the incident electromagnetic waves into small dimensions leading to the field localization with significant increase in the local field intensities. This local field intensity increase causes a local density of states disturbance for electromagnetic fields. Electromagnetic density of states (g_0^{ph}) strongly affects the

spontaneous emission rate of the emitters and is closely related with the coefficient in Equation 2.10

$$g_0^{ph}(\omega) = \frac{\omega^2}{\pi^2 c^3}$$

2.30

and the spontaneous emission rate in terms of $g_0^{ph}(\omega)$ and the dipole moment for a given transition μ is given by [38]

$$r_{spont} = \frac{1}{3\epsilon_0}\mu^2 \frac{\omega_0}{\hbar}\pi g_0^{ph}(\omega)$$

2.31

In the seminal proceeding paper of Edward Mills Purcell on the modification of spontaneous emission rate and decay lifetime in the presence of a resonant antenna in the radio frequency range can be applied to quantum emitters as well. If the system favors one oscillation, the density of states for all oscillations will be modified and the local density of states should be defined. For a resonant interaction in a system, the quality factor dictates the Purcell factor on the emission characteristics. The spontaneous emission rate in the vacuum (r_{spont}) and that in the cavity (r_{spont}^{cavity}) are related as follows [24]

$$r_{spont}^{cavity} = \frac{3}{4\pi^2}\frac{\lambda^3}{V}Q r_{spont}$$

2.32

In Equation 2.32, V is the modal volume of the oscillation being compared with λ^3 and Q is the quality factor of the mode oscillation in the cavity.

The emission enhancement also depends on the electric field enhancement due to field localizations typically observed in plasmonic cavities and the field enhancement factor F can be defined as

$$F = \frac{\left|\vec{E}(\vec{r},\omega)\right|^2}{\left|\overrightarrow{E_0}(\omega)\right|^2}\frac{g^{ph}(\vec{r},\omega')}{g_0^{ph}(\omega')} \qquad 2.33$$

where the first term accounts for the absorption increase due to local electric field enhancement at the absorption frequency ω and the second term accounts for the density of states modification in a cavity for an emitter emitting at the frequency ω'. [24] Purcell enhancement [39]–[42] and lifetime modification [43] are observed experimentally in numerous studies for quantum emitters. Observation of this enhancement is also possible for electrically pumped quantum emitters. [44] Purcell enhancement is the reason of surface enhanced Raman scattering (SERS). [45] In SERS applications, it is mistakenly reported that the enhancement factors are proportional to the fourth power of electric field magnitude. Although the effective enhancement factor is still Equation 2.33, the frequency difference between the incident and scattered light is almost zero and the modification in density of states can be attributed purely to the electric field modification in Raman scattering. Unlike scattering mechanism, light absorption and emission are affected by the environment significantly and system losses especially for lossy metallic

structures may exceed Purcell enhancement in most cases. In this case, instead of an enhancement in the emission, a strong quenching is observed.

Chapter 3

Fabrication and Characterization Techniques

In Chapter 2, we provided brief information required for the understanding of basic concepts of this thesis. In this chapter, we will introduce fabrication and characterization techniques used during the studies of this thesis. Observation of small features and confinement effects requires sensitive and optimized instruments. Fabrication techniques will be introduced under three subsections: additive, etching and patterning methods. Precise characterization of the fabricated structures is also of critical importance. In the context of this thesis, we will briefly introduce imaging and optical spectroscopy techniques as well

3.1 Additive Methods

Mostly pioneered by the material researchers, various methods have been developed to precisely deposit different materials on different surfaces in a controlled way. Although there are different deposition methods for various phases of materials to be deposited, it is possible to define two main categories for the additive methods for the vapor phase

deposition: physical and chemical. Chemical vapor deposition techniques cover a wide spectrum of materials and can offer additional capabilities including material selective deposition and epitaxial growth. In this thesis, we will focus on physical vapor deposition methods: thermal and electron beam deposition.

3.1.1 Thermal Deposition

Being a physical vapor deposition technique, the thermal deposition is one of the most commonly used and simple methods. It is generally suitable for low critical temperature materials (gold, silver, copper, etc.). During the operation, an evaporation boat made of high-melting temperature material is heated under high electrical powers. Evaporation material is vaporized under ultra-high vacuum and material vapor in a beam is deposited onto the substrate. The vapor beam follows a $\cos^2$ deposition rate in a conical form directed from the center of the boat. The deposition rate is controlled by the electrical power and monitored by a calibrated quartz thickness monitor. A shutter ensures the initiation of the deposition exactly at the desired deposition rate. A typical thermal deposition chamber is illustrated in Figure 3.1. Sample rotation is an option: if a more uniform deposition is desired, rotation certainly helps, however, especially for liftoff applications, the rotation results in sidewall deposition, which is catastrophic for the liftoff process. Deposited materials at the sidewalls prevent liftoff and rotating the substrate is not recommended in this case.

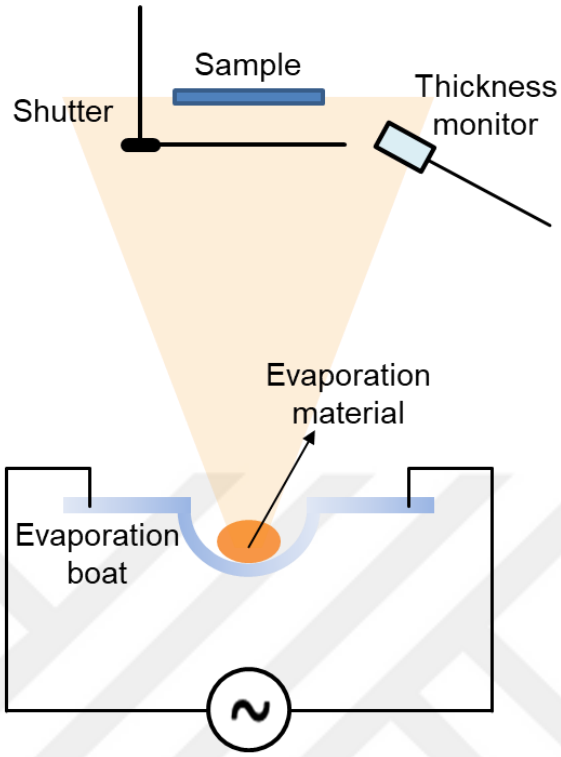

Figure 3.1 Thermal deposition technique illustration. Evaporation material is heated inside a high critical-temperature evaporation boat under ultrahigh vacuum. A beam of material vapor is deposited uniformly on the substrate while the deposition thickness is tracked via a thickness monitor.

3.1.2 Electron Beam Deposition

An alternative method to the thermal deposition is electron beam (E-beam) deposition (EBD). In this case, instead of heating whole evaporation material, a highly energetic and focused electron beam is directed towards the evaporation material placed in a crucible. The e-beam interacting with a portion of the material results in local heating. EBD is especially useful for high critical temperature materials (chromium, titanium, silicon oxide, etc.) Apart from the heating mechanism, EBD shares similar components

as the thermal deposition technique. In most of the systems, a shutter, a thickness monitor and substrate rotation options are common as illustrated in Figure 3.2.

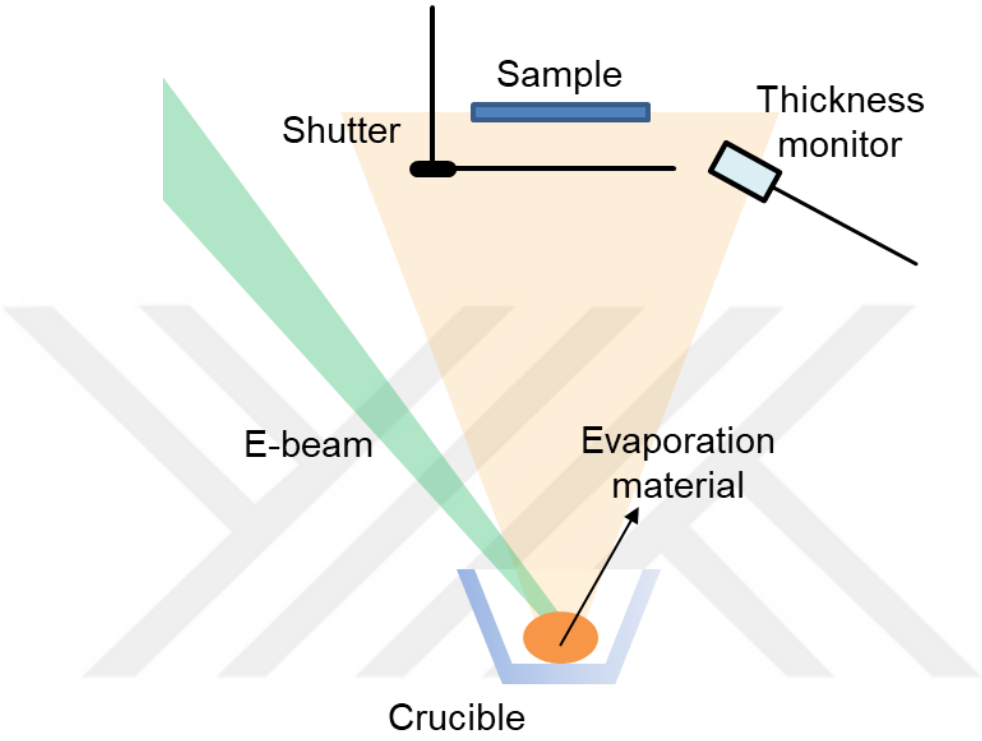

Figure 3.2 Electron beam deposition technique illustration. Inside a crucible, evaporation material is heated with a high current electron beam under ultrahigh vacuum. A beam of material vapor is deposited uniformly on the substrate while the thickness is tracked with a thickness monitor.

3.2 Etching Methods

Similar to additive methods, etching methods can be separated into two main categories: physical and chemical etching. Among various etching methods, the physical etching methods like argon milling are not commonly utilized in nanofabrication. Since milling is not material selective and highly directional, it is not versatile enough. On the other

hand, the chemical etching methods can offer extreme versatility. Chemical etching can be in wet or dry forms and depending on the application, the resulting etch profile can be anisotropic or isotropic, i.e., etching can be directional or not, respectively.

3.2.1 Wet Etching

Most of the wet etching recipes are isotropic due to the chemical reactivity independent of crystallographic plane of the material. However, in the thesis we employed carefully controlled anisotropic KOH etching of single crystalline silicon surface. Because of this reason, we will briefly introduce conventional KOH etching and our modified recipe for finer nanometric features. Different crystallographic planes of silicon show different etching rates with KOH. KOH etching gives the etching ratios for commonly utilized planes of silicon as (100):(110):(111)=400:600:1 with approximately 2 μm/min etch rate in (100). In this thesis, we will present a nanometer sized v-grooved surface fabricated on silicon surface in Chapter 4 and, unlike conventional microprocessing of silicon, micrometers/min etch rates are too fast for the controlled etching of this nanometric features. Also, fast etching can create tens of nanometers surface roughness, which was unacceptable in our case. KOH etching of silicon at 120 °C while stirring facilitates the removal of hydrogen gas bubbles, which is considered to be the root cause for the rough silicon surface formation while etching without stirring. [46] The resulting etch rate is 12.2 μm/min with measured surface roughness of 21.2 nm. Although this method is believed to outperform conventional 30% KOH etching at 80 °C, it has still a high etch rate, which gives rough surface after etching. To reduce the surface roughness, isopropanol (IPA) can be used [47], [48]. To prepare the etchant, 70 g KOH pellets are dissolved in 190 mL DI water under constant stirring and after obtaining clear solution,

40 mL IPA is added. For this recipe, we used stirring and ultrasonic agitation separately. Under continuous stirring at 80 °C, the expected etch rate is 1 μm/min [47]. Similarly, 3 M KOH (~15wt%) and 12% IPA solution at 60 °C results in 0.11 μm/min [48]. Increasing the IPA concentration and decreasing the temperature slows down the etch rate of silicon. To reduce the etch rate, an additional surfactant can also be used. Triton-X 100 added into KOH solution reduces the selectivity between (100) and (110) planes, enabling 45° walls by etching silicon wafer [49]. Using 2 M (10wt%) KOH solution and 100 ppm (parts per million in volumes) Triton-X 100, we expect 0.08 μm/min etch rate at 75 °C, leading to 4.59 nm surface roughness [50]. SEM images of all resulting surfaces of the corresponding recipes are presented in Figure 3.3. Among all the recipes, 15% KOH and 12% IPA solution at 60 °C with stirring gave the best result in the light of SEM observation. Even after this fine etching, there are some small surface irregularities, however, we observed that these irregularities can be eliminated after using an additional HF acid etching, which we apply in the cleaning step of final mold fabrication (Radio Corporation of America).

IPA saturated recipe leads to the best (100) surface quality. Another optimized recipe for anisotropic etching of silicon with saturated IPA solution [51] is used with chromium masked pattern in Figure 3.4. 20wt% KOH dissolved in 80wt% H_2O: IPA (4:1) solution with stirring at 40 °C for 4 min followed by DI water washing results in anisotropically etched Si surface.

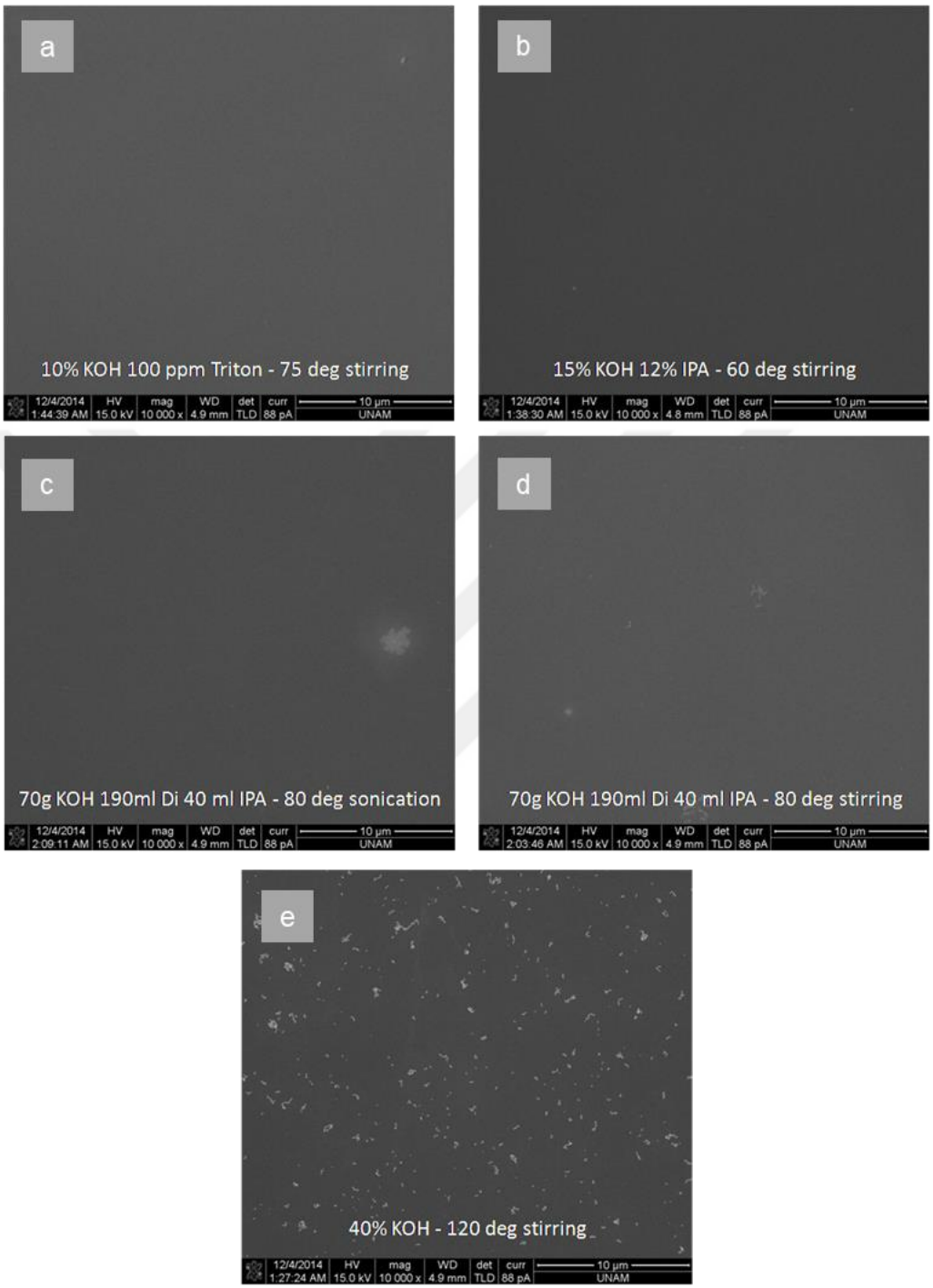

Figure 3.3 Si (100) surfaces imaged following different KOH etch recipes under the same contrast, brightness and magnification.

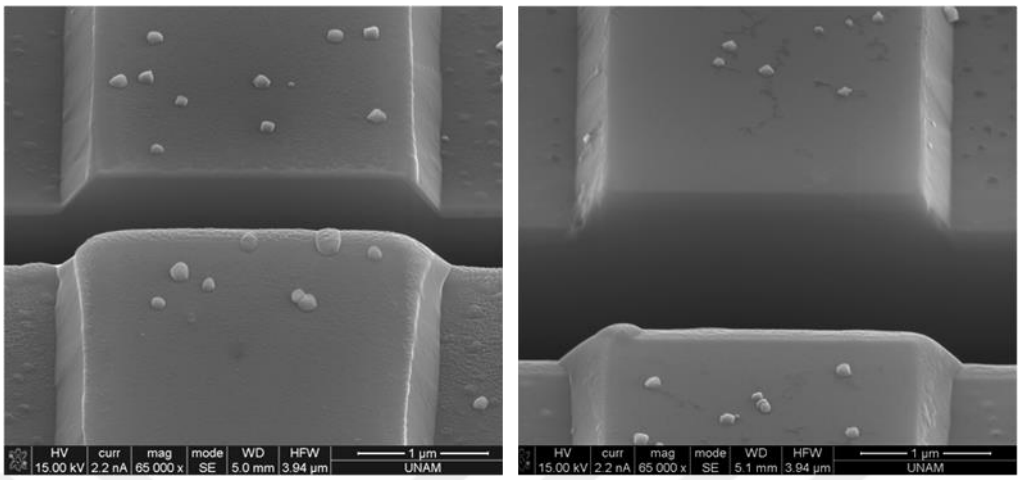

Figure 3.4 Anisotropic etching of Si (100) surface before (left) and after (right) Cr mask removal.

3.2.2 Dry Etching

As a complementary tool to the wet etching, dry etching introduces a significant versatility in nanofabrication. Dry etching can be chemical, physical or the combination of the both. In basic systems, a plasma reactor is used to increase the chemical interaction rate between the injected reactive gas and the material. In this respect, reactive ion etching (RIE) systems are mostly isotropic etcher systems. Anisotropic etching achieved by creating and directing the plasma onto the surface. Inductively coupled plasma RIE (ICP-RIE) systems can achieve faster chemical as well as anisotropic etching. It is also possible to create a noble gas plasma like argon plasma and direct ionized argon atoms to the surface to physically mill the surface. Commonly, ICP-RIE systems uses two plasma generators namely low-frequency plasma platen to enhance the plasma, and high-frequency plasma platen to direct plasma. It is possible to play with the anisotropy of the etch profile by adjusting the power of the high-frequency platen. For low power levels,

the etch will be mainly chemical and hence isotropic and, for high power levels, the etch is more physical and thus anisotropic.

Most commonly used recipe for the anisotropic etching of silicon surface is Bosch process, which utilizes consecutive etching and deposition steps. During this process, SF_6 etches the surface and C_4F_8 deposits a polymeric layer isotropically. With the effect of the high-frequency platen, the etching can be anisotropic and while sidewalls are protected with the deposited layer, the bottom part will be etched. In this way it is possible to etch directly into the silicon surface in the surface normal direction. However, as it can be seen from Figure 3.5a, these etching and deposition cycles leave a trench structure on the sidewalls for each cycle. Although these trenches can be reduced to nanometer range, which is acceptable for microfabrication, we need smoother sidewalls for our fabrication process. Instead of providing the SF_6 and C_4F_8 gases consecutively as a serial process, we provided them simultaneously into the chamber. [52] The resulting etch profile is shown in Figure 3.5b. Perfect vertical sidewalls without any trenches are obtained for SF_6:C_4F_8-33:55 sccm with high-frequency platen in forward power mode. In Figure 3.6, for a large area of dense structures, using the modified Bosch process, the etching of silicon surface is successfully shown. In Figure 3.6a we used a thermally grown 300 nm silicon oxide layer as the etch stop mask and in Figure 3.6b a dense grating structure is masked with 30 nm of chromium. It is also worth pointing out the highly material selective nature of this etching process since the etch poorly attacks PMMA. Thus right after electron beam lithography and development steps, it is possible to use patterned PMMA as the etch stop mask.

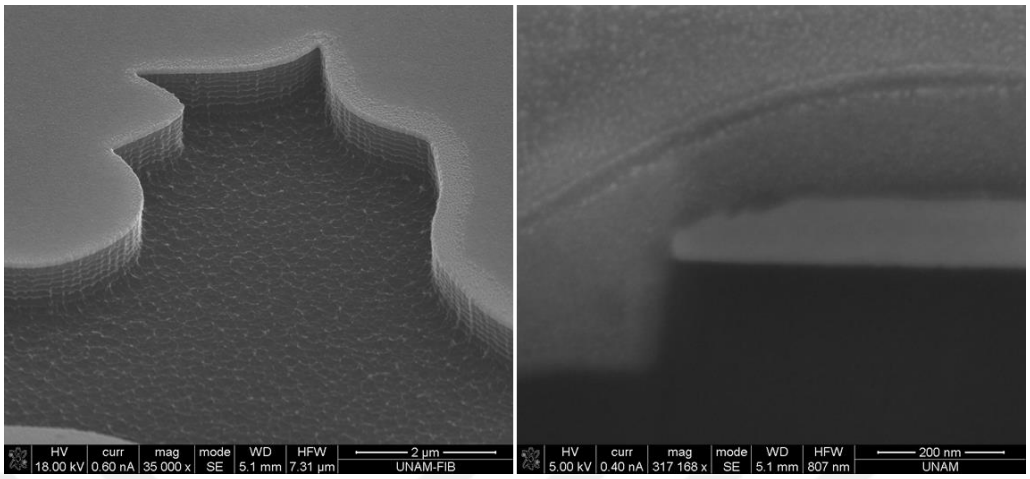

Figure 3.5 Anisotropic dry etching of silicon surface. While conventional Bosch process leaves nanometric trenches (left), the modified Bosch process leaves a smooth vertical profile (right).

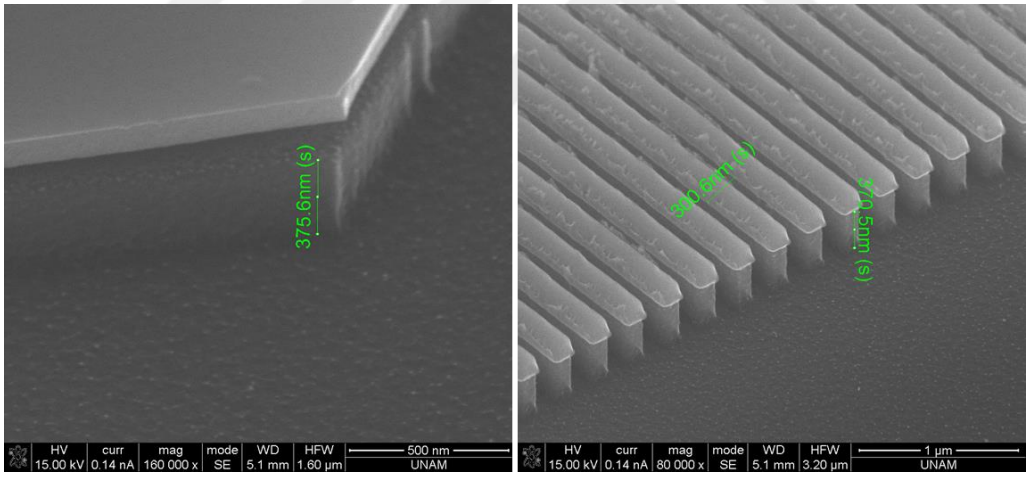

Figure 3.6 Modified Bosch process applied to silicon oxide (left) and chromium (right) etch masks on silicon surface.

3.3 Patterning Methods

Patterning is the most critical step of the nanofabrication processing. The demand for high-performance products in the consumer market and challenging research requirements create a driving force to push the limits of the nanofabrication to smaller dimensions continuously. The resolution of patterning (and similarly imaging) systems is fundamentally limited with the diffraction, which is directly related with the operating wavelength of the system. This resolution is determined by the Airy disc formation of a perfect spot in the farfield, which is given by $R = \frac{0.61\lambda}{NA}$ where R is the resolvable feature size, λ is the system operating wavelength, and NA is the numerical aperture of the imaging system. Using immersion methods, NA can take values like 1.0-1.4 in typical systems. Therefore, a rough estimation on the resolution of $R \cong \lambda/2$ is practically accurate enough. Considering the visible light wavelength range of 400-700 nm, the best resolution can be obtained with a light microscope is about 200 nm. For photolithography, 193 nm light sources are typical with a practical resolution of R ~ 80 nm. Using highly optimized systems, a resolution level of 10 nm is possible for transistor fabrication but these values are impractical for general research purposes requiring a certain degree of freedom in the design. Further reducing the operating wavelength of optical systems is quite challenging due to the limitations in the development of reliable short-wavelength light sources as well as of the photoresists to work with them.

On the other hand, electrons having a rest mass, m_0, characterized by De Broglie wavelength, and at high acceleration voltages, the relativistic calculation gives

$$\lambda = \frac{h}{\left(2m_0 eV\left(1 + \frac{eV}{2m_0 c^2}\right)\right)^{\frac{1}{2}}}$$

3.1

An electron accelerating under the potential difference of 1 V has 1 eV energy with a wavelength of 1.23 nm whereas the light wave having 1 eV energy has a wavelength of 1239 nm. This is a three orders of magnitude difference. Also, it is easy to accelerate electrons under high potential differences. Typical electron microscopes work under 30 – 300 kV accelerating voltages. An electron accelerated under V = 100 kV leads to λ = 3.70 pm, more than enough to resolve a single atom. Thanks to this resolution capability, electron beam lithography is an enabling tool for nanofabrication, which may not be possible with other methods. In this thesis, we used electron beam lithography systems for our nanofabrication; hence, we will briefly introduce the beam writing techniques and the template-stripping method.

3.3.1 Electron Beam Lithography (EBL)

In electron beam lithography (EBL), a resist sensitive to the electron beam is used for patterning. The minimum achievable feature size using EBL is determined by the resist material. Typically, 50 nm dense structures and 20 nm isolated structures can be defined by using 495 K and 950 K PMMA resists having ~100 nm thicknesses. When the electron beam interacts with the resist at the correct dosage, the resist changes its chemical structure and becomes soluble in the developer solution. After the developing process, the patterned EBL resist can be used as the final structure: e.g., as an etch mask for the underlying substrate or, after metallization, as a sacrificial layer for the liftoff

process. EBL is a convenient method for research purposes or rapid prototyping. However, due to being a serial process, it is a time-consuming and expensive fabrication tool. In Figure 3.7, some EBL fabricated structures of ours are shown using Bilkent University UNAM facilities.

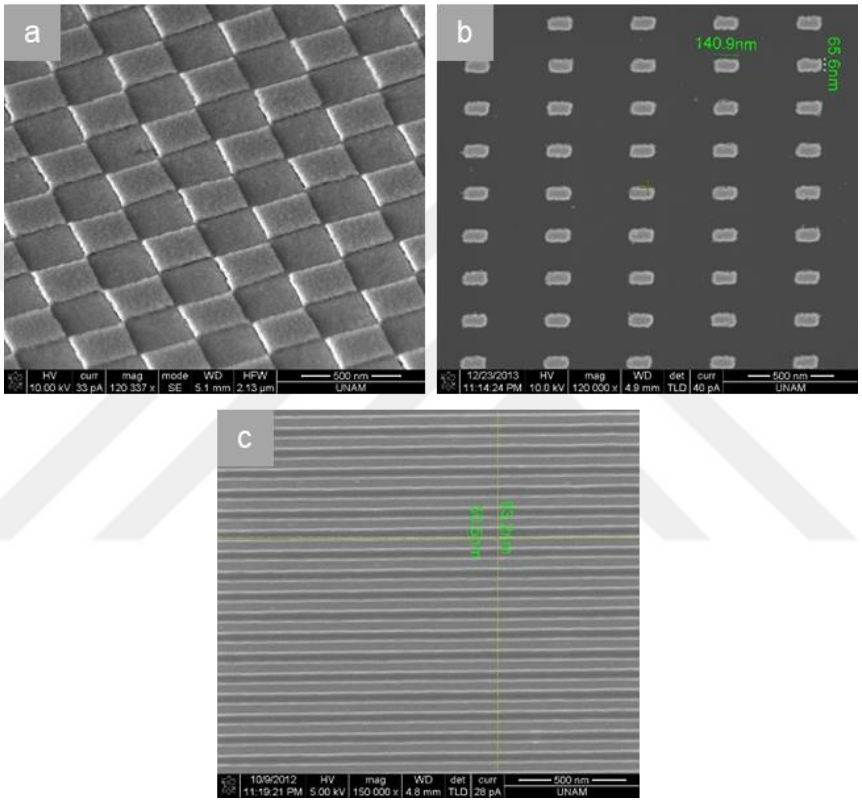

Figure 3.7 a) Fabricated checkerboard structure with sharp corners. b) Monodisperse gold blocks with nanometer sized features. c) 50% duty cycle grating structure with a periodicity of 100 nm.

3.3.2 Focused Ion Beam (FIB) Lithography

Similar to the electron beam techniques injecting a beam of electrons, ion beam systems can create a beam of ions that can be used for imaging and patterning. Focused ion beam (FIB) lithography is performed by using dual-beam scanning electron microscopes

(SEM). Unlike the other conventional fabrication methods, it is a direct lithography tool and it does not require a predeposited resist to develop. Any material can be milled using gallium ions. In addition to the milling, with highly reactive gases of metallic compounds, it is possible to deposit metallic structures with high precision in FIB. This deposition step does not require any predeposited resist, either. FIB is typically used for rapid prototyping, TEM sample preparation, and rapid cross-sectional SEM observation. In Figure 3.8, the direct patterning of thin gold film into a bullseye structure, nickel nanowire slicing, and cross-sectional observation of deep ICP-RIE etched silicon are presented. We performed all these presented processes at Bilkent University in UNAM.

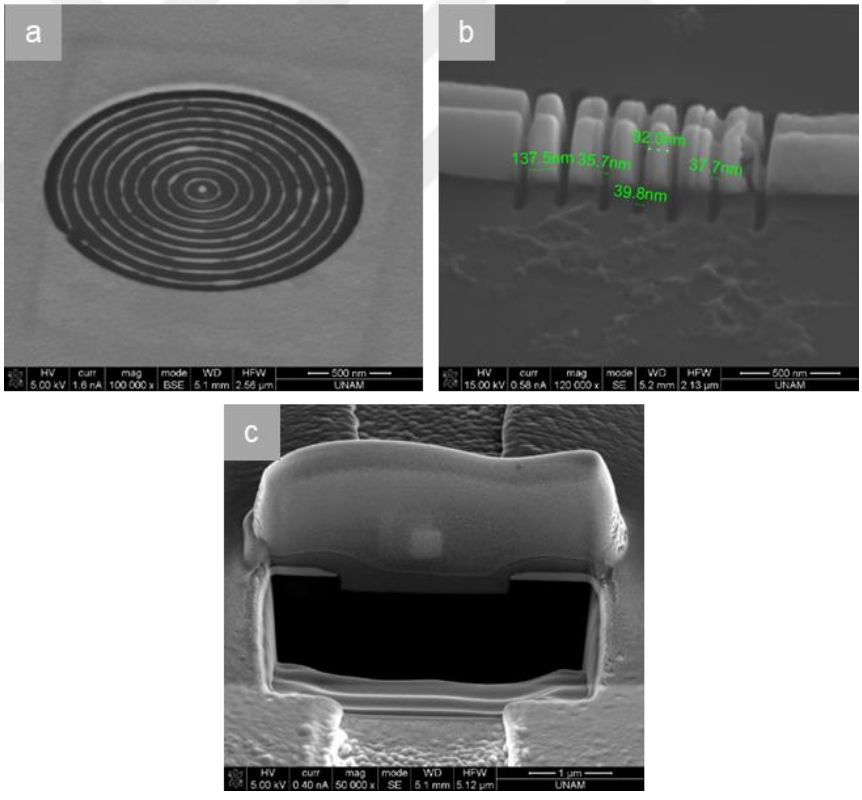

Figure 3.8 a) Gold bullseye structure with very thin lines. b) Nickel nanowire slicing for nanodisc fabrication. c) FIB milling for cross-sectional imaging of anisotropically etched Si masked by gold.

3.3.3 Template Stripping

Many demanding applications require ultra-smooth substrate and device surfaces. Unfortunately, surface roughness is an inevitable result of many fabrication methods. Due to the limited adhesion to silicon surface, thin films of especially gold and silver create isolated island-like structures on the surface for sub-20 nm film thicknesses. In addition, during the development and liftoff steps of lithography, PMMA swelling and small connections occurring at the sidewalls of deposited material induce unwanted surface roughness. The feedback mechanism occurring during the anisotropic etching of silicon inherently creates an ultra-smooth atomically flat crystalline surface. Also, the exact borders of crystallographic planes can produce very sharp corners. Utilization of such smooth surfaces and sharp corners is possible for the deposited metallic layers using the-so-called template stripping method. Using silanization, the surface energy of silicon and silicon oxide reduces significantly, and any deposited layer can be peeled off from the surface. For the fabrication of sharp corners of the v-grooved surface that we will discuss in Chapter 4, we used this silanization step on the mold structure. We used 1H,1H,2H,2H-perfluorodecyltriethoxysilane silanization agent in the nitrogen filled glovebox environment to avoid oxygen interaction. First, we let silicon wafer to reach 200 °C on a hot plate with a glass petri dish covering the hot plate surface as illustrated in Figure 3.9. Then, at 200 °C, we inject 30 μL of the silanization agent and covered the glass petri dish to avoid gas leakage. Immediate vapor creation inside the petri dish is a sign of the silanization process. After 30 min, excess agent is rinsed inside analysis grad hexane. The first trials of template stripping are shown in Figure 3.10. The mold is fabricated via photolithography with micrometer sized features. The etch mask is thermally grown silicon oxide on the surface. High-quality and smooth gold surface can

be seen here. In Figure 3.11 a chromium masked mold is used with different density of structures. Wavy features on the peeled gold surface is due to the heating that occurred during the electron beam imaging.

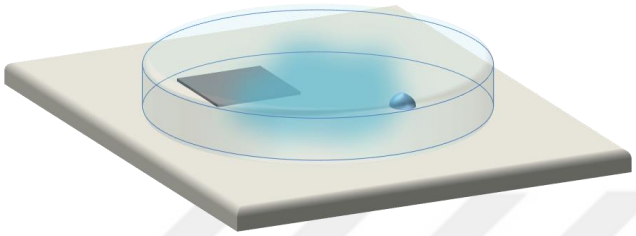

Figure 3.9 Silanization process illustration on a hot plate.

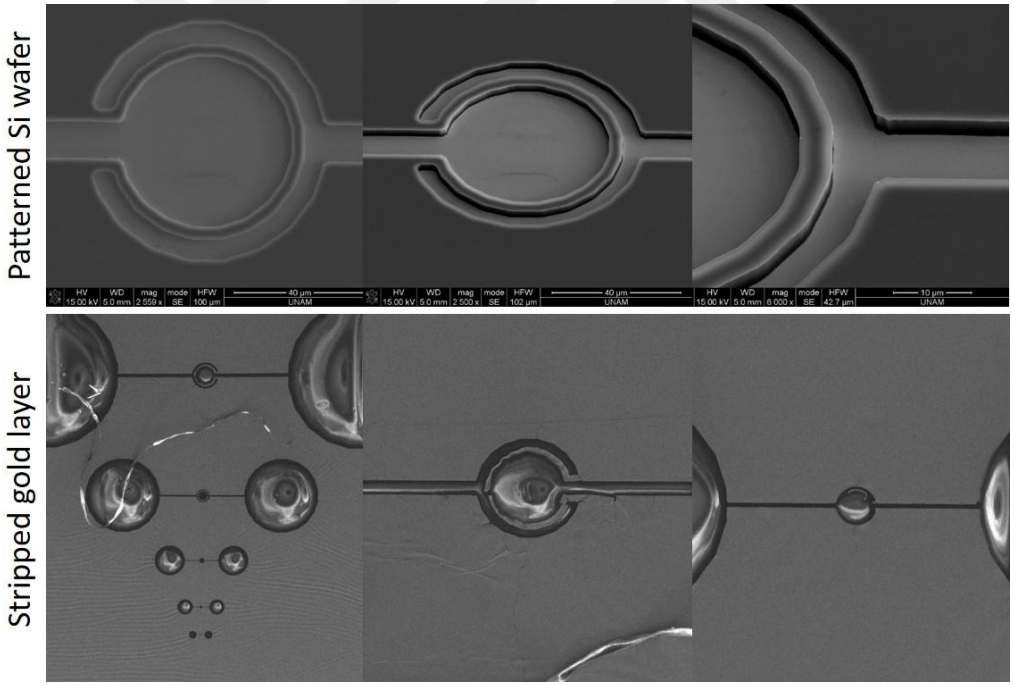

Figure 3.10 Results of our development of the template stripping from silicon surface having micrometer sized features. 300 nm silicon oxide masked surface of silicon is etched using anisotropic dry etching and silanized. A deposited thin layer of gold is peeled off the template using a supporting polymer layer.

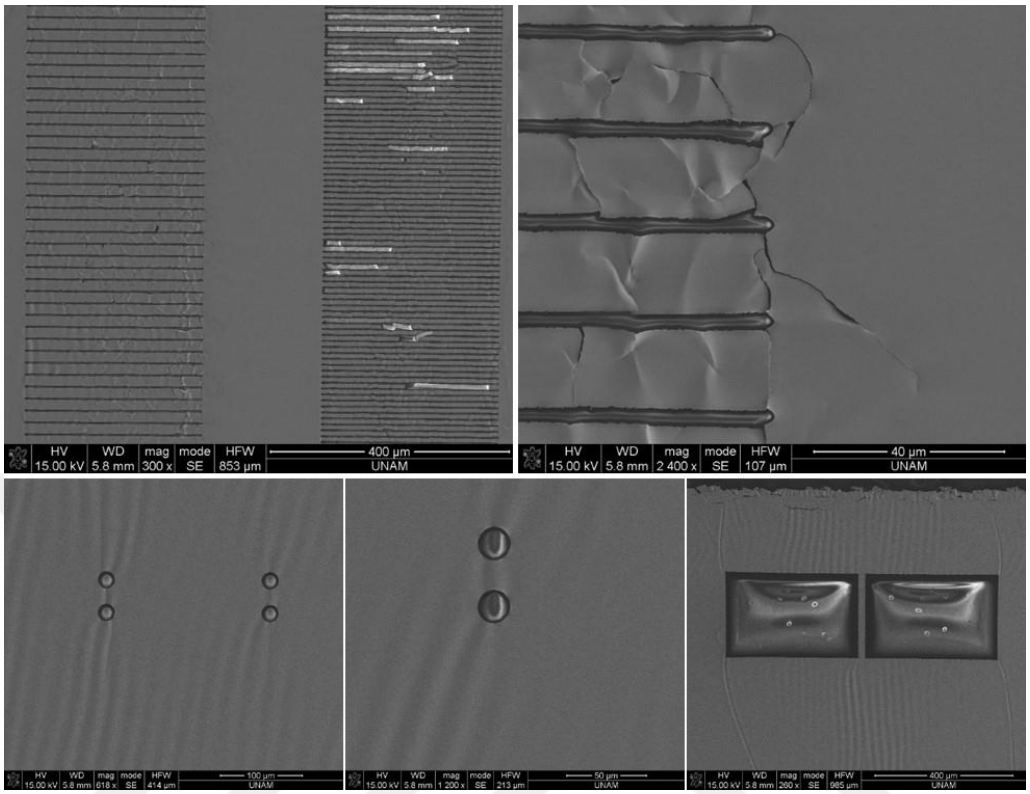

Figure 3.11 Results of our additional examples of the template stripping from silicon surface. This time a thin chromium layer is used to mask the surface of silicon during anisotropic dry etching. After silanization, deposited thin layer of gold is peeled off the template with a supporting polymer layer. The wavy surface observed in some small structures is due to the supporting polymer swelling due to heating under the bombardment of the electron beam during SEM imaging.

3.4 Imaging Methods

Following their fabrication, inspecting nanostructures is critical. Among different imaging techniques, the most commonly used methods are optical and electron beam (e-beam) imaging techniques. We discussed the capabilities and resolution limits of such optical and e-beam techniques in Subsection 3.3. Here, we will discuss different aspects of optical and e-beam imaging methods, where we will focus on the additional

information that can be obtained using these two methods. Optical microscopy will be introduced from the brightfield and darkfield microscopy techniques point of view. Additionally, back focal plane imaging configuration that we used in Chapter 4 will be explained. Finally, e-beam imaging systems will be explained by electron beam and material interaction types.

3.4.1 Brightfield and Darkfield Optical Microscopy

Starting from the invention in the 16th century, optical microscopes have served different functionalities driven by the application requirements. Brightfield, darkfield, phase contrast, confocal and many other different microscopy techniques applied on the optical microscopes provided us different means of inspecting and understanding different aspects of the nature. In this thesis, brightfield and darkfield configurations of optical microscopy were used for common structural inspection. In Figure 3.12, these two configurations are illustrated for inverted-type optical microscopes. Here an illumination source, which is conventionally a halogen light bulb (typically 100 W) commonly used, (although white super-luminescent LEDs are becoming popular), is condensed over a transparent sample. An objective in the opposite end collects the transmitted light through the sample. The image plane is imaged onto the retina with an eyepiece or to a CCD with the imaging tube. In the brightfield configuration, the background is bright and the observed features are created due to the absorption and scattering from the structures on the surface. In the darkfield configuration, however, the background is dark. An opaque disc blocks the direct light into the objective. If there is no scattering structure in the light path, the objective collects no light. The darkfield microscopy allows to see the scattering off any discontinuity on the focused sample surface including

particles and small features on the surface. Even transparent structures with slight refractive index differences can be imaged in the darkfield configuration. For example, scattered light characterization is essential for plasmonic structures and the darkfield microscopy is an excellent enabling tool for this purpose. It is also possible to measure additionally the optical transmission and scattering spectra with an optical spectrometer placed at the image plane.

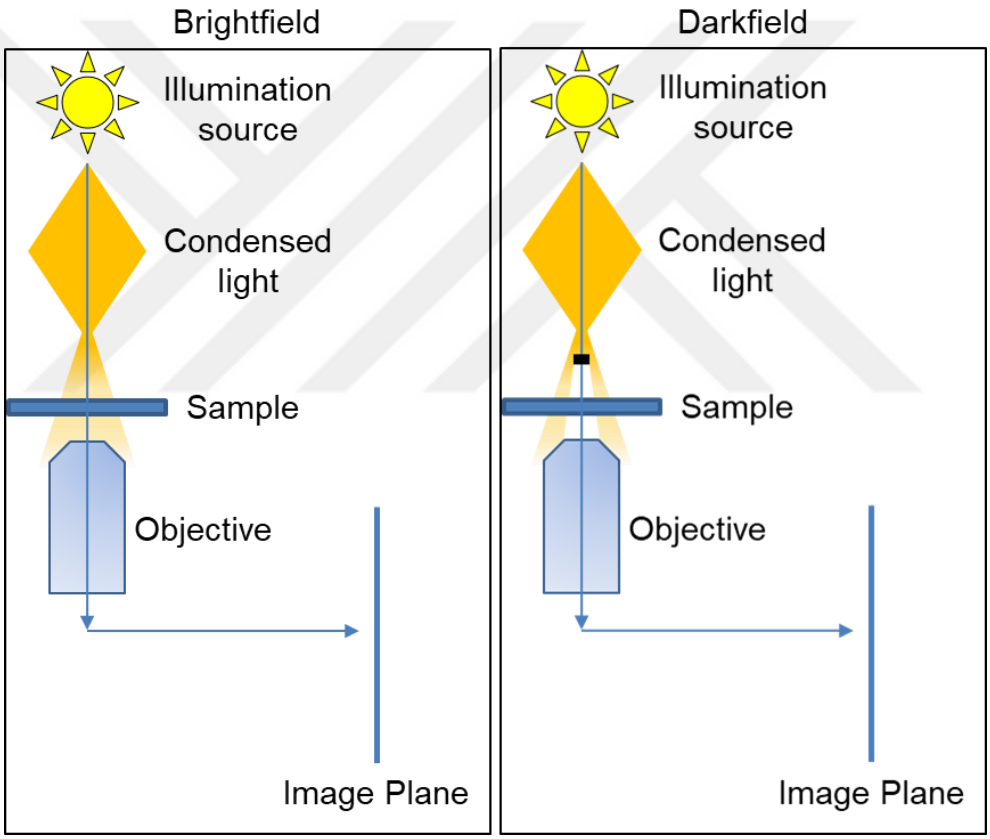

Figure 3.12 Brightfield and darkfield microscopy configurations for the inverted optical microscope.

3.4.2 Back Focal Plane Imaging

Back focal plane (BFP) imaging is a powerful technique to observe the dipole orientations of emitters. With this method, the dipole orientation of even single molecules can be detected. [53] Electric field intensities can be calculated using the local density of optical states (LDOS). Using the angular representation of the dyadic Green's function [37], we can obtain LDOS equations for the s- and p-polarization components in the x-z plane as follows [54]

$$\rho_x^s(\omega, k_{||}) = \left(\frac{1}{8\pi k_0^2}\right)\left(\frac{k_0}{k_{z3}}\right)\left|\frac{t_{32}^s e^{ik_{z2}d}\left(1 + r_{21}^s e^{2ik_{zz}h}\right)}{1 - r_{21}^s r_{23}^s e^{2ik_{z2}D}}\right|^2$$

$$\rho_y^p(\omega, k_{||}) = \left(\frac{1}{8\pi k_0^2}\right)\left(\frac{k_0}{k_{z3}}\right)\left|\frac{t_{32}^p e^{ik_{z2}d}\frac{k_{z2}}{n_2 k_0}\left(1 - r_{21}^p e^{2ik_{2z}h}\right)}{1 - r_{21}^p r_{23}^p e^{2ik_{z2}D}}\right|^2$$

$$\rho_z^p(\omega, k_{||}) = \left(\frac{1}{8\pi k_0^2}\right)\left(\frac{k_0}{k_{z3}}\right)\left|\frac{t_{32}^p e^{ik_{z2}d}\frac{k_y}{n_2 k_0}\left(1 + r_{21}^p e^{2ik_{2z}h}\right)}{1 - r_{21}^p r_{23}^p e^{2ik_{z2}D}}\right|^2$$

3.2

where k_{zi} is defined as

$$k_{zi} = \sqrt{n_i^2 k_0^2 - k_x^2}$$

3.3

Here transmission and reflection coefficients for the s- and p-polarizations are calculated using Fresnel equations

$$t_{ij}^{p} = \frac{2n_i n_j k_{zi}}{n_j^2 k_{zi} + n_i^2 k_{zj}}, \qquad t_{ij}^{s} = \frac{2k_{zi}}{k_{zi} + k_{zj}}$$

$$r_{ij}^{p} = \frac{n_j^2 k_{zi} - n_i^2 k_{zj}}{n_j^2 k_{zi} + n_i^2 k_{zj}}, \qquad r_{ij}^{s} = \frac{k_{zi} - k_{zj}}{k_{zi} + k_{zj}}.$$

3.4

Since our structure has another layer in the given configuration, to generalize this 3-layer system to any multilayered system, we used the transfer matrix method to compute the overall transmission coefficient $t_{j1}^{s,p}$:

$$M_{ij}^{s,p} = \frac{1}{t_{ji}^{s,p}} \begin{bmatrix} t_{ij}^{\mathrm{s,p}} t_{ji}^{\mathrm{s,p}} - r_{ij}^{\mathrm{s,p}} r_{ji}^{\mathrm{s,p}} & r_{ji}^{\mathrm{s,p}} \\ -r_{ij}^{\mathrm{s,p}} & 1 \end{bmatrix}, \qquad M_{j,phase} = \begin{bmatrix} e^{-ik_{zj}} & 0 \\ 0 & e^{ik_{zj}} \end{bmatrix}$$

3.5

$$M_{j1}^{\mathrm{s,p}} = M_{j(j-1)}^{\mathrm{s,p}} M_{(j-1),phase} \dots M_{34}^{\mathrm{s,p}} M_{3,phase} M_{23}^{\mathrm{s,p}} M_{2,phase} M_{12}^{\mathrm{s,p}}$$

3.6

$$t_{j1}^{\mathrm{s,p}} = \frac{1}{M_{j1}^{\mathrm{s,p}}(2,2)} \left[M_{j1}^{\mathrm{s,p}}(1,1) M_{j1}^{\mathrm{s,p}}(2,2) - M_{j1}^{\mathrm{s,p}}(1,2) M_{j1}^{\mathrm{s,p}}(2,1) \right]$$

3.7

Finally, LDOS equations are generalized as follows:

$$\rho_x^s(\omega, k_{||}) = \left(\frac{1}{8\pi k_0^2}\right)\left(\frac{k_0}{k_{zj}}\right) \left| \frac{t_{j1}^s e^{ik_{z2}d}\left(1 + r_{21}^s e^{2ik_{zz}h}\right)}{1 - r_{21}^s r_{23}^s e^{2ik_{z2}D}} \frac{k_y}{\sqrt{k_x^2 + k_y^2}} \right|^2$$

$$\rho_y^p(\omega, k_{||}) = \left(\frac{1}{8\pi k_0^2}\right)\left(\frac{k_0}{k_{zj}}\right)\left|\frac{t_{j1}^p e^{ik_{z2}d}\frac{k_{z2}}{n_2 k_0}\left(1 - r_{21}^p e^{2ik_{2z}h}\right)}{1 - r_{21}^p r_{23}^p e^{2ik_{z2}D}}\frac{k_x}{\sqrt{k_x^2 + k_y^2}}\right|^2$$

$$\rho_z^p(\omega, k_{||}) = \left(\frac{1}{8\pi k_0^2}\right)\left(\frac{k_0}{k_{zj}}\right)\left|\frac{t_{j1}^p e^{ik_{z2}d}\frac{k_x}{n_2 k_0}\left(1 + r_{21}^p e^{2ik_{2z}h}\right)}{1 - r_{21}^p r_{23}^p e^{2ik_{z2}D}}\right|^2$$

3.8

Using the LDOS equations and considering all possible dipole moments, it is possible to calculate electric field intensity at the BFP. In Figure 3.13, we illustrated the BFP image formation of aligned dipoles in the emitter layer. When an aligned dipole radiates, the polarization state of each angular point is modified. Using a polarizer at the collection end, it is possible to observe the differences as illustrated. The polarizer allowing to pass the light in the x-direction transmits most of the emission of a dipole when it is aligned in the x-direction. Only a slight reduction in the intensity is expected around 45°, 135°, 225° and 315° directions, which are indicated with faded and slightly rotated arrows. If the polarizer allows the light to pass in the y-direction, the dipole in the x-direction suffers in 0°, 90°, 180°, and 270° directions in the BFP image. Although a large reduction in the light intensity is expected, the light will pass in 45°, 135°, 225° and 315° angles. A BFP imaging setup is illustrated in Figure 3.14 and our built setup is shown in Figure 3.15.

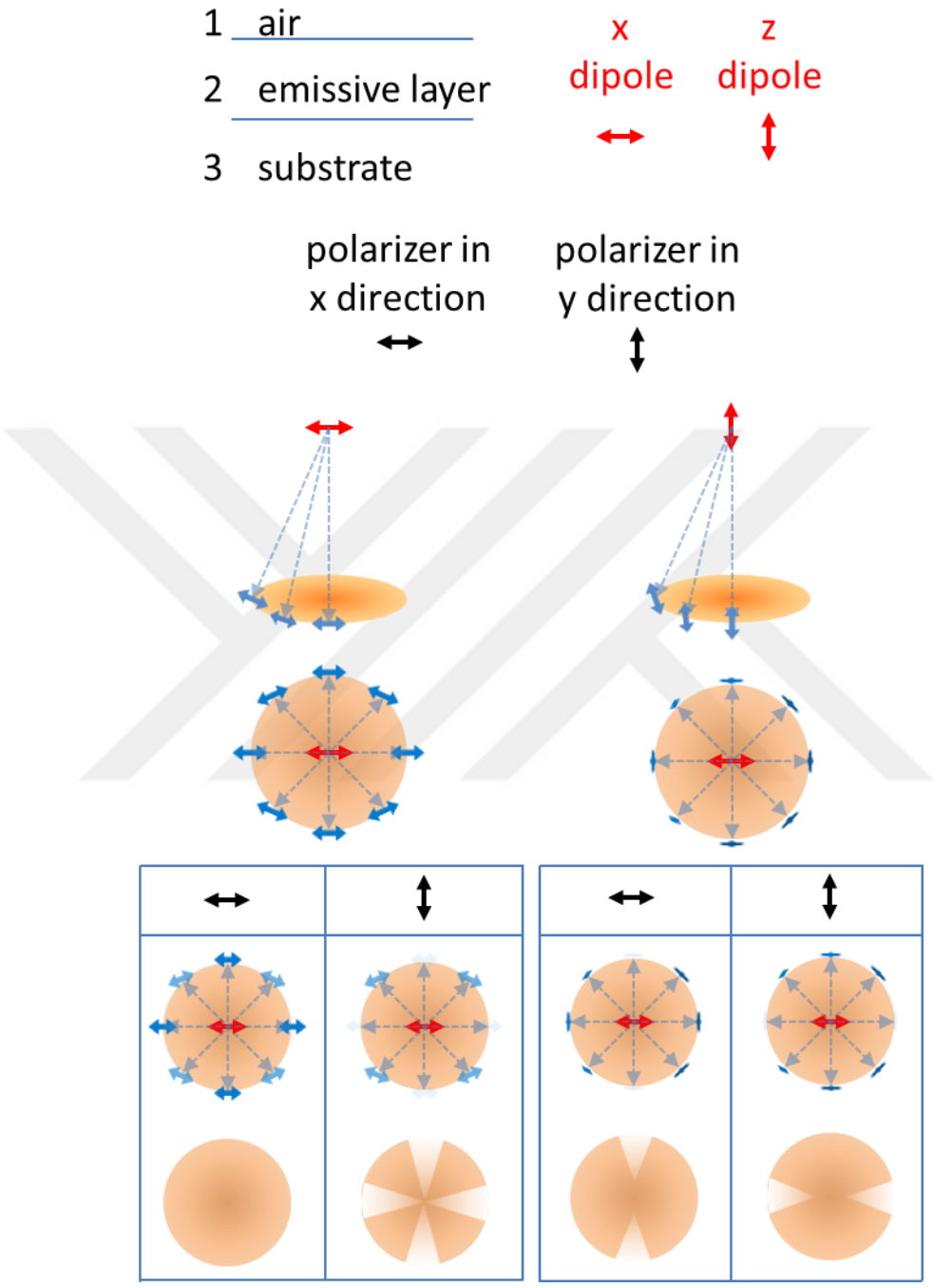

Figure 3.13 BFP pattern formation of aligned dipoles. When a polarizer is placed at the collection end, the modified polarization state of the light can be identified according to the propagation direction.

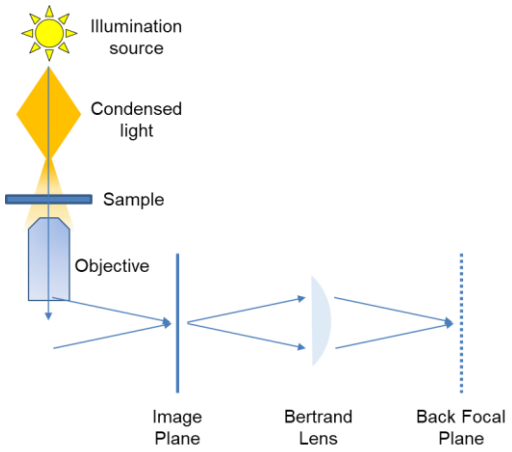

Figure 3.14 BFP imaging configuration. Depending on the application, a luminescent sample can be excited and a lens (called Bertrand lens) placed at one focal length behind the image plane images the BFP at one focal length behind the lens.

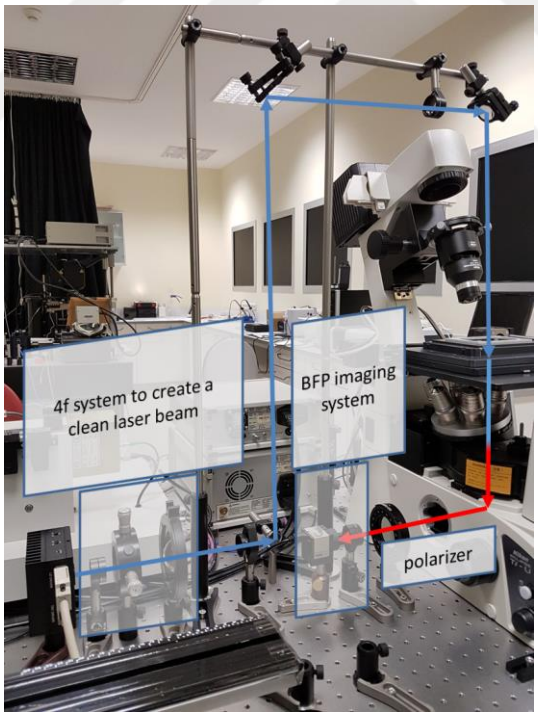

Figure 3.15 Our BFP imaging setup used to measure the dipole orientations of our emitters. A laser beam excites our nanocrystals from the top and a microscope objective collects the emitted light. Using a Bertrand lens the BFP is imaged on CCD.

3.4.3 Electron Microscopies

We explained the main advantage of electron beam imaging in Subsection 3.3 with its superior resolution capability compared to optical imaging systems. However, in addition to enabling better resolution, electrons can give plenty of information related with the physical and chemical structure of a material. Interaction mechanisms of a highly energetic electron beam with material are illustrated in Figure 3.16. SEM and transmission electron microscopy (TEM) are among the main application methods. In SEM, a highly focused electron beam spot scans the surface of a specimen. Scattered secondary electrons and backscattered electrons are collected with detectors. While the secondary electrons mainly give morphological information (as the contrast still depends on the material type), the backscattered electrons mostly provide material information on the surface since the backscattering probability is directly corelated with atomic radius. For the case of thin specimens having thicknesses less than 100 nm and nanoparticles on TEM grids, electrons can pass through the sample and can be collected at the other side. These transmitted electrons can then be imaged. Instead of refractory elements used in optical microscopes, magnetic coils serve as lenses for electrons and enable superior resolution to be achieved in TEM. Various methods similar to darkfield and Fourier plane imaging can be applied in TEM. Elastically scattered transmitted electrons can be detected in a coherent manner and can create diffraction patterns when passed through crystalline structures. This is one of the best tools to analyze the crystal structure and lattice constants, e.g., of nanoparticles. Fourier transformation of these diffraction patterns provides atomic resolution.

In addition to imaging techniques, electrons can provide additional information on the materials. Auger electrons and characteristic X-rays (used in energy dispersion spectroscopy, EDS or EDX) created under electron beam bombardment give elemental composition information. Inelastic scattering of electrons in TEM are used for the electron energy loss spectrum measurement (EELS). EELS provides material related information around keV energy range, however, around couple of eV energies, with a good monochromator attachment, it is possible to study the plasmonic response of the structures at the optical energy regimes. In this thesis, we commonly used SEM and TEM for material analyses. In Chapter 5 the elemental mapping of doped colloidal quantum wells is performed with scanning electron beam generated characteristic X-rays being a good example for EDX mapping.

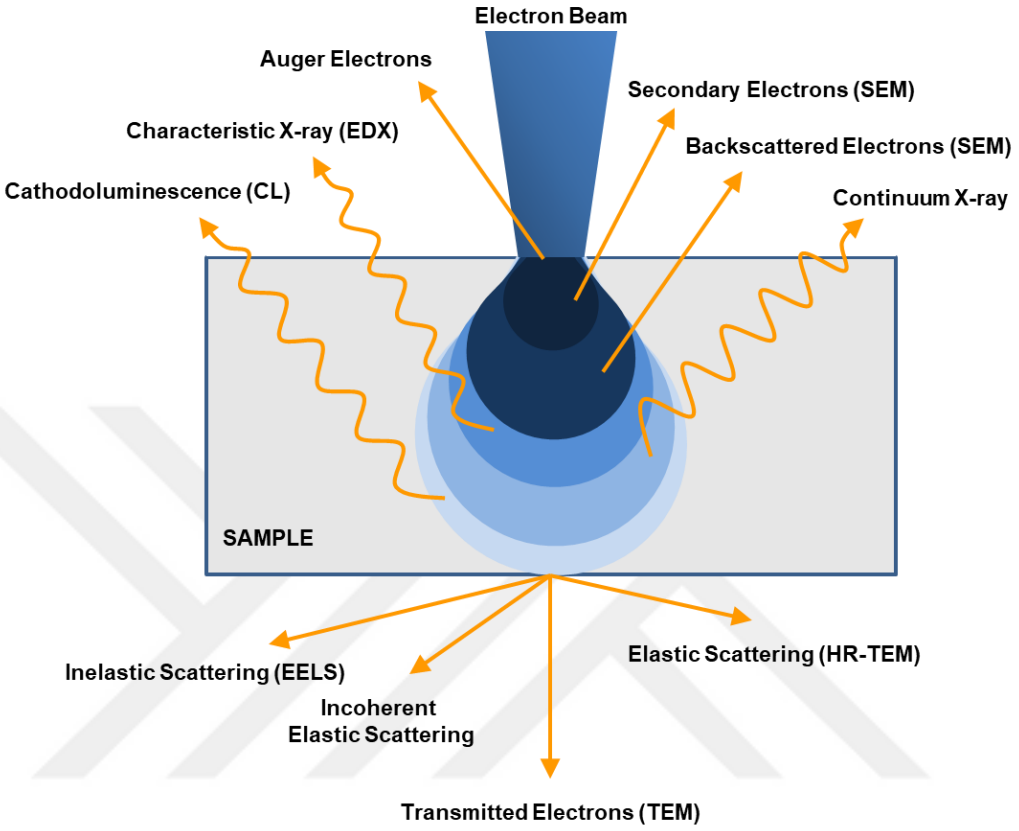

Figure 3.16 Interaction mechanisms illustrated for a highly energetic electron beam interacting with material. Different interaction mechanisms are used for different analysis methods. (SEM: scanning electron microscopy, TEM: transmission electron microscopy, HR-TEM: high-resolution TEM, EDX: energy dispersive X-ray scattering, CL: cathodoluminescence, EELS; electron energy loss spectroscopy)

3.5 Optical Spectroscopies

Similar to electron-material interaction mechanisms giving additional information on the inspected material, optical interactions can also provide further information about the electronic state of the material beyond imaging purposes. Photon-electron and photon-phonon interactions in semiconductors are useful in this regard. As discussed in Chapter

2, light absorption and emission mechanisms highly depend on the electronic structure of semiconductors. Their spectra reveal important information about the electronic and chemical structure of materials. For example, Raman and infrared absorption spectroscopies are complementary methods for the chemical structure analysis of materials exploiting photon-phonon interaction. In this subsection, we will briefly explain the optical spectroscopic methods used throughout this thesis. Absorption and photoluminescence (PL) spectroscopies are essential tools for nanocrystals and plasmonics research. Also, we will briefly explain the quantum efficiency measurement of luminescent materials, which is important for quantifying their intrinsic optical radiation performance of emitters with respect to the number of absorbed photons.

3.5.1 Absorption and Photoluminescence Spectroscopies

The basic working principle of absorption spectroscopy is illustrated in Figure 3.17. A broadband light source is spectrally filtered to obtain the desired wavelength. Light is collected after passing through a solution or solid sample. There is another monochromator at the collection end to ensure only the illuminating wavelength of the light is collected at the detector, which is critical especially for emissive samples. In this configuration, although we call it absorbance spectroscopy, what we measure is the optical transmission and the transmission is given by

$$T(\lambda) = \frac{\Phi_{tr}(\lambda)}{\Phi_0(\lambda)} = 10^{-Abs} \tag{3.9}$$

Here, $\Phi_{tr}(\lambda)$ and $\Phi_0(\lambda)$ are the transmitted and input light intensities, respectively. The absorption is found using $A = 1 - R - T - S$ where R is the reflection, T is the transmission and S is the scattering. In the case of dilute solutions of colloidal nanocrystals having negligible reflection and scattering, the assumption $T = 1 - A$ is valid. For plasmonic structures with sizes larger than 10 nm, the scattering becomes dominant and should be taken into account. Scattering spectra for these samples can be measured using methods similar to darkfield microscopy.

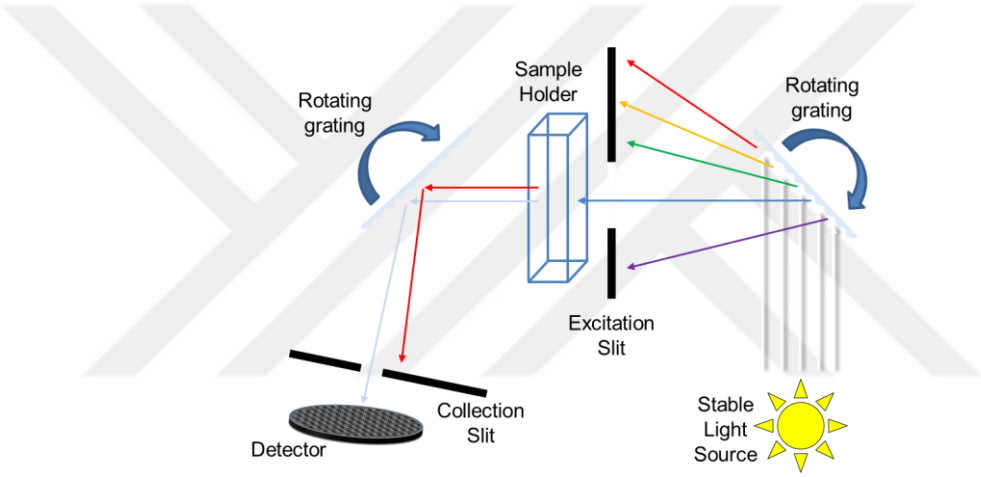

Figure 3.17 Absorption spectroscopy. Generally, a broadband excitation source is used. However, to avoid errors with the excitation, the collection wavelength should be the same as the excitation and, if any, emission wavelength should be rejected.

In PL spectroscopy, we excite the luminophores at a predetermined wavelength of light during the measurement. A collection-end monochromator unit scans the desired PL spectrum with a desired level of accuracy. The accuracy of the monochromatic system depends mainly on the width of the slit after the dispersive element and the quality of dispersive element, which can be a holographic grating. Generally, the collection end of PL spectrometers is not placed in the excitation light path to avoid highly intense excitation light. While the absorption spectrum captures information on

every electron and phonon interaction mechanisms, the PL spectroscopy provides information only on the radiative interaction. In principle, it is possible to resolve each transition energy in a nanocrystal, however, distinct energy peaks are screened with exciton-phonon interactions. Exciting nanocrystals with energies just above the energy bandgap at cryogenic temperatures allows to observe these distinct transitions. This method is called florescence line-narrowing spectroscopy. Although we did not use this method in this thesis, mentioning it here is important to understand the potential of PL spectroscopy.

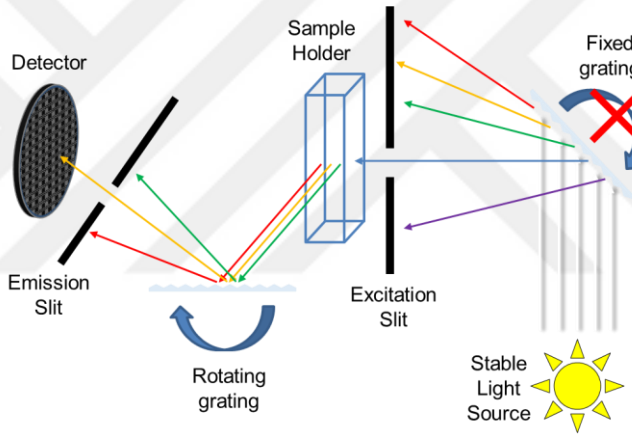

Figure 3.18 Emission spectroscopy. A fluorophore is excited via a selected wavelength band of a broadband source. During this fixed excitation, the PL spectrum is scanned.

Photoluminescence excitation (PLE) spectroscopy can be considered as the combination of absorption and PL spectroscopies. As illustrated in Figure 3.19, while tracking the light intensity at the desired emission wavelength, the excitation wavelength is scanned. In this way, it is possible to reveal the absorption features contributing the emission process at the desired emission wavelength. PLE is especially important to analyze the underlying absorption features contributing to PL. In Chapter 5, as a direct

evidence, we used PLE to show Cu PL emission in our Cu-doped colloidal quantum wells, which we found is originating from the NPL absorption and not any other formed nanocrystal in the solution. The PLE is used to identify heterogenous PL broadening effects in QDs that may not be monodispersed. For QDs having broad size distributions, different parts of PL emission gives different PLE spectra.

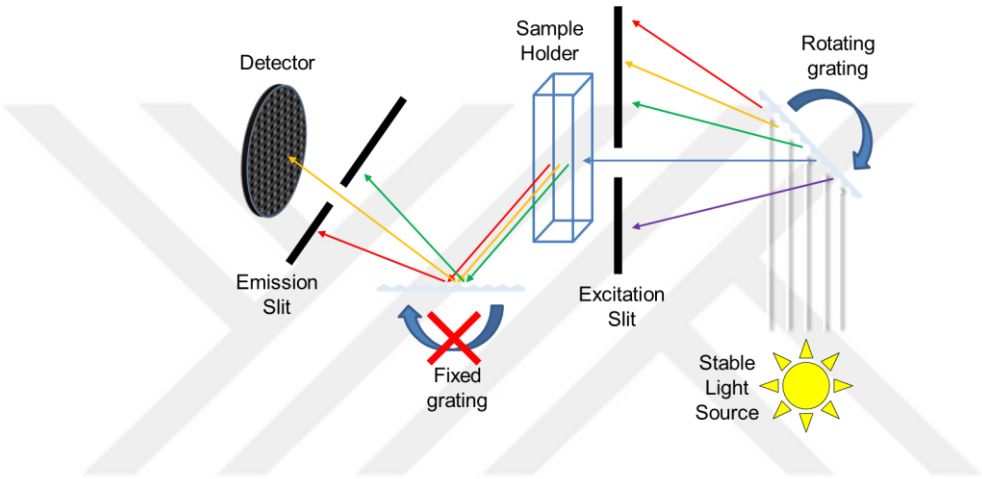

Figure 3.19 Photoluminescence excitation (PLE) spectroscopy. In contrast to PL spectroscopy, here the fluorophore emission wavelength is fixed. With the emission collected at this fixed wavelength, the excitation wavelength is scanned, and the PL intensity is recorded for tuned excitation wavelength.

3.5.2 Absolute Quantum Efficiency Measurement

Most of the semiconductor nanocrystal applications require a high PL efficiency. To quantify the PL efficiency of emitters, relative and absolute PL quantum efficiency (PL QE) measurements are commonly used. The relative PL QE measurement requires a reference dye emitting at the similar wavelength range of a tested emitter. Considering the absorption and emission intensities of the reference dye and the emitter under the test, the ratio of absorbed and emitted photons give a relative PL QE. However, this

method requires a different dye for each measurement and the reference dye's absorption and emission spectra should cover those of the emitter. For example, highly engineered nanocrystals can produce large Stokes-shifted emission, which can be challenging to characterize in relative PL QE measurements. Instead, using an integrating sphere, it is possible to measure the absolute PL QE of any emitter with de Mello method. [55] the absolute PL QE characterization requires three different sets of measurements as shown in Figure 3.20. As the excitation source, a high-power Xe lamp output is passed through a monochromator to be filtered to obtain the desired excitation wavelength. Three different configurations are used for blank, sample and scattering measurements. In the blank measurement, there is no sample inside the integrating sphere. This allows to measure the number of injected photons. The sample measurement is the case where the excitation beam directly hits on the sample. The sample absorbs both the direct and scattered excitation light and emits light. The scattered excitation light is taken into account with the scattering measurement. Absorption coefficient $Absorb$ is then defined in terms of the excitation portion of the sample $\left(I_{sample}^{ex}\right)$ and the scattering $\left(I_{scattering}^{ex}\right)$ one follows:

$$Absorb = 1 - \frac{I_{sample}^{ex}}{I_{scattering}^{ex}} \qquad 3.10$$

Finally, the absolute PL QE η is calculated as

$$\eta = \frac{I_{sample}^{em} - (1 - Absorb) I_{scattering}^{em}}{I_{blank} Absorb} \qquad 3.11$$

where I_{sample}^{em} and $I_{scattering}^{em}$ are the emission portions of the sample and the scattering measurements and I_{blank} is the integrated intensity of the blank measurement. The excitation and emission portions of a PL QE measurement is shown in Figure 3.21 for a 81% efficient nanocrystal sample. At our laboratory, we used a custom-built PL QE system calibrated with an optical powermeter over the 300-1100 nm range. We used several reference dye measurements and in the visible region, our error is limited within ±2%. For a reliable absolute PL QE measurement, the reabsorption effects must be minimized, hence, we should work with dilute solutions of the nanocrystal samples. Generally, the overall $Absorp$ coefficient smaller than 0.1 gives reliable results. However, it is the best to measure PL QE for a wide range of concentrations and observe the change accordingly.

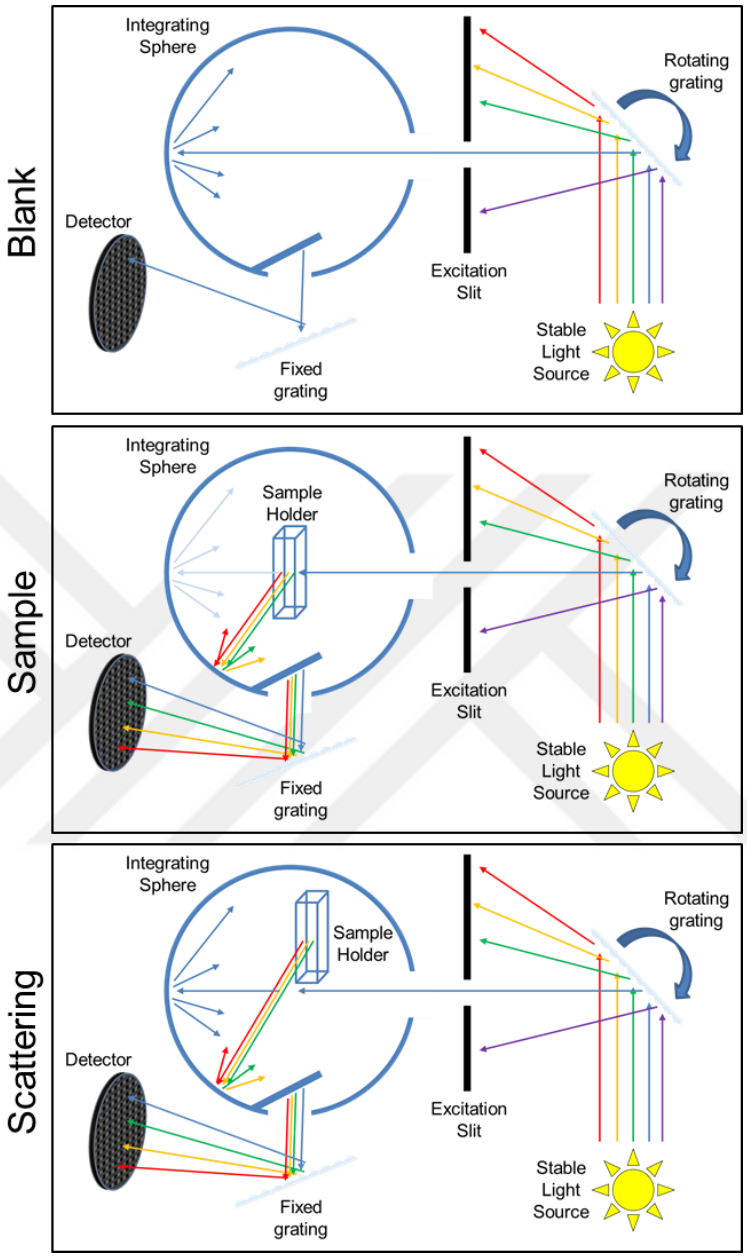

Figure 3.20 Three configurations of the absolute PL QE: the blank, sample and scattering measurements are illustrated.

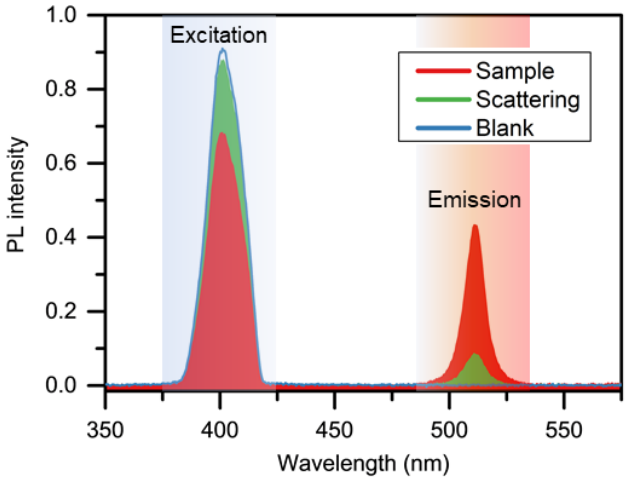

Figure 3.21 Exemplary spectra for the absolute PL QE calculation. Blank, sample and scattering spectra are shown with the excitation and emission portions.

Chapter 4

Polarized Color Conversion of Colloidal Nanocrystals Coupled to Plasmonic Surfaces

This section is based on the publication “Strongly Polarized Color Conversion of Isotropic Colloidal Quantum Dots - QDs Coupled to Fano Resonances of v-Grooved Plasmonic Surfaces for Next-Generation QD-TVs,” **K. Gungor**, O. Erdem, B. Guzelturk, E. Unal, M. Sak, S. Jun, E. Jang, and H. V. Demir. (in submission)

Colloidal nanocrystal, also commonly known as colloidal quantum dots (QDs) offer high color purity important for liquid crystal displays (LCDs), stimulating color enrichment in LED-lit LCD-TVs. However, in LCDs requiring polarized backplane illumination, highly polarized light generation using inherently isotropic QDs remains a fundamental challenge to date. In this thesis, we show strongly polarized color conversion of isotropic QDs coupled to Fano resonances of v-grooved plasmonic surfaces compatible with surface-normal LED illumination for next-generation QD-TVs. This architecture overcomes the critically oblique excitation of SPPs by using v-shapes imprinted on the

backlight unit (BLU). Using intrinsically isotropic QDs (with an initial contrast ratio of unity) coated on v-BLU surface, we experimentally measured a high degree of polarization at the farfield reaching a contrast ratio of 10 enabled by Fano resonance coupling. Full electromagnetic solution shows Fano line-shape transmission in transverse magnetic polarization allowing for higher transmission as an indication for forward scattering configuration. Of these QDs coupled to the SPP modes, we observed strong modifications in emission kinetics revealed by time-resolved PL spectroscopy and dipole orientations identified by BFP imaging. This collection of findings indicates conclusively that these isotropic QDs are forced to radiate in polarized state from the patterned planar surface under surface-normal excitation. Finally, we developed a template-stripped QD-based v-BLU plasmonic plastic sheet for a proof-of-concept demonstration of a front-panel display working under backlight illumination. These results show that direct integration of the proposed polarized light-emitting isotropic QDs into bendable electronic displays is possible for next-generation QD-TVs.

4.1 Motivation and Review

Liquid crystal displays (LCD) revolutionized the display market. The compact structure of LCDs compared to cathode ray tube screens increased the application areas and quality of displays. In most advanced LCDs, a back-illuminating light source (typically blue light-emitting diodes - LEDs) is used to excite color converting materials placed behind the liquid crystal cells (LCC). A rear polarizer is placed between the color converting layer and LCCs. LCCs change the polarization state of linearly polarized light passed from the rear polarizer, which clips the undesired polarization of color-converting material emission and remaining blue back-light illumination. Another polarizer in the

front-plane of the LCD selectively passes only the light with polarization state modified by LCCs. Finally, a color filter is used to create color selective pixels. Color filters are critical for the color rendering quality of LCDs. During the display operation, each optical component (polarizers, color filters, color converting materials) induces an inherent loss and significantly reduces the efficiency of LCD unit. The use of rear polarizer causes at least 50% loss of the backlight, which limits the overall efficiency of the displays. Therefore, polarized light emitting backlight sources can potentially boost the overall efficiency of current LCDs making them highly desirable for the display manufacturers.

Colloidal semiconductor QDs possess spectrally tunable features including narrow PL emission and broad absorption profile. [56] Decades of research resulted in high stability, [57] near-unity efficiency [58], [59] and spectrally engineered pure color-emitting QDs [59], [60]. Their narrow PL emission eliminates the requirement of color filters with a careful spatial placement of QDs, which can be done with established inkjet printing, transfer printing [61] and novel lithographic techniques. [62] High in-film efficiency of QDs is another advantageous feature compared to conventional color converting phosphorus. Also there are major supply concerns for rare-earth materials crucial for phosphorus materials. [63] In contrast, wide availability and material choice alternatives for QDs make solution-processed QDs ideal color converting materials. The QD-based backlights in the LCDs can favorably enhance the color gamut as compared to the ones that use phosphor based color converting backlights. [64]–[66] Considering the listed advantages, QDs have attracted great interest from the display industry and QD-enhanced LCDs are dominating the display market. [7]–[9], [59], [67], [68] Still, the LCDs based on the QD-backlights suffer from the randomly polarized light of

isotropic QDs similar to phosphor-based LCDs which requires utilization of rear polarizer. In this thesis, we developed a novel plasmon-nanocrystal composite surface to generate polarized light from isotropic nanocrystal emitters. With proposed structure, it is possible to design ultra-thin, bendable and uniform displays incorporated with any type of nanocrystal emitter.

Efforts to achieve polarized light generation in semiconductor nanocrystals mainly focused on the shape modification and emission control of the emitters. Anisotropic nanocrystals inherently emit partially polarized light in a single particle level; [69] however, they require aligned immobilization on the surface making them impractical at large scale. [70] Polarized emission of rod-in-rod nanocrystals in a stretched polymer film have been reported, however, this method is not flexible in terms of luminophore choice and utilizes only the anisotropy coming from the absorption characteristics. [71] Thanks to their strong interaction with impinging electromagnetic field, metallic grating structures are used as polarizing structures for light generation. Nevertheless, there is a trade-off between transmission and anisotropy values for reported metallic grating structures aiming polarized light creation. [72]–[74] For high polarization contrast ratio of 50, limited transmission is observed. [73] Here, polarization contrast ratio (CR) and corresponding polarization anisotropy (r) are defined in terms of TM (I_{TM}) and TE (I_{TE}) polarization PL intensities as

$$CR = \frac{I_{TM}}{I_{TE}} \tag{4.1}$$

$$r = \frac{I_{TM} - I_{TE}}{I_{TM} + 2I_{TE}}$$

4.2

In addition to limited transmission, metal grating coupling causes a PL wavelength shift which can create undesired effects in display operation. [72] Photonic crystal cavities are used for optical density of states manipulation of the quantum emitters. Although photonic crystal cavities showed high CR performance, these efforts remained in the single particle level. [75] Plasmonic coupling is another strong light interaction mechanism for optical density of states control over the quantum emitters. Gold nanorods coated with emitters [76] suffer the inhomogeneity problem and requirement of nanoparticle alignment on the surface. Highly polarizing plasmonic nanohole antennas suffers from low transmission values. [77] Plasmonic grating coupling of QD emission shows a polarization multiplexing capability for different emitters, however, the requirements like excitation through a small aperture and epitaxial thick silver films reduce transmission. [78] Like polymer stretching to overcome time-consuming and costly nanofabrication routes, magnetically aligned gold nanorods with nickel endings provide CR of 15 but inhomogeneity of the film surface is a limitation for practical applications. [79]

4.2 Working Principle

To overcome losses of polarized light generation, engineering the emission kinetics of emitters is a promising approach. PL decay engineering using all-colloidal plasmonic cavities to achieve anisotropic emission has been reported, however, having limited CR values of 2.05 ($r = 0.26$) and oblique illumination requirement of these cavities limit

their use in the display backplanes. [80] Surface plasmon coupled emission (SPCE) is another strong polarization dependent mechanism for various fluorescent molecules and quantum emitters. [81], [82] However, SPCE mechanism suffers from light emission only at a specific angle. In our work, we exploited strong polarization dependence of SPCE mechanism for front-panel compatible applications of polarized light emitting QD surfaces.

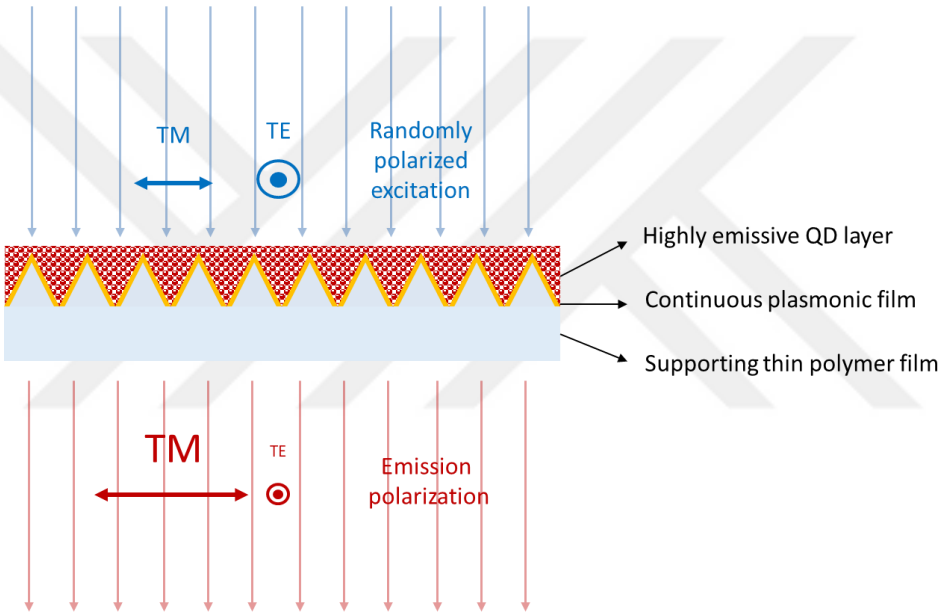

Figure 4.1 Working principle of the v-grooved surface utilizing SPCE for highly polarized light generation at surface normal direction.

Ultra-thin metallic films can support surface plasmon-polariton (SPP) modes having strong polarization dependence. However, SPP modes can be excited under oblique illumination. Our design overcomes the oblique illumination requirement by using v-shaped grooves patterned on the surface. Strong coupling between SPP modes and isotropic QDs results in polarized emission from planar surface under surface-normal excitation. As illustrated in Figure 4.2, direct integration of isotropic QDs to front-panel

displays will be possible for polarized mode operation. Blue light emitting diode emission excites isotropic QDs deposited on the surface of v-shaped backlight unit (v-BLU). Polarized emission of QDs coupled to v-BLU passes through LCCs and front polarizer selectively passes the desired polarization state. Our proposed v-BLU surface replaces two components in conventional LCDs: color converting layer and rear polarizer which wastes half of the emission.

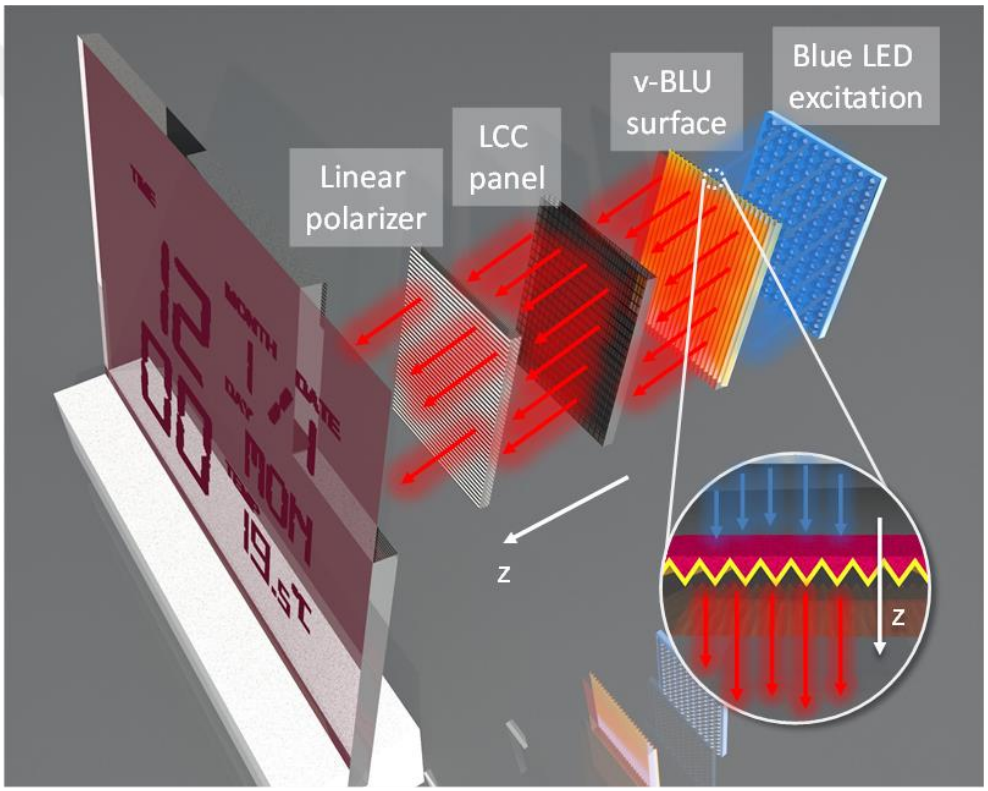

Figure 4.2 Proposed display architecture of v-BLU surface. Randomly polarized blue LED in surface normal configuration excites isotropic QDs on the v-BLU surface, however, emitted light from the QDs integrated intimately with the v-BLU is strongly linearly polarized towards liquid crystal cells. Inset figure illustrates excitation configuration of proposed v-BLU design.

4.3 Fabrication of v-BLU Structure

v-BLU surface fabrication requires a mold for replication process. Several new replicates can be stripped off from the mold surface reducing the fabrication costs for commercial applications. Fabrication of the v-BLU is illustrated in Figure 4.4a. V-shape of grooves is created by exploiting the crystallographic plane-selective etch rates of single crystal silicon wafer. We used several nanolithography techniques for mold fabrication including of electron beam lithography, dry- and wet-etching steps and silanization process to reduce surface energy of the mold. [83]–[85] After the thermal deposition of thin plasmonic layers on mold, replicates are stripped off with the micrometer-thick support polymer layer. QDs are then spin-casted on the replicates. Cross-sectional SEM images of the mold (Figure 4.4b) and replicate (Figure 4.4c) are showing a high-quality replication process using template stripping method.

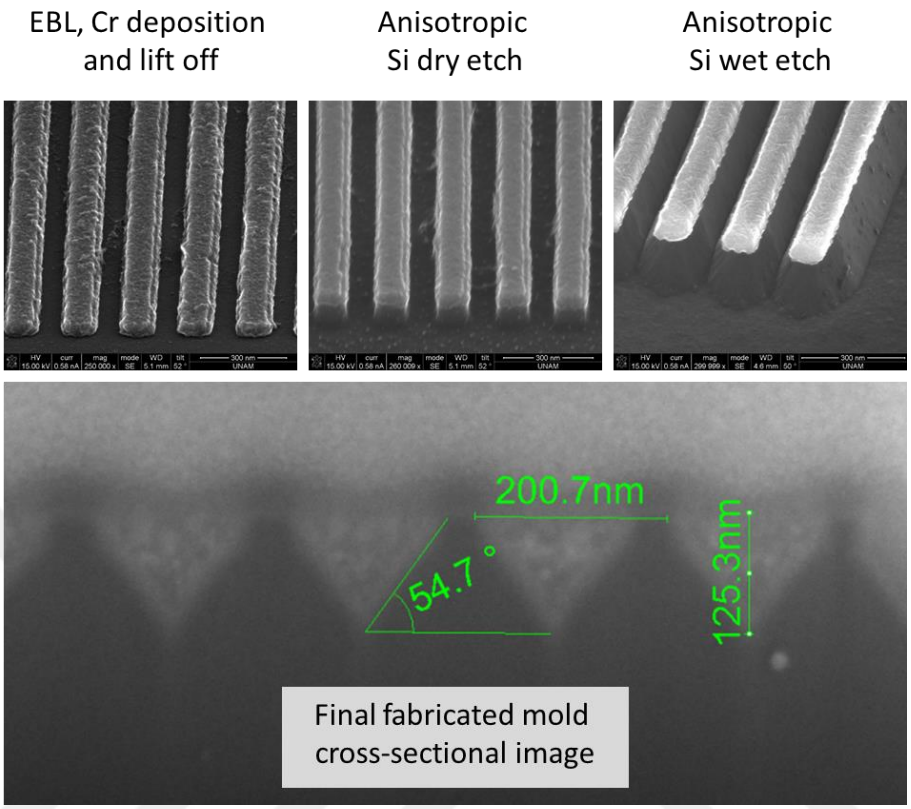

Figure 4.3 Fabrication steps for mold with v-grooved surface features are shown. Starting with the pattern definition using EBL and consecutive Cr deposition and liftoff serves as protective layer for anisotropic dry etching step. After highly anisotropic silicon dry etch using ICP-RIE, modified anisotropic KOH wet etch of silicon defines the v-groove features on silicon surface. Finally, characteristic 54.7° angle is observed under cross-sectional imaging.

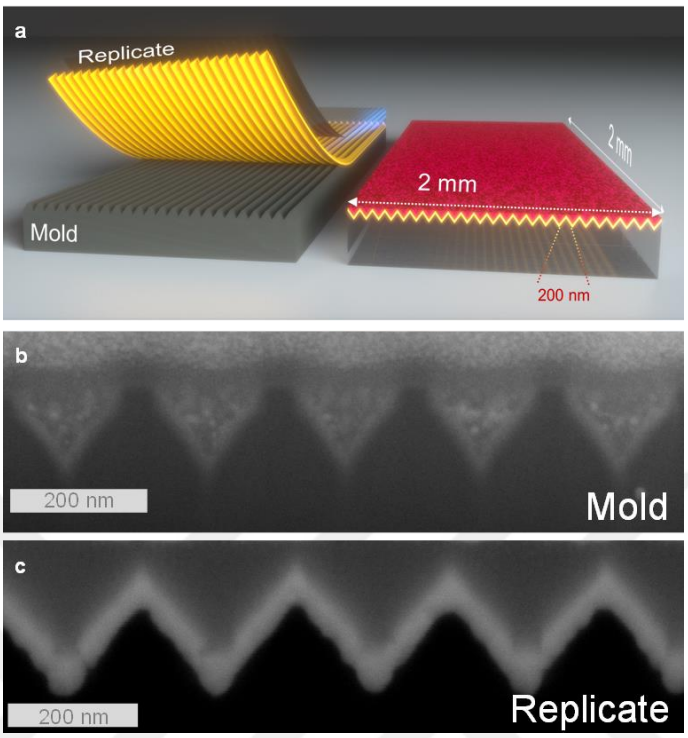

Figure 4.4 (a) Illustration of the developed fabrication method and final structure of the proposed v-BLU. After metal layer deposition, v-BLU together with support layer polymer is stripped off from silicon mold. (b) Cross-sectional SEM image of the fabricated mold structure. (c) Cross-sectional image of the replicated gold v-BLU with QDs.

4.4 Plasmonic Characterization of v-Grooved Surface

4.4.1 Optical Transmission Spectral Characterization of v-BLU

Optical transmission spectra of gold v-BLU before and after QD layer deposition are presented in Figure 4.5a. Depending on the thickness of QD layer, plasmonic response of the structures is changing. Due to effective refractive index increase, a redshift in the

position of SPP resonance is expected. [30] TE mode is similar to plain gold film response as shown with gray background. This similarity is expected since the impinging electromagnetic radiation will experience no surface feature in TE polarization. Figure 4.5b shows the TM/TE transmission ratio of the gold structure before and after QD deposition. For both thin and thick QD depositions, we have a TM/TE ratio of ~5 at 620 nm wavelength, which is the PL emission peak wavelength of our red emitting QDs. If our v-BLU design was only clipping a portion the rejected polarization, both thin and thick deposition of QDs would provide similar CR. Gray dashed-line in Figure 4.5b presents flat gold film TM/TE ratio being unity as expected. Definition of TM and TE polarizations under surface normal excitation for plain gold is degenerate and this unity TM/TE ratio shows that there is no inherent anisotropy originating from measurement setup. To further understand the polarization response of the v-BLU, numerical simulation of only gold structure without QDs is performed and presented in Figure 4.7a. The simulations for TM and TE polarizations agree well with the experimentally measured transmission.

To further extend the polarization capabilities of v-BLU to the green region of visible spectrum, a silver v-BLU is fabricated. Considering the surface plasmon resonance frequency, the silver v-BLU can be used for green QDs without further optimizing our mold structure to achieve polarized emission in green region. In Figure 4.6a, silver v-BLU transmission response before and after QD deposition is shown. Similar to gold v-BLU, we observed an increase and red-shift in transmission response after QD deposition. At the green QD peak emission wavelength (540 nm), the silver v-BLU gives TM/TE transmission ratio of ~7 (Figure 4.6b). Numerical simulation of transmission spectra is in agreement for TM and TE polarizations with experimental measurements

as shown in Figure 3f. Another observation is the similar transmission line-shapes of silver v-BLU and gold v-BLU TM polarizations. This observation suggests that the transmission line-shape of TM polarization is characteristic to v-BLU design.

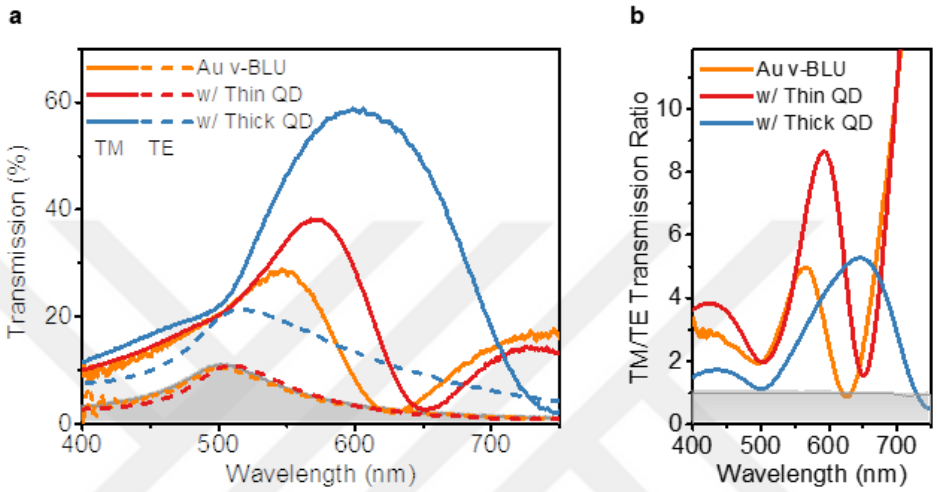

Figure 4.5 (a) Transmission spectra of gold v-BLUs having different red QD layer thicknesses. Thicker QD layer results in red-shifted and increased transmission response for TM polarization. TE polarization for thin QD layered structures is similar to flat gold film transmission response plotted in gray shaded curve. (b) Transmission TM/TE ratio for gold v-BLU shows an increased polarization performance for structures with QDs. Around red QD emission peak wavelength (620 nm) TM/TE ratio is ~5 for both structures. Gray shaded curve of flat gold film TM/TE ratio is unity as expected.

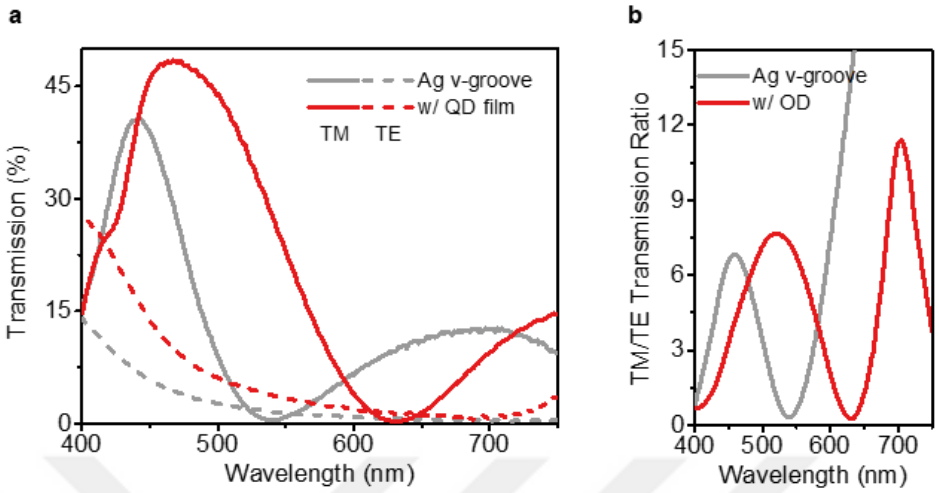

Figure 4.6 (a) Transmission spectra of silver v-BLU before and after green QD layer deposition. Presence of QD layer results in red-shifted and increased transmission response for TM mode similar to gold v-BLU. (b) Transmission TM/TE ratio for silver v-BLU shows an increased polarization performance after QDs deposition. Around green QD emission peak wavelength (540 nm) TM/TE ratio is ~7.

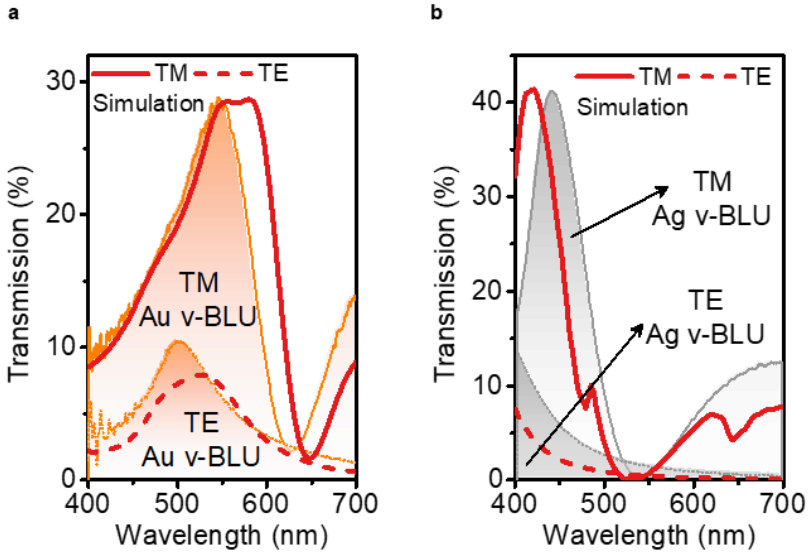

Figure 4.7 (a) Experimental and simulated transmission spectra of gold v-BLU. (b) Experimental and simulated transmission spectra of silver v-BLU.

4.4.2 Numerical Simulations and Fano Resonance Line-shape

Before and after QD deposition, transmission spectra of gold and silver v-BLUs follow typical Fano resonance forward scattering line-shape. [86]–[89] In forward-scattering Fano resonance, there should be an enhanced transmission for frequencies higher than the resonance wavelength and below the resonance wavelength, transmission should decrease considerably. Impinging electromagnetic field intensities are mapped for simulated gold v-BLU in Figure 4.8. For TE polarization, there is no significant change in transmission regardless of the wavelength. In contrast, different wavelength points in TM polarization transmission spectra shows distinct intensity maps. Without QD deposition, gold v-BLU features a resonance wavelength around 615 nm for TM polarization. Field maps show increasing transmission for 550 and 580 nm wavelengths which features a forward scattering pattern. At 615 nm, transmission spectrum changes its shape and wavelengths higher than the resonance wavelength features a reduced transmission. This reduced transmission is clearly observed in intensity maps for higher wavelengths. Another observation is the stark contrast between field intensity magnitudes for TM and TE polarizations between v-grooves where QDs are deposited. In addition to transmission selectivity for different polarizations, increased electric field intensity enhances optical mode density for QDs in TM polarization.

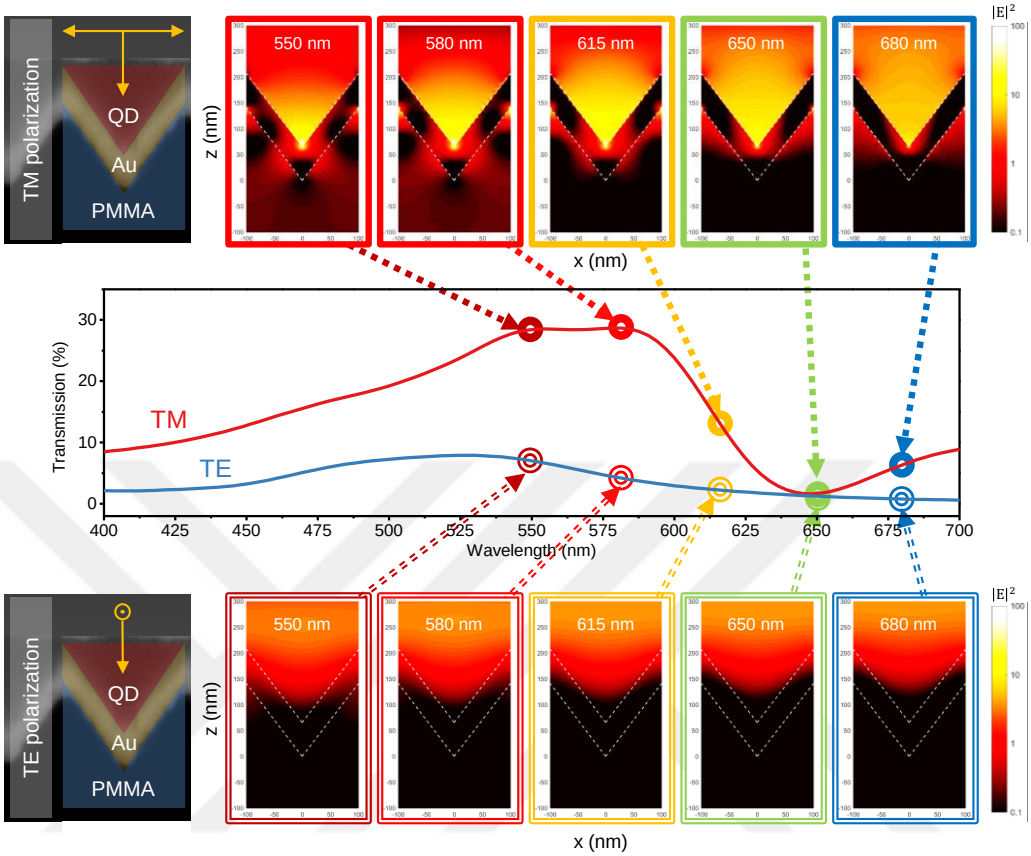

Figure 4.8 FDTD modeling of gold v-BLU without a QD layer. TM and TE polarization orientations are illustrated on the left and when deposited on v-BLU, the position of QDs are shown in red color. TM polarization transmission response resembles Fano type resonance line shape and observed higher transmission for higher energies is an indication for forward scattering configuration. Electric field intensity maps are showing increased transmission for the lower wavelengths than resonance wavelength of 615 nm. Also, the gap where QDs are deposited shows an increased electric field intensity, which increases the optical density of states for QDs. TE polarization shows no sign of strong resonance behavior and both transmission and electric field density values are significantly lower than TM polarization.

4.5 Photoluminescence Characterization of Coupled QDs

4.5.1 Steady-State Polarization Dependent Photoluminescence Measurements

After analyzing transmission polarization response of v-BLUs, we measured their steady-state farfield PL under different polarizations. Measurement setup is similar to LCD operation as illustrated in Figure 4.9. We used 400 nm linearly polarized laser source to excite v-BLUs with a 45° to groove directions ensuring the excitation of both TM and TE polarization states equally. The laser excites the QDs at normal incidence and PL of QDs is collected after rotating the analyzer at different angles. Absorption and PL of green ($\lambda_{PL} = 540\ nm$) and red ($\lambda_{PL} = 620\ nm$) QDs are presented in Figure 4.10 with the TM polarization transmission spectra of silver and gold v-BLUs, respectively. In Figure 4.13, TM and TE polarization PL spectra for green and red emitting QDs show the intensity difference and unchanged PL peak wavelength for perpendicular polarizations. PL peak wavelength change is an undesired response observed in grating structures and other plasmonic cavities. [72], [80] PL intensity change of the thin red QD film-gold v-BLU under different analyzer angles is shown in Figure 4.11. Integrated PL intensity follows a cosine square shape as expected with 180° periodicity. CR obtained from the cosine square fit is 9.70 giving an anisotropy value of 0.74. Gray spheres show the integrated PL intensity of QDs on flat gold film and as expected there is no inherent anisotropy coming from the measurement setup. Higher PL intensity value of TM polarization on v-BLU is a combination of higher transmission and increased electric field intensity as shown in Figure 4.8. For green QD-silver structure we have a

CR of 4.32 as shown in Figure 4.12, which corresponds to r = 0.53. Observed CR of red QDs coupled to gold v-BLU in steady-state PL is almost two times the expected PL from transmission measurements. This higher CR indicates that the v-BLU does not simply clip the TE mode emission but enhances the TM polarization emission.

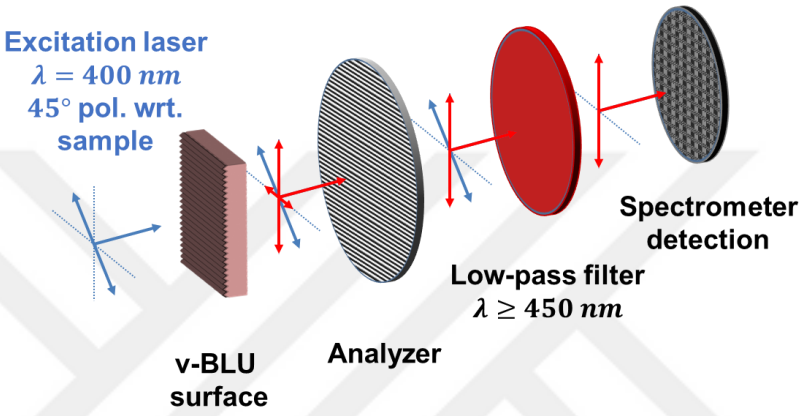

Figure 4.9 Farfield polarization dependent PL intensity measurement setup. Similar to LCD operation mechanism, emitted light of isotropic QDs coupled to v-BLU passes through an analyzer and a color filter to cancel out laser light. Using a spectrometer, we measure the intensity spectrum of the under different angles of the analyzer. Laser excitation polarization is 45° to the groove directions ensuring equal excitation of both TM and TE polarizations.

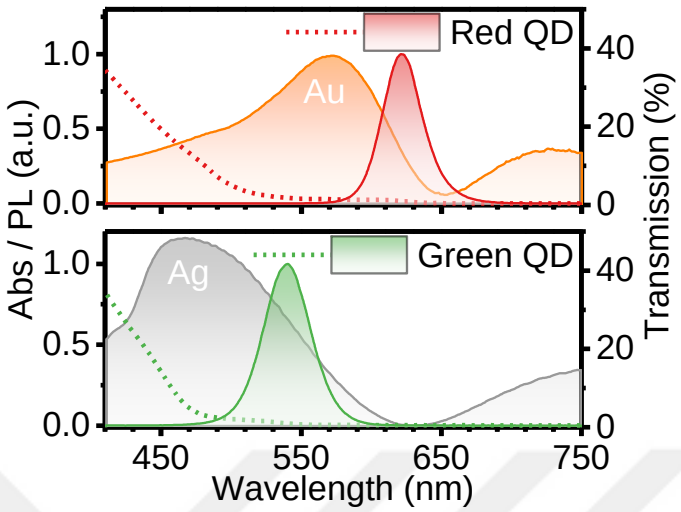

Figure 4.10 Absorption and emission spectra of red (λ_{PL} = 620 nm) and green (λ_{PL} = 540 nm) QDs used in this study are shown with corresponding TM polarization transmission spectra of gold and silver v-BLUs.

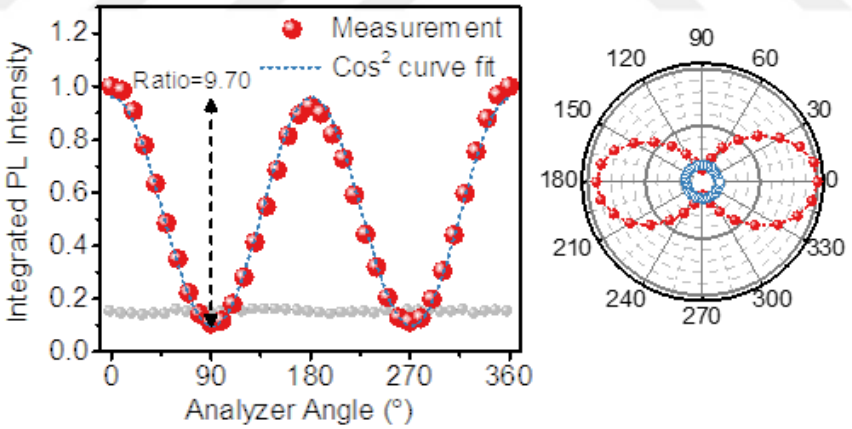

Figure 4.11 Analyzer angle dependent PL intensity for red QDs follows a well-defined $\cos^2$ dependence with CR=9.70. Gray spheres are PL intensity of QDs on flat gold film and the absence of $\cos^2$ dependence is an indicator for the absence of measurement system related anisotropy.

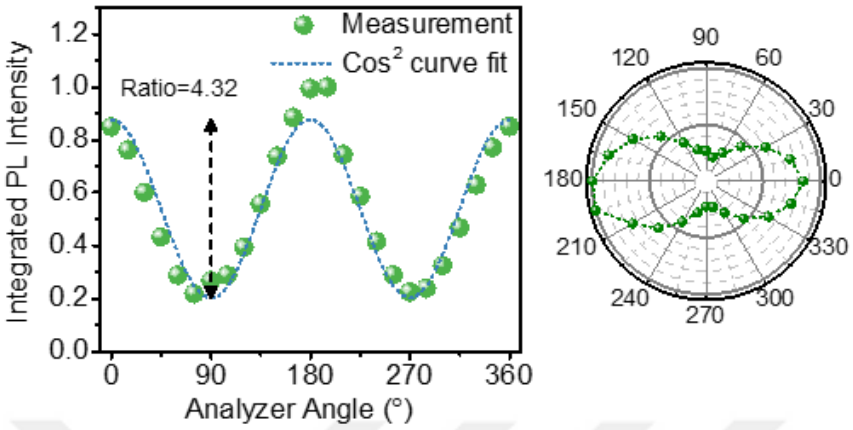

Figure 4.12 Analyzer angle dependent PL intensity for green QDs follows a well-defined $\cos^2$ dependence with CR=4.32.

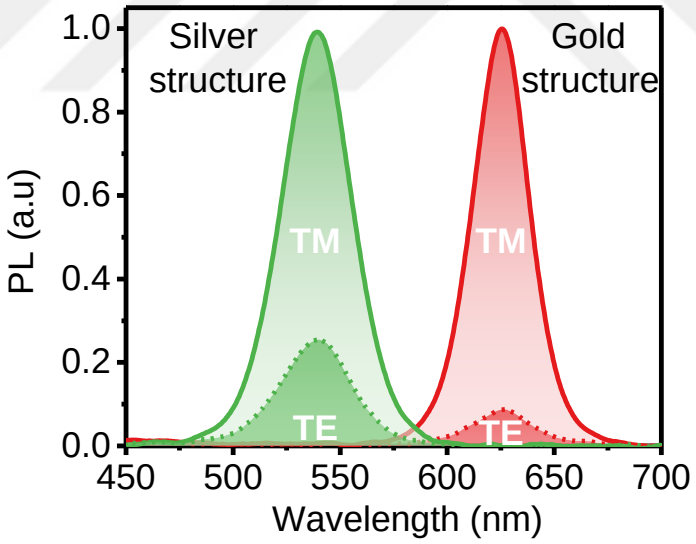

Figure 4.13 Maximum and minimum PL spectra of red and green QDs in TM and TE polarizations showing high CR and no significant peak wavelength change.

4.5.2 Emission Kinetics Analysis of Plasmonically Coupled Quantum Dots

To overcome the loss mechanisms of conventional polarized light generation methods, emission control of emitters is crucial. When a rear polarizer is used, rejecting a specific polarization state of randomly polarized light causes losing half of the intensity. Control over the emission anisotropy of the quantum emitter can prevent these losses and increase the overall efficiency of displays. In the steady state PL measurements, red QDs on gold v-BLU show a high CR which cannot be simply explained by polarization selective transmission response of v-BLU. There must be a modification mechanism in the optical density of states for QDs in TM and TE polarizations. This modification mechanism can be observed by observing the emission kinetics of the emitter. Configuration for conventional anisotropy measurements are presented in Figure 4.14. This configuration cannot be used for in film measurements of our v-BLU surface. We need to define a G factor calculation configuration to avoid system related anisotropies. Our proposed anisotropy measurement configuration is presented in Figure 4.15. A nonpatterned QD film is used to calculate the G factor. To measure the two orthogonal polarization decays, we placed our v-BLU surface in 45° with respect to the excitation laser polarization. Then anisotropy is calculated as $r = (I_{TM} - GI_{TE})/(I_{TM} + 2GI_{TE})$ where $G = I_{TM}^{nonpatterned}/I_{TE}^{nonpatterned}$. In Figure 4.16, observation of PL decays of our QDs with and without interacting with v-BLU show a significant change in the PL decay kinetics. QDs without a plasmonic layer in their proximity have average lifetime of 10.08 ns. Under plasmonic interaction, the lifetime of the QDs reduces to 0.70 ns since flat gold layer increases the PL decay rate. TM polarization emission has

the highest decay rate ($t_{av} = 0.39$ ns) indicating increased density of optical states Since the stead-state PL measurements yielded PL intensity enhancement for TM polarization, higher decay rate of TM polarization emission can be attributed to the increase in the radiative decay mechanisms for QDs. As expected from transmission spectra in Figure 4.5 and steady-state PL measurements in Figure 4.11, TE polarization ($\tau_{av} = 0.61$ ns) and QD emission on flat gold ($\tau_{av} = 0.70$ ns) average lifetimes are similar. In addition to enhanced TM polarization emission, slightly lower PL intensity level and faster decay rate of TE polarization emission compared to QDs on flat gold film indicate that the strong influence of v-BLU forces isotropic QDs to emit polarized light. The calculated anisotropy value using these decay curves gives $r = 0.76$, agreeing well with our steady-state anisotropy measurement of $r = 0.74$.

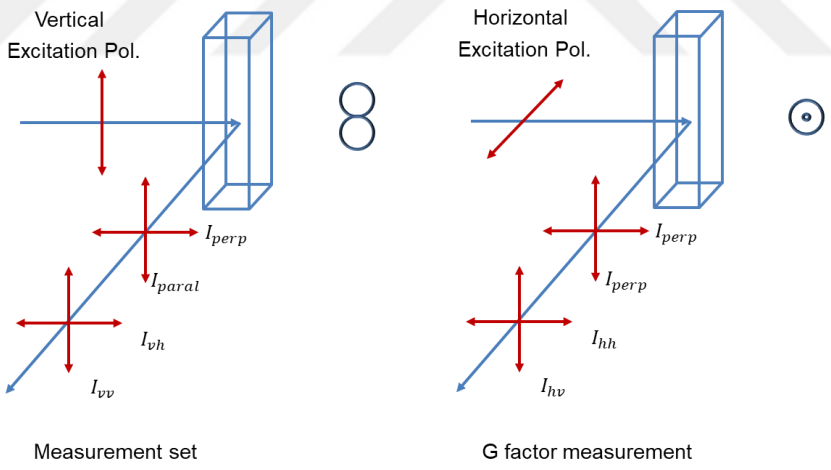

Figure 4.14 Conventional in solution anisotropy measurement configuration using time resolved fluorescence measurement setup. In vertical polarization excitation, only vertical dipole is created and allows to measure the anisotropy in this configuration. To eliminate the system related anisotropies G factor calculation is required. Created dipole in horizontal configuration is isotropic with respect to the collection end and any measured anisotropy must be system related.

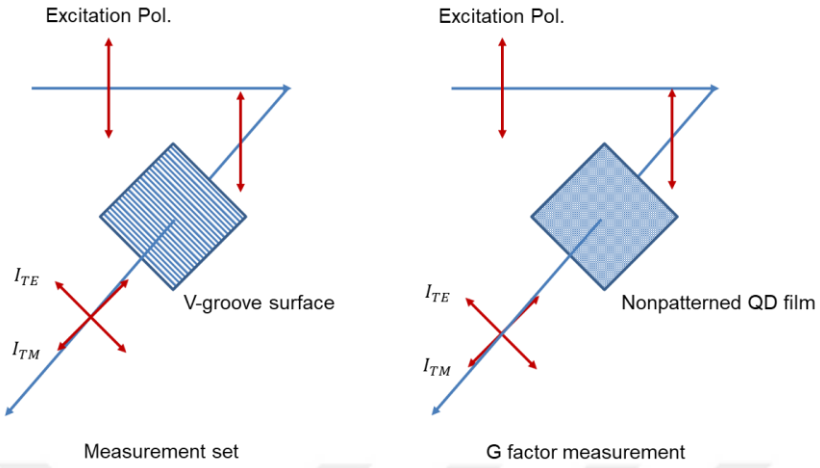

Figure 4.15 Our proposed anisotropy measurement configuration for in-film measurements. 45° placed groove orientation of the sample ensures the excitation both polarization states. G factor is calculated from nonpatterned QD film which would give 0 anisotropy inherently. TM and TE polarization measurements are corrected according to this measured G factor.

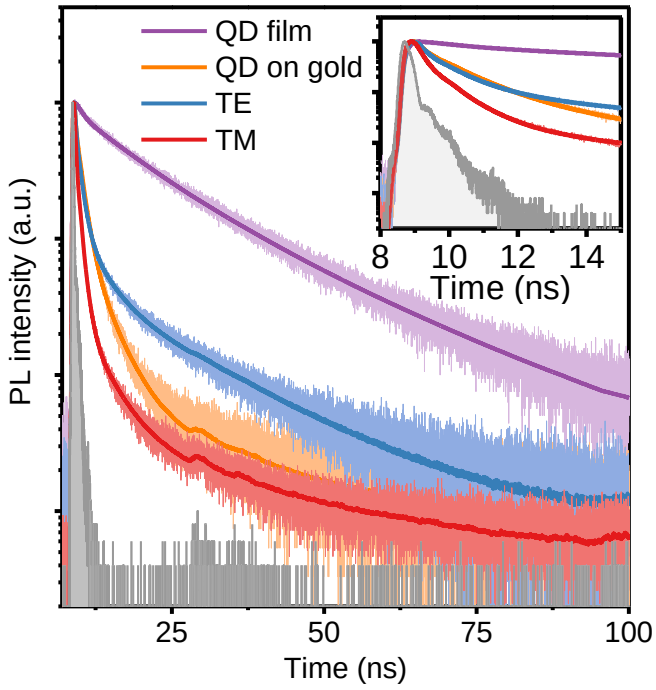

Figure 4.16 Time resolved fluorescence analysis of red QD films shows a strong modification in density of optical states for QDs. While average lifetime of plain QD film is 10.08 ns, decay rate increases when QDs are in a proximity of gold layer (for QDs on plain gold layer $\tau_{av} = 0.70$ ns). Increased PL intensity and the fastest decay ($\tau_{av} = 0.39$ ns) observed in TM polarization PL of QDs indicate a pronounced anisotropy which is measured as 0.76 from transient analysis agreeing well with steady-state measurements. Inset figure zooms into the initial times of the decay curves and shows similar transient response for TE polarization and plain gold film emissions. Gray curve corresponds to instrument response function of our measurement system.

4.5.3 Dipole Orientation of Quantum Dots when Coupled to Plasmonic Surface

A pronounced anisotropy in QD emission as a result of an anisotropic modification in the optical density of states is expected to change the emitter dipole orientation. BFP imaging is used to observe the dipole orientations of anisotropic emitters. [54], [90]–[92] In Figure 4.17a-f, BFP images of plain red QD film on fused silica, red QD film on plain gold layer and red QDs on gold v-BLU are shown under two perpendicular analyzer orientations. Plain QD film on fused silica BFP images (Figure 4.17a,b) show isotropic emission with a central spot surrounded by a brighter ring. The ring shape is due to critical angle and its Fourier space radius is close to k_0, where k_0 is free space wavenumber of the electromagnetic radiation. Considering the effective refractive indices of QD film ($n_{eff} \cong 1.8$) [67] and fused silica layer, we expect radius to be $0.81k_0$ which is close to observed BFP image. On the plane of incidence, isotropic QDs show no polarization response. QD film on plain gold layer (Figure 4.17c,d) shows characteristic narrow ring shape indicating strong angle-dependent directional emission at SPP coupling angle. [93] It is reciprocal to Kretschmann configuration of SPP

excitation: instead of exciting SPPs in gold film with a monochromatic light source impinging at a specific angle, QD emission is coupled to SPPs and radiation is observed at SPP angle at the backplane of gold film. Since only TM polarization can excite SPPs, SPCE of QD film is highly polarization dependent. However, TM polarization is dependent on the reference frame for plain gold film and this reference frame is dictated by analyzer orientation: when analyzer is rotated, rejected portion of TM polarization emission rotates as well. For the case of QDs coupled to gold v-BLU (Figure 4.17e,f), we observe distinctly different BFP images for two orthogonal analyzer orientations. In Figure 4.17e, analyzer cancels out TM polarization emission and we observe significant reduction in TE polarization emission in both k_x and k_y directions. In perpendicular analyzer orientation, TE polarization emission is cancelled and TM polarization can pass as illustrated in Supporting Information. This BFP pattern is observed in anisotropic molecular emitters. [53] In contrast to SPCE behavior, v-BLU fixes the reference frame for dipole orientation and angled walls of the grooves eliminates the undesired directional oblique emission observed in SPCE. We observe a central spot in v-BLU coupled BFP image of QDs indicating a surface normal emission which is important and desired feature for LCD operation.

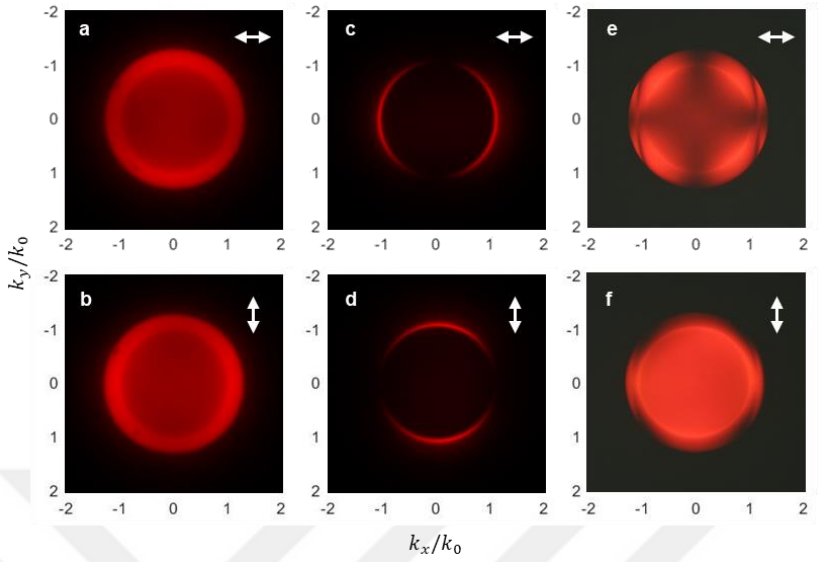

Figure 4.17 Dipole orientations of red QDs under different configurations are measured using BFP imaging: (a,b) QD film on fused silica, (c,d) QD film on plain gold layer and (e,f) QD film on gold v-BLU. QDs on fused silica and plain gold are isotropic for any analyzer angle. On v-BLU, when TM polarization is cancelled by analyzer in (e) PL emission in k_x and k_y directions are absent in BFP image indicating an orientated dipole. In vertical orientation of analyzer, dominant polarization is allowed to pass in all directions (f).

4.6 Proof-of-Concept LCD Application using v-BLU Backlighting

A proof-of-concept LCD application is realized by using red QD-gold v-BLU in the backplane replacing the rear polarizer. Fabricated bendable gold v-BLU with red QDs is shown in Figure 4.18. The structure consists of a thin gold layer, micrometer thick supporting PMMA polymer layer and Scotch tape to strip the replicate. To further reduce the artificial anisotropies related with measurement system, we fabricated two structures on the same substrate with perpendicular groove orientations. With spin-deposited red

QD layer, complete structure is bendable and light-weight. In Figure 4.19, v-BLU with a thick QD layer (expected CR = 5.6) is imaged behind an analyzer, under UV illumination and ambient lighting. On and off behavior is visible with analyzer rotation. At 45°, both QD emission and plasmonic structure reflection is similar for both orientations. Finally, by disintegrating a transparent LCD clock, we fabricated a display using our red-emitting v-BLU. We kept the LCD unit and front polarizer but replaced the rear polarizer with our v-BLU. Since the size was matching with the dimensions of our structures, we used “DATE” writing on the clock as illustrated in Figure 4.2. Under orthogonal orientations of rear polarizer, bright and dark areas of the writing interchanges as shown in Figure 4.20a,b. Using our structures having perpendicular orientations under UV illumination from backplane, we observe both configurations of the writing (Figure 4.20c). It is remarkable that letters are only visible in the areas where our structures are defined.

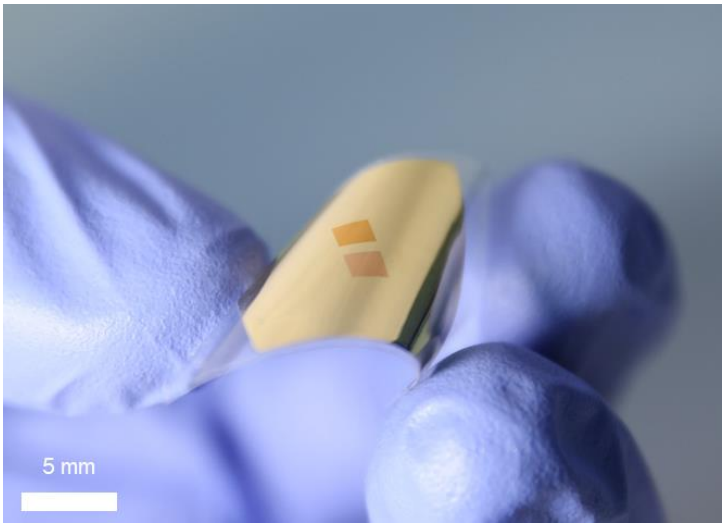

Figure 4.18 Fabricated bendable v-BLUs under ambient lighting. On the same film there are two structures with perpendicular groove orientations to minimize system and sample preparation related anisotropies.

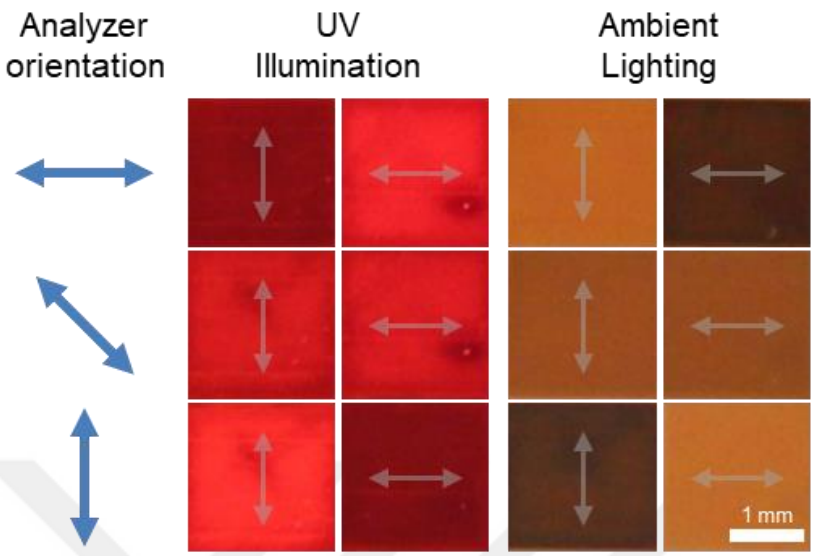

Figure 4.19 Analyzer dependent photographs of two structures on the same substrate: QD PL emission with UV back-illumination and reflection under ambient lighting. As expected perpendicular orientations of analyzer turn on and off each structure. At 45° the response of both structures is the same.

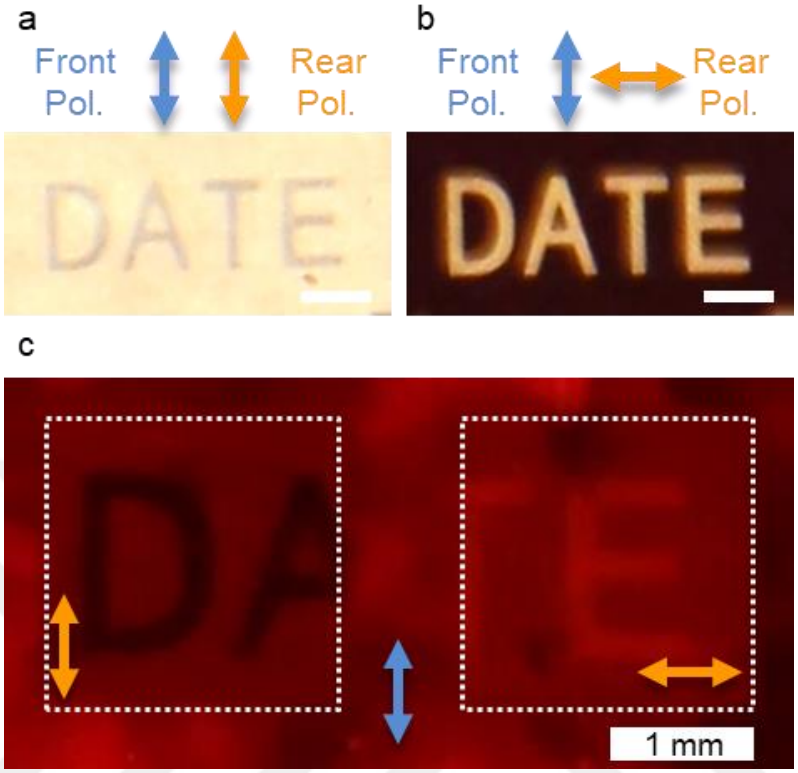

Figure 4.20 Rear polarizer orientation dependent letters on transparent LCD clock is shown to explain display operation. (a) Background is bright, letters are dark when front and rear polarizers are parallel. (b) Bright and dark areas are reversed when front and rear polarizers are perpendicular. (c) “DATE” writing is created using gold v-BLU with red QDs used as back illumination replacing the rear polarizer. Both configurations observed in (a) and (b) for orthogonal orientations of v-grooves on the same substrate. Letters are only visible on the structures indicating display operation enabled by the polarization response of v-BLUs.

4.7 Summary

Polarized light emission creation from isotropic QDs opens new possibilities for next generation displays. v-BLU plasmonic surface modifies the optical states density of QDs and forces them to emit anisotropically. Control over the decay kinetics and dipole orientation of isotropic QDs is instrumental to overcome optical losses caused by the

rear polarizer in conventional LCDs. Fabrication method developed for v-BLU allows for a bendable and polarized light generating color converting backplane illumination unit for LCDs. Observed CR of 9.70 is promising value for display applications and the proof-of-concept display demonstration using thicker QD film having 5.67 CR is supporting the possibility for practical display application of v-BLUs. It is possible to fabricate polarized LEDs using isotropic QDs as active layer with v-BLU architecture. With a proper material choice, continuous plasmonic film of v-BLU can act like one of the contact layers and induce anisotropy for density of optical states for QDs. In this respect, v-BLU is a promising design for next generation displays.

Chapter 5

Luminescent Solar Concentration of Colloidal Nanocrystals

This section is based on the publication "Near-Unity Emitting Copper-Doped Colloidal Semiconductor Quantum Wells for Luminescent Solar Concentrators," M. Sharma,* **K. Gungor**,* A. Yeltik, M. Olutas, B. Guzelturk, Y. Kelestemur, T. Erdem, S. Delikanli, J. R. McBride, and H. V. Demir, Advanced Materials (2017), vol. 29, no. 30, p. 1700821, Aug. 2017. Adapted (or "Reproduced in part") with permission from John Wiley and Sons. Copyright 2017 Wiley-VCH Verlag GmbH & Co. KGaA, Weinheim. (* equal contribution)

Doping of bulk semiconductors has revealed widespread success in optoelectronic applications. In the past few decades, substantial effort has been engaged for doping at the nanoscale. Recently, doped colloidal QDs have been demonstrated to be promising materials for luminescent solar concentrators (LSCs) as they can be engineered for providing highly tunable and Stokes-shifted emission in the solar spectrum. However, existing doped QDs that are aimed for full solar spectrum LSCs suffer from moderately low quantum efficiency, intrinsically small absorption cross-section and gradually

increasing absorption profiles coinciding with the emission spectrum, which together fundamentally limit their effective usage. In this thesis, we show the first account of copper doping into atomically-flat colloidal quantum wells (CQWs). In addition to Stokes-shifted and tunable dopant-induced PL emission, the copper doping into CQWs enables near-unity quantum efficiencies (up to ~97%), accompanied by substantially high absorption cross-section and inherently step-like absorption profile, compared to those of the doped QDs. Based on these exceptional properties, the authors have demonstrated by both experimental analysis and numerical modeling that these newly synthesized doped CQWs are excellent candidates for LSCs. These findings may open new directions for deployment of doped CQWs in LSCs for advanced solar light harvesting technologies.

5.1 Motivation and Review

Luminescent solar concentrators (LSCs) are light-harvesting devices that are expected to be a cost-effective alternative to optics-based solar concentrator systems. [11], [13], [94] In contrast to expensive optics-based concentrators, LSCs offer the capability to absorb both direct and diffused sunlight by its embedded fluorophores that exhibit reemission at longer wavelengths. Generally, LSCs are composed of plastic optical waveguides containing highly luminescent fluorophores or glass slabs coated with active layers of emissive materials. [94]–[96] Under solar illumination, the fluorophore's emission is guided and concentrated towards the edge of the slab waveguide through total internal reflection. This emission is then collected and converted to electricity by photovoltaic (PV) cells placed at the thin edges of the waveguide, thus allowing for large-area solar light harvesting with small-area PVs. [94], [95] Therefore, LSCs are

promising candidates for lowering the solar energy costs by increasing the incident radiation flux with large area of the LSCs exposed to the sunlight, which in turn can augment photogenerated power output in PVs. [13], [94] Additional increase in the power output of a PV cell has recently been targeted further by matching the emission wavelength of LSC emitters to that of the spectral efficiency peak of a given device. [97], [98]

Colloidal luminescent NCs have been shown to be highly promising materials for their utilization as LSC emitters. [12], [13] Effective usage of these NCs in LSCs, however, requires a number of important properties including high PL (PL) quantum efficiency (QE), tunable solar absorption, and good photostability. [12], [99] Apart from these fundamental necessities for the phosphor material, it is essential to avoid the suffering of the captured photons in the waveguide from various scattering and reabsorption losses. [12], [13] Amid various loss mechanisms affecting the LSC performance, the most crucial limiting factor for the practical implementation of the LSCs is the losses due to reabsorption in the system. [12], [13], [100] To overcome this problem, different approaches offering the utilization of NCs have been recently proposed owing to their Stokes-shifted emission together with other required physical properties. [13], [100] Among the studied materials addressing this problem are colloidal NC heterostructures (e.g., CdSe/CdS core/shell, CdSe/CdSe dot-in-rod) [13], [101], [102], ternary I-III-VI_2 QDs (e.g., $CuInS_2$/ZnS, $CuInSe_xS_{2-x}$/ZnS) [97], [98] and doped semiconductor NCs (e.g., ZnSe:Mn, CdSe:Cu). [12], [100]

In the last decade, based on the widespread success of Cu-doped phosphors, a lot of effort has been put on the development of Cu-doped zero- (0D) and one-dimensional

(1D) colloidal semiconductor NCs [103]–[109], which have unique advantages including size- and composition-dependent tunable PL emission, almost zero self-absorption, and p-type conductivity. [110] These nanostructures, which can emit in the spectral range of visible to near-infrared (NIR), have been extensively studied to be applied in the fields of color conversion, optical amplifiers, biomarkers, lasers, and secure information displays. [103], [104], [111], [112] Recently, Gamelin and coworkers [12], [98] have shown that the Cu-doped CdSe and $CuInS_2$/CdS QDs studied under identical conditions have exhibited significantly higher performance as compared to other colloidal NC heterostructures. However, in literature CdSe QDs have been found to be difficult for doping and, therefore, have been less explored in terms of doping as compared to other wide-bandgap II-VI NCs including ZnSe, CdS, ZnS, and InAs. [104], [105], [113]–[117] In the last two decades, partial cation exchange [115] and cluster-seeded heat-up methods [103], [118], [119] have shown success for doping of Cu into CdSe QDs with PL QEs reaching to respectable values as high as ~40%. Thus, further increase in PL QE of these Stokes-shifted and tunable visible-NIR emitting Cu-doped CdSe NCs will help to pave the way for integrating them into practical LSCs. [109]

Recently, CQWs, also commonly referred to as nanoplatelets (NPLs), have attracted great interest owing to their strong 1D confinement. [23], [120] This new class of NCs have shown superior optical properties as compared to the QDs including narrow spontaneous emission spectra, suppressed inhomogeneous emission broadening, extremely large linear and nonlinear absorption cross-sections [121], [122], and giant oscillator strengths. [123], [124] Due to finite vertical thicknesses of these colloidal NPLs, they possess distinctly sharp step-like absorption features as shown in Figure 5.1. In this regard, ideal LSCs are targeted with fluorophores that feature very weak

absorption (e.g., Stokes-shifted plus step-like absorption) in the emission region. [56] Recently, the detrimental effect of reabsorption in doped QDs and CdSe/CdS heterostructures due to partial optical absorption/emission overlap has been observed to limit their applicability for large-scaled LSCs. [12] Thus, the step-like optical absorption feature of NPLs is potentially a key to superior LSCs, provided that their other required parameters are engineered for the realization of the ideal LSCs. To date, doping of Cu ions has not been shown in the category of 2D colloidal NPLs. The widespread success of Cu^{+} doping in 0D NCs motivates us to explore its potential and applicability in these optically superior and strongly confined 2D NPLs.

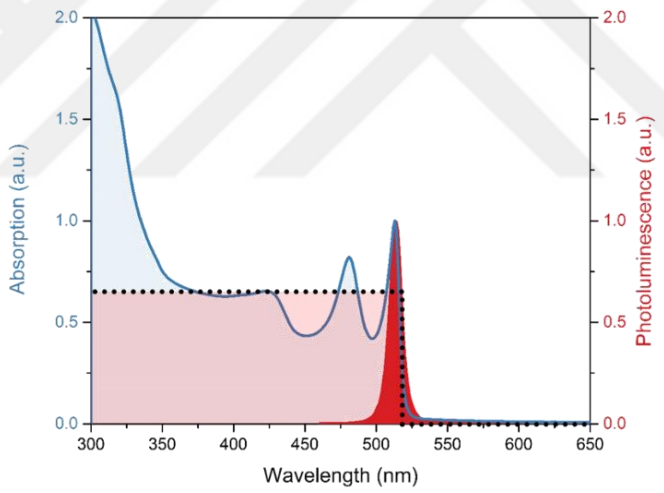

Figure 5.1 Absorption and PL spectra of 4 ML undoped CQW.

In this thesis, we propose and demonstrate Cu-doping in CdSe NPLs having an efficient dopant-induced PL emission synthesized using nucleation doping strategy. In addition to doping in different thicknesses, by the deposition of CdS shell on these doped NPLs, we also achieved tunable dopant-induced emission covering a wide range of electromagnetic spectrum from visible-to-NIR. Here detailed optical and morphological

studies have been systematically conducted to understand the effect of doping in varying amounts of Cu into the NPLs. The Cu-doping has been confirmed independently via different techniques including inductively coupled plasma mass spectroscopy (ICP-MS), high-angle annular dark-field (HAADF) scanning transmission electron microscopy (STEM) combined with energy-dispersive X-ray spectroscopy (EDS) mapping, and X-ray photoelectron spectroscopy (XPS). Furthermore, the dopant-induced PL emission in the Cu-doped CdSe NPLs has been corroborated with time-resolved fluorescence (TRF) spectroscopy. Using an 1D liquid waveguide setup [12], these Cu-doped NPLs possessing high absorption cross-section and near-unity PL QEs are shown to be the efficient materials for their deployment in practical LSCs.

5.2 Structural and Optical Characterization of Cu-doped Nanoplatelets

Herein, we used a hot injection-based nucleation doping method to successfully dope Cu^{+} ions in the CdSe NPLs having discrete vertical thicknesses (3 and 4 MLs). For the control samples having various thicknesses, existing optimized recipes were used for 3 and 4 ML CdSe NPLs syntheses. [120], [125] For effective doping of Cu (in terms of varied Cu concentration and the resulting dopant induced emission efficiency) in these thicknesses, the existing synthesis recipes were modified. Different types of Cu precursors and their time of injection during the synthesis have been optimized for having highly efficient and reproducible synthesis of the doped NPLs. The details of the synthesis can be found in ref. [126].

To investigate the Cu doping of the NPLs, HAADF STEM image of Cu-doped 3 ML CdSe NPLs (for the exemplary case of 1.1 atomic weight (at. wt.) % of Cu-doping) presented in Figure 5.2a, together with the EDS elemental map of Cd, Se and Cu given in Figure 5.2b,d clearly show the homogenous doping of Cu atoms within the core NPLs. Both Cd and Se maps are well matched with the HAADF-STEM image. At small doping levels, Cu maps also match the HAADF-STEM image.

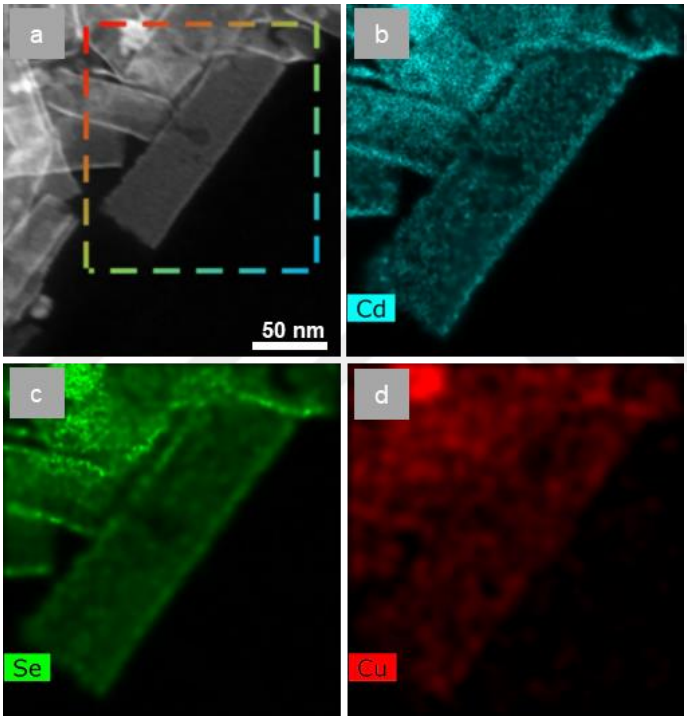

Figure 5.2 a) HAADF-STEM images of 1.1% of Cu-doped 3 ML CdSe NPLs. b-d) EDS maps of cadmium, selenium and copper. Reprinted with permission from [126]. Copyright 2017 WILEY-VCH Verlag GmbH & Co. KGaA, Weinheim.

To determine the exact doping amounts, ICP-MS measurements were carried out for the samples thoroughly cleaned with ethanol. Figure 5.3a,b show the change of the Cd, Se and Cu atomic percentages in the 3 and 4 ML doped NPLs as a function of the added

Cu precursor during the synthesis. From this set of analyses, we observed that there is a monotonic increase in the incorporated Cu dopant with the increase in Cu precursor up to a certain level. With the further increase in Cu precursor, the amount of Cu doping in the NPLs is found to decrease. Thus, the dopant concentration can be fine-controlled up to 11.3% for 3 ML and 9.0% for 4 ML NPLs by tuning the amount of Cu precursor solution used during synthesis.

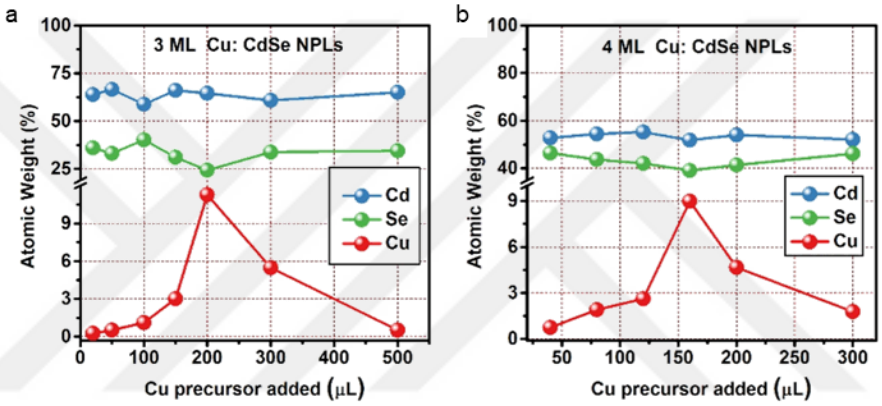

Figure 5.3 ICP:MS analysis of 3 (a) and 4 ML (b) Cu-doped NPLs having different Cu precursors used during synthesis. Reprinted with permission from [126]. Copyright 2017 WILEY-VCH Verlag GmbH & Co. KGaA, Weinheim.

Besides the EDS elemental maps and ICP measurements, XPS measurements independently show the presence of Cu in the NPLs, additionally providing further insight to understand its possible oxidation states. The high-resolution XPS spectra of 11.3% Cu-doped 3 ML CdSe NPLs shown in Figure 5.4 at 932.55 and 955.35 eV specific to Cu 2p orbitals suggesting the existence of Cu^{+} ions as the dopant. [105], [127], [128] High-resolution XPS spectra at the Cu 2p peak are presented in the inset of Figure 1g as a function of the increasing Cu-dopant amount.

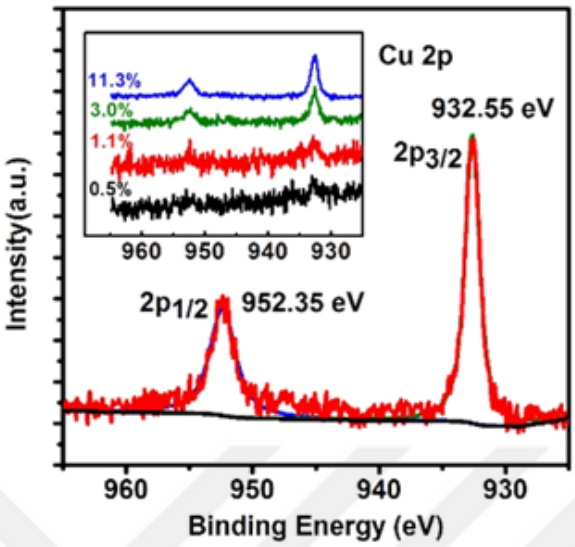

Figure 5.4 High-resolution XPS spectra of Cu 2p region in 3 ML Cu (11.3%) doped CdSe NPLs (inset: high-resolution spectra for different Cu concentrations in CdSe NPLs). Reprinted with permission from [126]. Copyright 2017 WILEY-VCH Verlag GmbH & Co. KGaA, Weinheim.

Figure 5.5a depicts the UV-visible absorption and steady-state PL spectroscopy results obtained from the samples of undoped and Cu-doped 3 and 4 ML CdSe NPLs. UV-visible absorption spectra of the undoped and doped samples show that both electron heavy-hole (e-hh) and electron light-hole (e-lh) transitions of the CdSe NPLs stay unchanged after doping, which pinpoints that the doping level studied here does not change the essential excitonic absorbance of the NPLs. [120] In addition, for all of the doped samples, there exists a very weak and broad absorption tail at lower energies beyond the first excitonic absorption peak. This may arise due to metal-to-ligand (conduction band) charge transfer ($ML_{CB}CT$) absorption state, which has been previously observed for the Cu-doped CdSe QDs. [129]–[131]

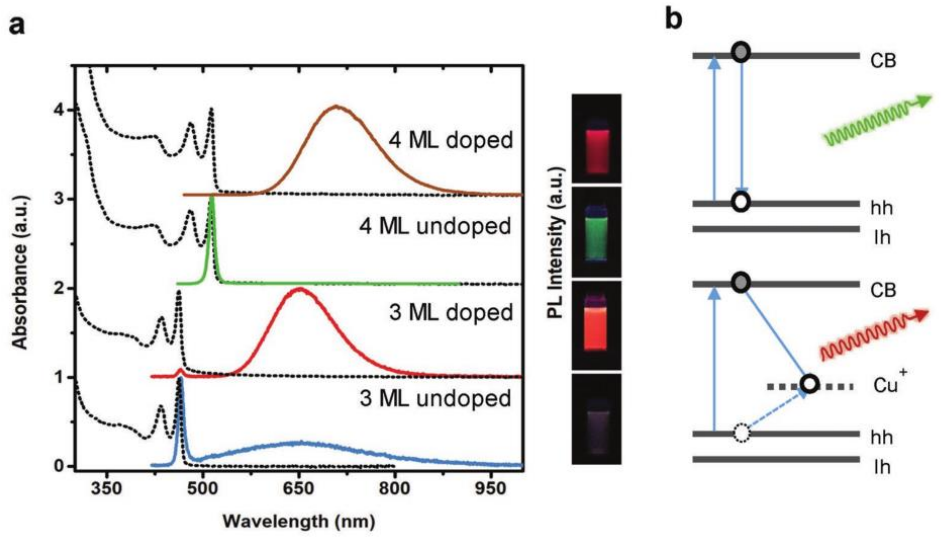

Figure 5.5 a) UV-visible absorption and PL spectra of 3 and 4 ML Cu-doped and undoped CdSe NPLs. Color pictures of the 3 ML and 4 ML undoped and Cu-doped CdSe NPLs illuminated by 365 nm UV lamp are shown next to the corresponding PL spectra. b) Energy band diagram for the undoped and Cu-doped NPLs. Herein, solid arrows show processes involving photons, and dashed arrows show nonradiative processes. Reprinted with permission from [126]. Copyright 2017 WILEY-VCH Verlag GmbH & Co. KGaA, Weinheim.

The PL emission spectrum of the undoped 3 ML CdSe NPLs in solution at room temperature (along with their normalized absorption spectrum) shown in Figure 5.5a exhibits a spectrally narrow band-edge (BE) emission peak at ~465 nm having a full-width at half-maximum (FWHM) of ~10 nm, which is a characteristic of the CdSe NPLs having 3 ML vertical thickness. [120] Along with the narrow BE emission, these NPLs also exhibit weak trap emission bands having a broad emission, which was reported earlier for these 3 ML NPLs. [23], [124] On the contrary, for the doped 3 ML NPLs, a strong and broad emission in the longer wavelength region (peaking at ~650 nm) was observed in addition to the weak BE emission at ~465 nm. This broad Stokes-shifted

emission was previously assigned to Cu-related emission ($ML_{CB}CT$) in CdSe QDs. [103], [130] UV-visible and PL emission spectra of undoped and Cu-doped 4 ML CdSe in Figure 5.5a show similar behavior with the doping of Cu ions, which has resulted in strong and efficient Stokes-shifted emission (~700 nm) for Cu-doped 4 ML NPLs. Thus, with the relaxation of the confinement from 3 ML to 4 ML NPLs, we found consistent behavior in the shift of Cu-related emission spectrum (650 to 700 nm). The real-color photographs of both the undoped and Cu-doped 3 ML and 4 ML CdSe NPLs illuminated under UV lamp are given next to the corresponding emission spectra. Figure 5.5b shows energy band diagram for the undoped and Cu-doped NPLs. Therefore, as seen from emission spectrum in Figure 5.5a and its corresponding band diagram in Figure 5.5b, the recombination mechanism for this Cu^+ related mid-gap emission in these doped NPLs is very similar to zero dimensional Cu-doped CdSe QDs [109], [129], [130], [132].

Furthermore, as shown in Figure 5.6, the Cu-related emission contributions in the total emission spectrum and absolute PL QE vary as a function of the increasing Cu precursors in the 3 and 4 ML doped NPLs. With increasing Cu precursor values up to certain levels (200 µL for 3 ML doped NPLs and 160 µL for 4 ML doped NPLs), the fraction of total integrated PL intensity associated with Cu^+ emission (I_{CT}/I_{TOT}) increases and the intensity of the excitonic PL decreases to nearly zero. Above these levels of dopant precursors, the integrated dopant related emission contributions decrease in consistency with the recovery of the BE emission. Additionally, as estimated by ICP:MS analysis, there is a monotonic increase in the doping percentage with respect to the added Cu precursors (e.g., up to 11.3% and 9.0% for 200 and 160 µL of the used precursors for 3 and 4 ML NPLs, respectively (Figure 5.3a,b)). Above these limits, further increasing amounts of the added Cu precursors during synthesis result in decreased doping

percentages in the synthesized NPLs. Recently, for Cu-doped CdSe QDs, a similar decrease in the Cu^+ doping amounts at higher added amounts of the precursors has been observed, which further leads to the recovery of BE emission in their studies. [133]

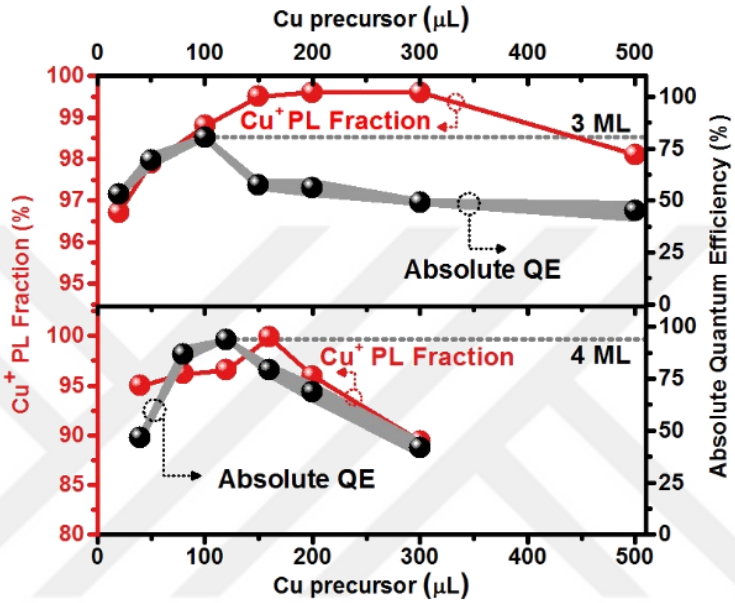

Figure 5.6 ICT/ITOT and absolute PL QE measured from the 3, 4 ML Cu-doped NPLs plotted vs. added Cu precursor values used in the reaction. Reprinted with permission from [126]. Copyright 2017 WILEY-VCH Verlag GmbH & Co. KGaA, Weinheim.

To this end, we measured the absolute PL QEs of all doped and undoped NPLs using an integrating sphere based on de Mello method (Figure 5.6). [55] Apart from the increase in dopant emission contributions (Cu^+ PL fraction), the absolute PL QE also increases with the increase of Cu feed up to 100 and 120 µL for 3 and 4 ML doped NPLs, respectively. At these dopant feed values, the highest achieved PL QEs are 80% and 97% for 3 and 4 ML doped CdSe NPLs, respectively. With further increase in the Cu feed values, although the integrated Cu^+ PL fraction increases slightly, the absolute PL QE

decreases. These high PL QEs (~80%-97%) for these Cu-doped 3 and 4 ML CdSe NPLs are found to be highly reproducible and stable at the ambient conditions for several months. Furthermore, these high PL QEs are nearly constant even at higher optical densities (from ~0.01 to 2.00 at the electron-heavy hole (e-hh) peak measured in 1 mm path length) of the dispersions thanks to their large Stokes shift. Recently, doped NCs (e.g., Cu-doped CdSe QDs) possessing Stokes-shifted emission have been shown to be the best in class luminophores for full spectrum LSCs, although they only reach the PL QE as high as 40%.[12] Thus, near-unity PL QE for our core only doped CdSe NPLs offers the potential to show significant improvement in the LSC applications.

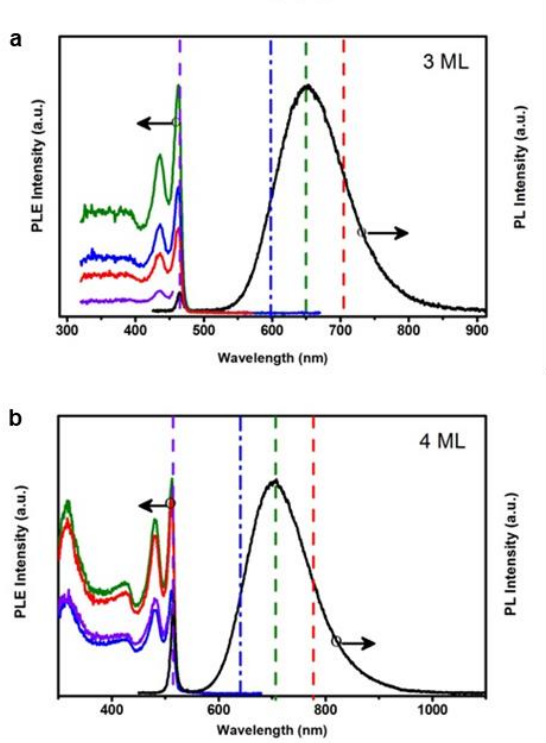

Figure 5.7 PLE spectra of Cu-doped 3 (a) and 4 (b) ML CdSe NPLs at different energies of Cu-related and excitonic emissions. Emission energies at which PLE spectrum is recorded has been shown by colored dotted lines for both 3 and 4 ML NPLs and their

corresponding PLE spectrum are shown in same color with solid lines. Reprinted with permission from [126]. Copyright 2017 WILEY-VCH Verlag GmbH & Co. KGaA, Weinheim.

To further understand the origin of this highly efficient and large Stokes-shifted emission in the doped NPLs, we performed PL excitation (PLE) spectroscopy (Figure 5.8a), collected while monitoring at the long-wavelength emission peak (650, 700 nm for 3 and 4 ML Cu-doped NPLs). These exhibit the midgap and both electron heavy-hole (e-hh) and electron light-hole (e-lh) transitions of the CdSe NPLs at the same relative intensity as in the electronic absorption spectrum (Figure 5.8a). Furthermore, excitation spectra of the Cu-doped 3 and 4 ML CdSe NPLs measured at spectral positions of the long-wavelength emission peak (i.e., at the peak, red-, and blue-tails), do not show any discernible spectral difference with respect to the electronic absorption spectrum (Figure 5.7). This suggests that there is no inhomogeneous broadening in the doped NPLs owing to their magic-sized vertical thicknesses. Thus, unlike colloidal QDs there is a near step-like optical absorption profile in these NPLs. Moreover, the PLE intensity for dopant related emission is much higher than BE-related emission for both 3 and 4 ML Cu-doped NPLs. Thus, it is clear from both the PL and PLE measurements that Cu doping has resulted in strong and efficient dopant-related Stokes-shifted emission in both 3 and 4 ML NPLs. Apart from the doping concentration, the type of NPL (thickness, lateral area), addition timing of the dopant precursor during synthesis, and different ligands used to prepare the dopant precursors are also important factors that are responsible for dominant and efficient Cu-related emission from NPLs.

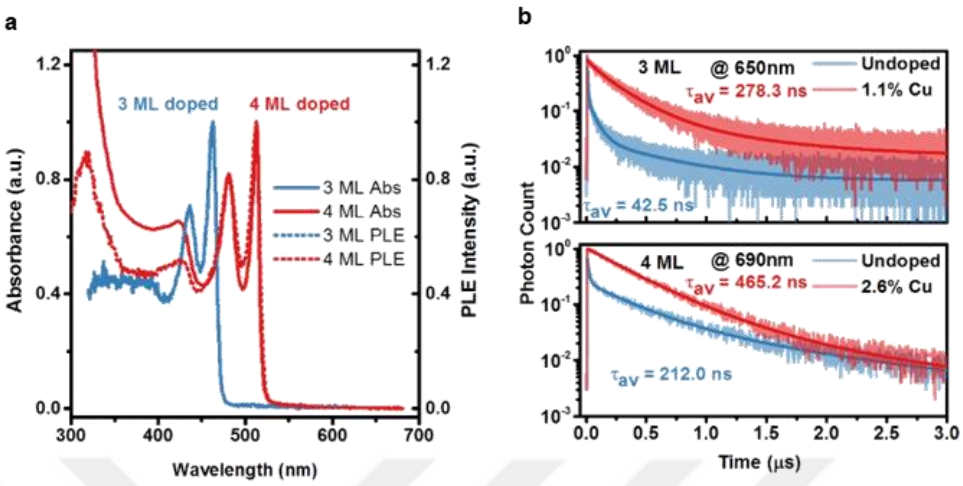

Figure 5.8 a) Electronic absorption (solid, blue and red), and PLE (dotted, blue and red, monitored at 650 and 700 nm for 3 and 4 ML NPLs, respectively) spectra of Cu-doped CdSe NPLs. b) TRF decays of the trap- and Cu-related emission at room temperature for undoped and Cu-doped 3 and 4 ML CdSe NPLs, respectively. Reprinted with permission from [126]. Copyright 2017 WILEY-VCH Verlag GmbH & Co. KGaA, Weinheim.

Furthermore, TRF spectroscopy using the time-correlated single-photon counting system was performed to understand this efficient dopant related emission in doped NPLs (Figure 5.8b). To investigate the exciton dynamics of this Stokes-shifted and highly efficient Cu^{+}-related emission in the doped NPLs, we compared the PL decay curves in the doped and undoped NPLs at the long wavelength (trap emission for the undoped NPL and Cu emission in the doped NPL). In the pure 3 ML undoped NPLs, a very broad but weak defect emission is observed. The fluorescence decay curve of this defect emission is shown in Figure 5.8b (upper panel), where we also compared this decay to the decay of the dopant emission in the doped NPLs. There is a stark contrast between the decay curves, which implies that this large Stokes-shifted emission in the doped NPLs is not due to the surface trap states. This supports that this emission

originates from the recombination of excited states between the conduction band of the CdSe NPL and the localized hole state of the Cu^+ dopant. [129] Similar observations for the trap and Cu-related PL emission are also made for 4 ML doped and undoped CdSe NPLs (Figure 5.8b, lower panel). Cu-doped CdSe QDs were previously shown to have an average lifetime between 300-500 ns. [109] The decay curves for both dopant and trap related emissions were fitted well with three exponentials for 3 ML and two exponentials for 4 ML doped NPLs. The average lifetime for Cu^+ and trap-related emissions in 3 and 4 ML doped and undoped NPLs were calculated as 278.3, 42.5 ns and 465.2, 211.2 ns, respectively. Briefly, absence and less fractional contribution of fast decay component in 4 and 3 ML Cu-doped NPLs, respectively, and positive correlation of Cu-related lifetime component with absolute PL QEs explain the origin of high PL QE in these doped NPLs.

There have been several reports for the origin and photophysics of Cu-related emission in CdSe NCs. [103], [111], [130] Although emergence of dopant related emission in these newly synthesized CdSe NPLs appears to be similar to the QDs, further investigations were performed to understand its behavior. Moreover, unlike 4 ML undoped CdSe NPLs, 3 ML undoped NPLs possess a weak and broad trap-related emission, which can be confused with dopant related emission in these newly synthesized doped NPLs.

Even though we verified the presence of variable amount of Cu in these doped NPLs by different elemental techniques, the origin of this highly efficient and Stokes-shifted emission in these NPLs needs to be further investigated. To this end, we selected two different, 3 and 4 ML Cu-doped and undoped CdSe NPLs. Using these four NPLs

separately as seeds we grew 1 ML shell of CdS via colloidal atomic layer deposition (c-ALD) technique. [134] Figure 5.9 shows the absorption and PL emission of the Cu-doped and undoped, 3 and 4 ML core/shell NPLs, respectively. In both the cases for 3 and 4 ML Cu-doped CdSe NPLs, the deposition of 1 ML of CdS shell redshifts the dopant emission further towards NIR region, which results from the relaxation of the confinement in the system. On the other hand, in the case of undoped NPLs with the deposition of 1 ML CdS shell, only excitonic emission is shifted to red regions and is in well agreement with previously reported undoped core/shell NPLs. [134] Due to the effective passivation of surface-related trap states with the CdS shell, trap-related emission in undoped 3 ML CdSe NPLs is completely suppressed. Therefore, appearance of this dopant-related redshifted-emission in the case of Cu-doped 3 ML core-shell NPLs supports that this broad Stokes-shifted emission in doped NPLs has not been originated from the surface-related trap sites. Furthermore, all excitonic features are well preserved in the doped samples as compared to undoped NPLs after growing the shell. However, with the deposition of 1 ML of shell there is a significant decrease in the measured absolute PL QEs (e.g., 70% to 12% and 90% to 18% for 3 and 4 ML samples, respectively). Furthermore, with the deposition of CdS shell, the Cu-related emission contributions are observed to decrease with the consistent recovery of BE emissions for both 3 and 4 ML Cu-doped NPLs. Recently, near complete elimination of Cu dopant ions and its related emission has been observed for Cu-doped CdSe QDs after overcoating these doped QDs with CdS shell. [133] The authors have accounted this extraction of Cu ions to the ability of different amines to access NC surface, which are used in the shell growth procedures. In our case for doped NPLs, rigorous cleaning steps and use of oleylamine during the shell growth with c-ALD approach suggest similar

behavior for the extraction of Cu ions during shell growth. Overall, these initial results are supportive to show that these highly efficient and Stokes-shifted emissions in 3 and 4 ML doped NPLs are originated from the $ML_{CB}CT$ PL emission like the previously studied 0D Cu-doped CdSe QDs.

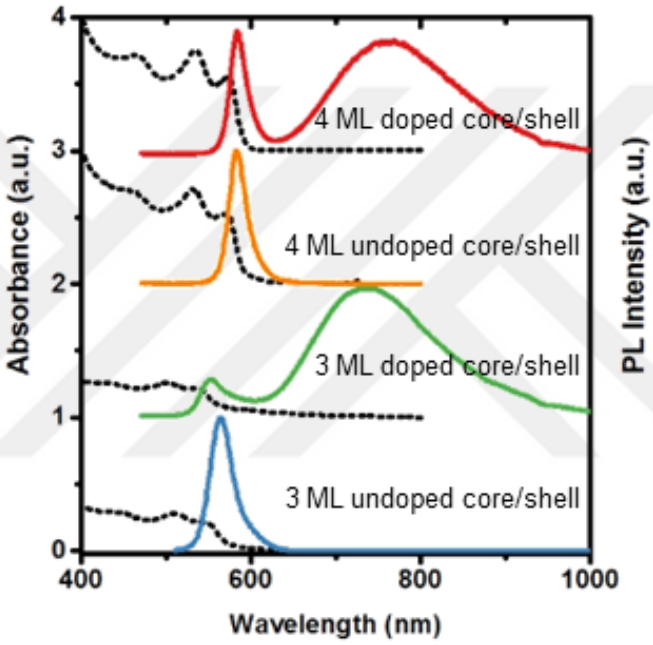

Figure 5.9 UV-visible absorption and PL spectra of undoped 3+1 (i.e., CdSe/CdS), doped 3+1 ML (i.e., CdSe:Cu/CdS), undoped 4+1 (i.e., CdSe/CdS), and doped 4+1 (i.e., CdSe:Cu/CdS) core-shell NPLs. Reprinted with permission from [126]. Copyright 2017 WILEY-VCH Verlag GmbH & Co. KGaA, Weinheim.

5.3 Reabsorption Characterization of Cu-doped Nanoplatelets

Successful Cu^+ doping leading to highly efficient dopant-related emission in our doped NPLs, creates a material platform as possible luminophores for LSC applications. The Cu-doped QDs have been recently shown to be the best phosphors for short- and long-scaled LSCs. [12] Although PL QE of these Cu^+ doped QDs has been shown to be moderately low (in the range of 40%) [12], [109] in comparison to other NC heterostructures [12], [13], their tunable solar absorption and lower reabsorption losses increased their performance as LSC luminophores. In our work, Cu^+ doping in 2D CdSe NCs has shown near-unity PL QE with similar Stokes-shifted emission. To characterize the performance of our doped 3 and 4 ML NPLs as LSC luminophores, we compared them with benchmarked Cu-doped CdSe QDs (having PL QE of 44%) in terms of reabsorption losses in the solution.

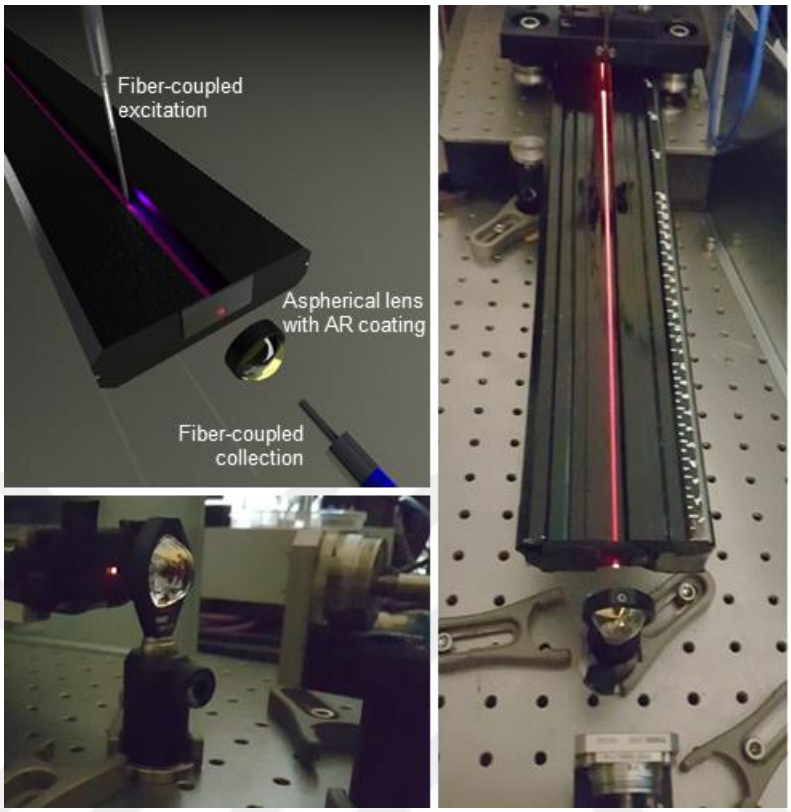

Figure 5.10 Illustration and photographs for 1D LSC measurement. Reprinted with permission from [126]. Copyright 2017 WILEY-VCH Verlag GmbH & Co. KGaA, Weinheim.

We measured the reabsorption losses in the NPLs using a recently reported 1D liquid waveguide with an excitation source placed on a movable stage [12] (Figure 5.10). The experimental setup is adapted with some modifications. The movable excitation source simulates the optical path distance to the stationary emission detection spectrometer coupled via a multimode optical fiber and a lens system. Reabsorption losses are quantified by measuring the PL spectra as a function of the optical path distance, L, up to 1.2 m. To make a fair comparison in terms of the reabsorption losses, we prepared 3 and 4 ML Cu^{+} doped NPL solutions having unity optical densities (OD=1) over t=1 mm (which is the thickness of the quartz cuvette) at their e-hh absorption peaks. The solutions

were carefully injected into the hollow fused silica waveguide without creating any air bubble in the optical path (since air bubbles can create unwanted artificial scattering centers). The PL emission spectra were collected by sliding the excitation source to systematically varied values of L, where L is the optical path distance between the excitation source and the collection end of the waveguide. Figure 5.11a,b show the PL spectra of 3 and 4 ML doped NPLs with changing L. The PL intensity decreases with a redshift in the spectrum with the increasing L for all luminophores. This decrease in the PL emission intensity and the accompanying redshift in the PL emission spectra of these highly-concentrated solutions of the doped NPLs are accounted for the reabsorption losses on the higher energy side of the PL emission spectrum. The normalized PL emission spectra for the doped 3 and 4 ML NPLs are shown in the insets of Figure 5.11a,b. The PL peak emission wavelength and half-maximum wavelength values of the measured PL spectra are given in Figure 5.13. While 3 and 4 ML NPLs exhibit a redshift, QDs show a narrowing in the PL emission spectra from the both sides causing the PL intensity to decrease significantly.

To understand the redshift and decrease in the PL spectrum, a numerical modeling using Beer-Lambert law is performed. For all samples, the change in the PL spectra with optical path distance obeys Beer-Lambert law perfectly, making the theoretical analysis possible on the LSC luminophores. In Figure 5.12, we compared the experimental and modeled PL spectra for all optical distances, which are in good agreement. Hence, using only the absorption and PL emission spectra of the emitters, it is possible to completely simulate the PL emission spectrum at any optical distance devising a useful method to characterize the performance of the luminophores to be used as LSC materials. Figure 5.14 shows the integrated PL emission intensities as a function of L for all of the

luminophores shown in Figure 5.12 (normalized at the collection end of the 1D waveguide, i.e., L=0). Unlike previously reported studies [12], [13], these integrated PL emission data were not corrected for any waveguide or scattering related losses. Although the scattering losses in the solutions are expected to be negligible due to the size of the luminophores, they have been already included in the absorbance spectra. Excellent agreement of the numerical model performed using Beer-Lambert law with experimental measurements also suggests that the only significant loss mechanism is the reabsorption loss in the solution.

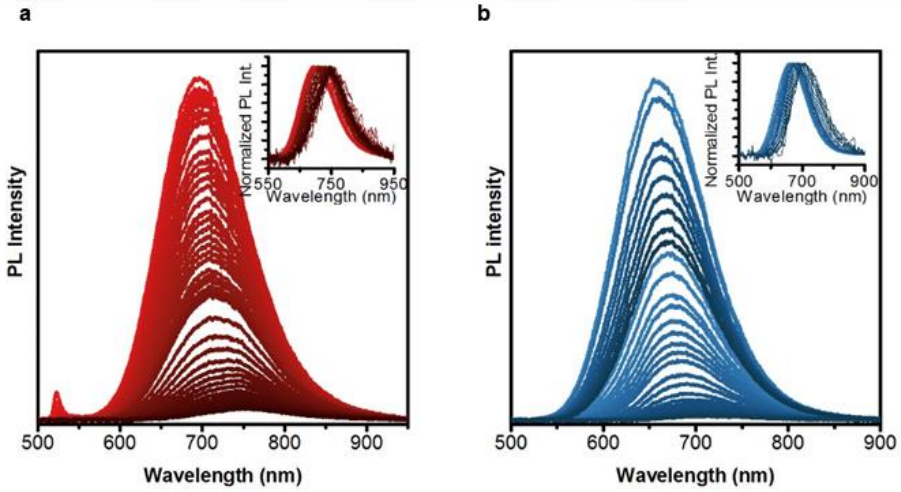

Figure 5.11 4 ML, (a) 3 ML (b) NPL PL intensities at different optical distances. Insets show the normalized PL emission of the same data to visualize redshift in the PL emission clearly. Reprinted with permission from [126]. Copyright 2017 WILEY-VCH Verlag GmbH & Co. KGaA, Weinheim.

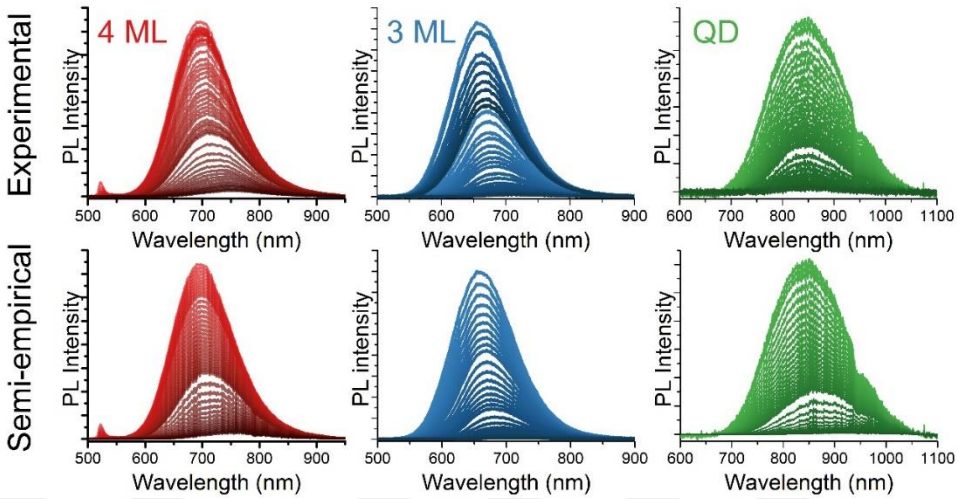

Figure 5.12 Experiment and semi-empirical calculation comparison. Reprinted with permission from [126]. Copyright 2017 WILEY-VCH Verlag GmbH & Co. KGaA, Weinheim.

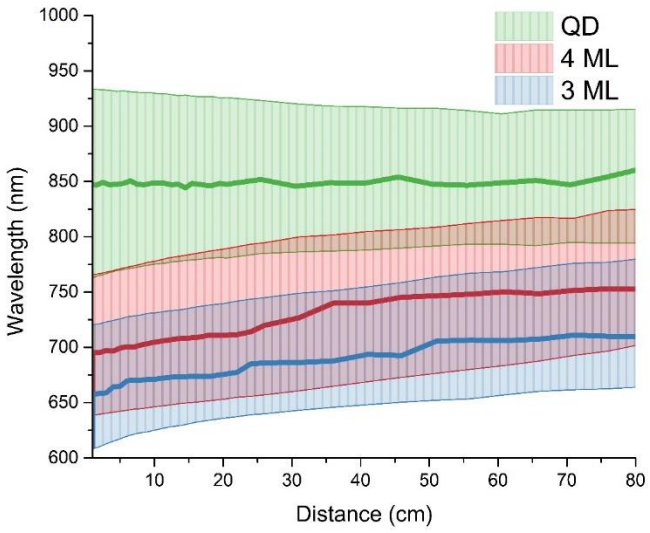

Figure 5.13 PL peak emission wavelength and half maximum wavelength values for different LSC emitters studied. Reprinted with permission from [126]. Copyright 2017 WILEY-VCH Verlag GmbH & Co. KGaA, Weinheim.

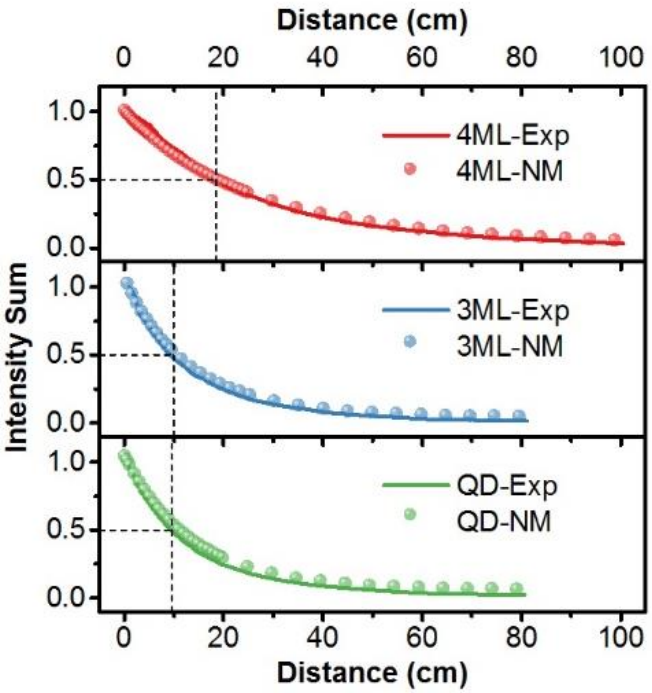

Figure 5.14 Spectrally integrated PL intensities for different luminophores as a function of excitation distance by both experimental and numerical modeling. The dashed lines indicate half-lengths, which for a given sample represent the value of length corresponding to 50% probability of reabsorption. Reprinted with permission from [126]. Copyright 2017 WILEY-VCH Verlag GmbH & Co. KGaA, Weinheim.

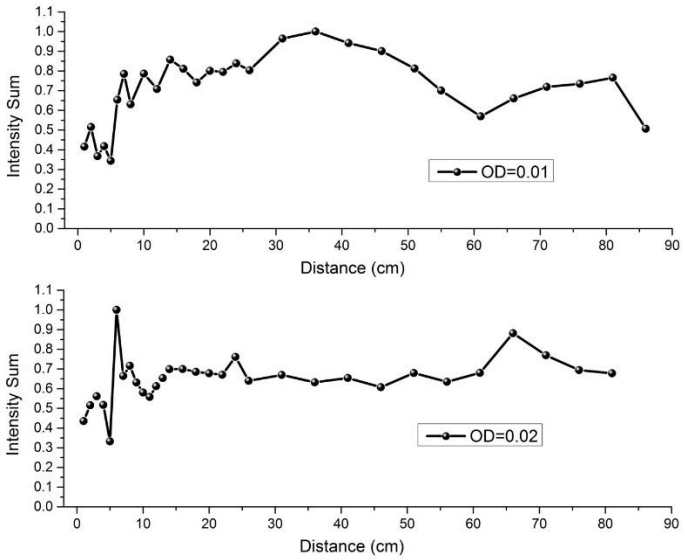

Figure 5.15 Dilute 4 ML doped NPLs to observe possible waveguide loss mechanisms other than reabsorption losses. Reprinted with permission from [126]. Copyright 2017 WILEY-VCH Verlag GmbH & Co. KGaA, Weinheim.

To reduce the effect of the reabsorption losses in the waveguide, we prepared dilute solutions of the 4 ML NPLs. 50 and 100 times diluted solutions of 4 ML doped NPLs do not show any noticeable PL emission intensity decrease that can be attributed to scattering or waveguide related losses in Figure 5.15. Agreement between experimentally measured and numerically modeled integrated PL emission intensities in Figure 5.14 indicates that at such high optical densities (OD=1) the dominating loss mechanism in the 1D waveguide stems from the reabsorption. In the numerical modeling, we used an effective confinement factor, Γ (<1), which quantifies how much of the emitted light is confined in the luminophore solution (i.e., the core region) of our waveguide. The best matching Γ factor is 0.3 for all luminophores in our setup. The LSC half length ($L_{1/2}$) values [135] calculated from Figure 5.14, for 3 ML and QDs are nearly similar (~10.0 cm), whereas 4 ML doped NPLs are shown to possess significantly longer

$L_{1/2}$ (~18.5 cm). In Figure 5.16a, we calculated the reabsorption probability to compare the LSC performances of the luminophores by considering their absorbance and PL emission profiles. [12] To simulate the PL emission decay with the increasing optical path, we used Beer-Lambert law. Our approach uses experimentally measured PL and absorbance values to predict PL spectrum at any optical distance. Although Beer-Lambert law does not consider the emission coming from the absorbing medium during the light propagation in the medium, the modified Beer-Lambert law for emissive materials does not apply for practical LSC applications. [136] Since the generated flux values (ϕ) are low considering the absorption cross-section (σ) and the average lifetime (τ), we have $2\sigma\tau\phi \ll 1$ and can thus ignore emission effect on the reabsorption characterization. We can safely use Beer-Lambert law instead of the modified equation. Since the light confined in the luminophore solution (i.e., the core region) will experience the reabsorption and the light confined in the fused silica pipe (i.e., the cladding region) will experience negligible absorption in our 1D LSC waveguide using the measured absorbance and the PL emission intensity at $\mathrm{L} = 0$ position of the luminophores, we calculate the intensity value in the waveguide at any L by:

$$I_{PL}(\lambda, \mathrm{L}) = I_{PL}(\lambda, 0)10^{-Abs(\lambda)\mathrm{L}\Gamma}$$

5.1

Here Γ is the effective confinement of the light in 1D waveguide. Experimental measurement and numerical modeling results are given in Figure 5.12. Using this method without performing any experiment, it is possible to predict LSC performance in terms of reabsorption losses. Reabsorption probability also provides a similar performance metric for the luminophores; 3 ML NPLs perform slightly better than the

benchmarked QDs and the performance of 4 ML NPLs substantially exceeds those of the other two. Reabsorption probability $R(l)$ calculations are done using normalized wavelength integrated PL intensity ($I_{PL-normalized}$) and is normalized absorbance at the e-hh peak (Abs) for all luminophores.

$$R(l) = \int_0^L I_{PL-normalized}(\lambda)\left(1 - 10^{Abs(\lambda)\times l}\right)\mathrm{d}\lambda \tag{5.2}$$

Here l is the reduced length defined as:

$$l = \frac{L \times OD}{t} \tag{5.3}$$

where L is the optical distance that light travelled, OD is the optical density at the absorption edge (at the e-hh peak for our case) and t is the thickness of the absorbing medium.

Ray-tracing Monte Carlo simulation using the absorbance and PL QE values of 4 ML NPLs predicts the half-length as ~19.5 cm, which is close to the experimentally measured 18.5 cm (Figure 5.16b). Ray-tracing calculation illustration is shown in Figure 5.17. To model the luminophore emission, we injected a beam inside the NC solution region with an angle θ_1 normal to the plane of incidence. Using Fresnel equations, we calculated the reflected and the transmitted intensities at each interface. Since the emission of the luminophores in the solution is expected to be isotopic and having random polarization, we averaged the intensities over the TE and TM polarizations. By

changing the angle θ_1 from 1° to 90° and averaging over all the angles, we obtained the total intensities of the light travelling inside the core (NC solution) and the cladding (fused silica) as shown in Figure 5.16b. In 2D modelling of our 1D waveguide we used lengths, refractive indices and absorbance values to exactly equivalent to the experimental conditions at the PL peak emission wavelength. Even at these high concentrations of the luminophores, the effect of the luminophores is negligible in the volume averaged effective refractive index calculation of the solutions. The refractive index of the luminophore solution can be taken as the refractive index of the solvent TCE, which is 1.477. Including the PL quantum yield of the 4 ML NPLs (PL QE = 0.92), we have successfully simulated the total intensity decay curve as shown in the Figure 5.16b.

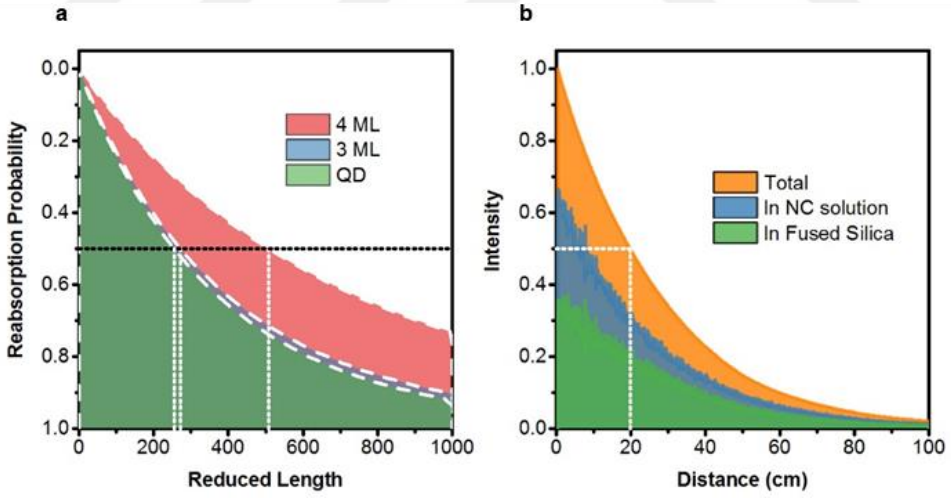

Figure 5.16 a**)** Reabsorption probability, plotted versus reduced length. b) Monte Carlo ray tracing simulation for the intensity decay using 4 ML NPL absorbance at the dopant emission and PL QE values. The dashed lines indicate half-lengths, which for a given sample represent the value of length corresponding to 50% probability of reabsorption.

Reprinted with permission from [126]. Copyright 2017 WILEY-VCH Verlag GmbH & Co. KGaA, Weinheim.

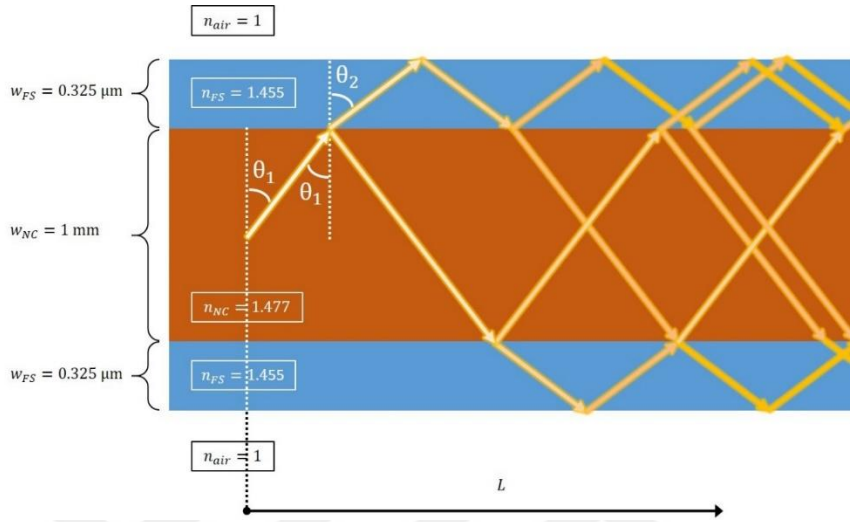

Figure 5.17 Ray-tracing Monte Carlo simulation for 4 ML NPLs. Reprinted with permission from [126]. Copyright 2017 WILEY-VCH Verlag GmbH & Co. KGaA, Weinheim.

5.4 Flux Gain Prediction of Cu-doped Nanoplatelets

In the light of experimental analyses and numerical model of the reabsorption losses, it is possible to project the flux gain (FG) performance of these doped NPLs. Previously, Gamelin and coworkers have reported the projected FG for 1D LSCs using the experimentally derived reabsorption data for different LSC emitters, e.g., doped NCs and different heterostructures. [12] 1D FG values were calculated as a function of the side length for large-area square LSC devices (with 1 mm vertical thickness and OD = 1). In this configuration silicon photovoltaic cells are attached to the two edges. Using

1D waveguide measurement data in Figure 5.11a,b and measured PL QEs of LSC luminophores, the projected 1D FGs are calculated using

$$FG = G_{geo}(L)\eta_{EC}\frac{\eta_{PV,PL}}{\eta_{PV,AM1.5}}\eta_{PL}\frac{A_{sol,NC}}{A_{sol,PV}}\int_0^L I_{PL}(l)dl \quad (5.4)$$

where $A_{sol,NC}$ and $A_{sol,PV}$ are the absorbed solar flux by NCs and Si PV, respectively, $G_{geo}(L)$ is the geometrical gain factor of our 1D hollow, fused silica pipe, η_{PL} is the NC PL QE, η_{EC} is the escape cone loss factor, $\eta_{PV,PL}$ and $\eta_{PV,AM1.5}$ is the overall efficiency of Si PV under PL emission wavelength and $AM_{1.5}$ irradiation, respectively. $I_{PL}(l)$ is the experimental distance-dependent waveguided PL intensity as reported in Figure 5.11. In their work, despite low PL QEs, Cu-doped CdSe QDs have shown the highest FGs for short- and long-range LSCs. In our case, 3 ML NPLs have a small spectral overlap with the solar spectrum; however, thanks to their higher PL QEs, 3 ML NPL FG performance is close to QDs (Figure 5.18). In addition to its low reabsorption loss performance, the absorption profile of 4 ML doped NPLs is redshifted with respect to 3 ML doped NPLs. This redshift in the absorption increases the overlap of the absorbance spectrum of the 4 ML NPLs with the solar emission. Having near-unity PL QE and increased spectral overlap with the solar spectrum compared to 3 ML NPLs, 4 ML NPLs significantly outperform QDs as expected from the integrated PL intensity measurements in Figure 5.14. Although the absorption profile of Cu-doped NPLs have limited spectral overlap with the solar emission in comparison to Cu-doped QDs, their near-unity PL QEs and step-like optical absorption have resulted in higher FGs for these newly synthesized LSC emitters.

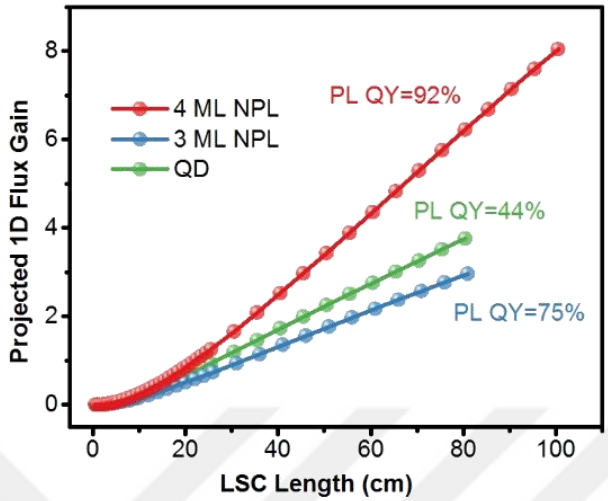

Figure 5.18 1D FGs for different LSC luminophores. Reprinted with permission from [126]. Copyright 2017 WILEY-VCH Verlag GmbH & Co. KGaA, Weinheim.

5.5 Fabrication and Optical Characterization of Luminescent Solar Concentrators of Cu-doped Nanoplatelets

After characterization of our luminophores in solution form, LSC prototypes have been prepared by embedding our Cu-doped luminophores in polymer matrix as a proof-of-concept demonstration. Poly(lauryl methacrylate) (PLMA) has been used as the polymer host material since its long side chains prevent agglomeration of colloidal NCs and low optical absorption in the visible spectrum allows for the fabrication of high-quality QD- and CQW-polymer nanocomposites. [56], [97], [137] Cu-doped QD-PLMA (and CQW-PLMA) nanocomposite between two borofloat glasses separated by transparent acrylic tape was photo-polymerized with two 365 nm UV sources from the both sides for

uniform illumination. In the process of nanocomposite photo-polymerization, we used an earlier reported fabrication procedure with slight modifications [97], [137]. All the luminophores under study were centrifuged in toluene solutions and dispersed in small amounts of lauryl methacrylate (LMA) monomer using ultrasonication for 3 h. ethylene glycol dimethacrylate (EGDM) (LMA:EGDM 80:20% wt/wt), which acted as a cross linking agent and a radical photoinitiator (Diphenyl(2,4,6-Trimethylbenzoyl) Phosphin E Oxide; 0.5% wt/wt) were mixed separately by ultrasonication for 1 h. Thereafter, monomer–luminophore mixture was then added to a large volume of LMA together with a secondary monomer, EGDM plus photoinitator mixture in N_2 filled glove box. The mixture was left to stir for 4 h under dark. The mixture was then injected into a mold consisting of two glass slides separated by acrylic tapes having thickness of 1 mm. Immediately these filled molds were irradiated under UV lamp (365 nm) for 40 min to trigger radical polymerization. The completion of UV-curing and presence of left over UV initiator was examined by UV-visible absorption spectroscopy which is very critical step. Uncompleted curing the polymer composite causes cracks in the polymer with time.

After the polymerization step, these 2D LSC plates were used as such for the measurements. In Figure 5.19a, high quality fabrication of the samples with high transmissivity is presented. Demonstrations of different LSCs under ambient light and UV light conditions are also given in Figure 5.20. Illustration of the Cu-doped 3 ML incorporated 2D LSC under UV illumination shows that the emitted light is concentrated to the edges (Figure 5.19b). In Figure 5.21a, absorbance and PL emission spectra for 3 and 4 ML NPLs in solution and in PLMA are presented. For both the 3 and 4 ML NPLs, we observed that our luminophores remain unaffected in terms of their steady-state spectral behavior when incorporated in PLMA. Furthermore, the PL emission decay

dynamics were analyzed in toluene, lauryl methacrylate (LMA) monomer solution and PLMA polymer film for the 3 and 4 ML NPLs without a noticeable change with respect to the matrix conditions, which indicates successful incorporation of these doped NPLs in the polymer matrix (Figure 5.21b).

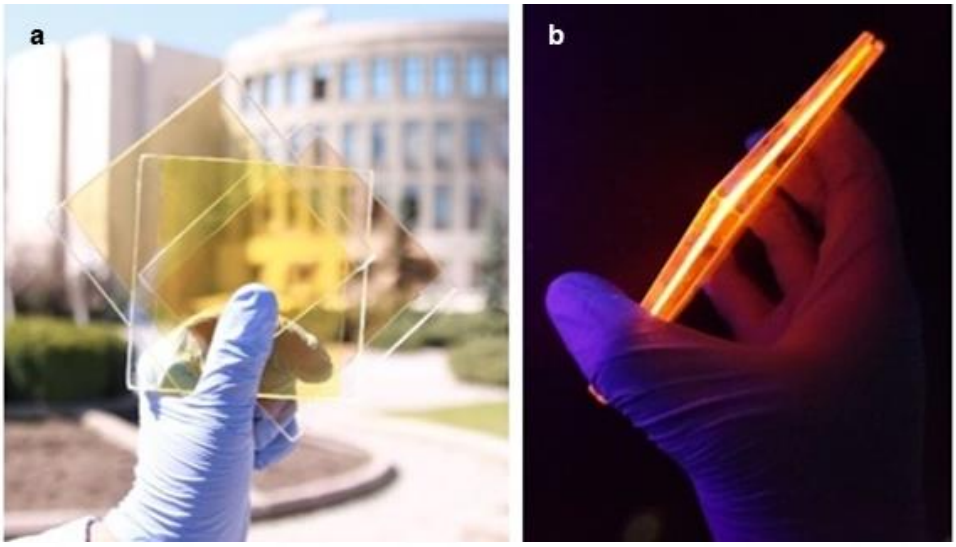

Figure 5.19 a) 2D LSCs consisting of Cu-doped 3 ML, 4 ML NPLs, and QDs incorporated in PLMA showing their high uniformity and high transmissivity under daylight. b) The real-color photograph of fabricated 3 ML NPL, 10 × 10 cm^2 LSC incorporated in PLMA matrix shown under UV illumination. Reprinted with permission from [126]. Copyright 2017 WILEY-VCH Verlag GmbH & Co. KGaA, Weinheim.

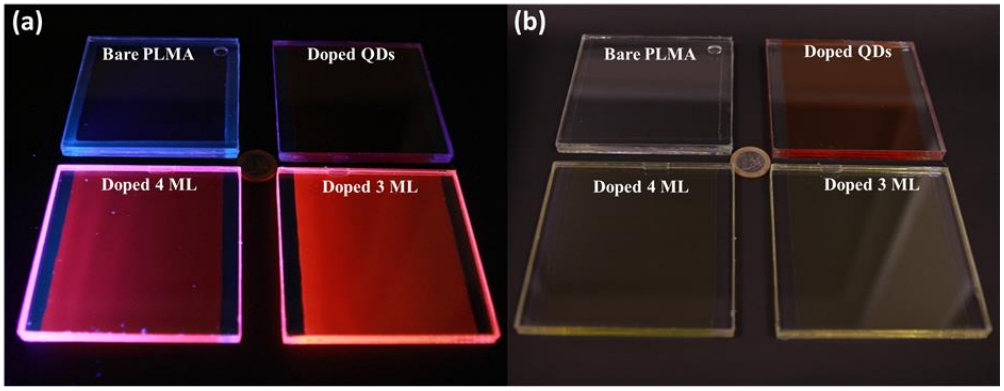

Figure 5.20 Photographs of different 10 × 10 cm^2 LSCs in PLMA matrix shown under (a) UV illumination and, (b) dim room light. Upper left (bare PLMA), upper right (Cu-doped CdSe QDs in PLMA), bottom left (Cu-doped 4 ML CdSe NPLs in PLMA), bottom right (Cu-doped 3 ML CdSe NPLs in PLMA). Reprinted with permission from [126]. Copyright 2017 WILEY-VCH Verlag GmbH & Co. KGaA, Weinheim.

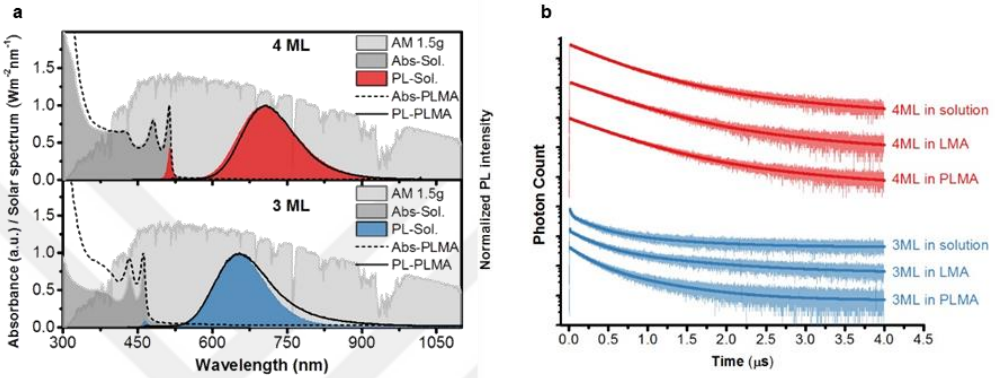

Figure 5.21 a) UV-vis absorption and PL spectra of Cu-doped 3 and 4 ML NPLs in toluene solution and in PLMA matrix. b) PL decay curves of 3 and 4 ML NPLs in toluene, LMA monomer solution and in PLMA solid films. Reprinted with permission from [126]. Copyright 2017 WILEY-VCH Verlag GmbH & Co. KGaA, Weinheim.

5.6 Optical Efficiency Characterization of Fabricated Nanoplatelet Luminescent Solar Concentrators

Using small slabs of dimensions (1 × 1 cm^2), we measured optical efficiencies of all the studied doped luminophores by using a calibrated integrating sphere. [101] The highest measured optical efficiencies are 52.5%, 46.5% and 13.5% for the LSCs fabricated using Cu-doped 3 ML NPLs, 4 ML NPLs, and QDs, respectively. To make a fair performance evaluation of the luminophores, we used the absorbed photon flux (*A*), which is

calculated by the integration of the overlap product of the luminophore absorption and the solar flux. Since three of the luminophores are absorbing different portions of the solar spectrum, this definition can be a useful metric for assessing their performance. Moreover, considering the constant external QE response of the commercial silicon solar cells, effect of the PL emission wavelength of the luminophores on the efficiency of the solar cell should be negligible.[12] In Figure 5.22a, measured optical efficiencies (η_{opt}) for different loadings of NPLs in PLMA matrix with one loading of QD is shown when a Si solar cell is attached to one edge of the LSC. Measured short-circuit current, open-circuit voltage and filling factor values are given in Figure 5.23. In all the measurements, no back diffuser or reflector was located at the back of the waveguide in order to reproduce the situation of an actual PV window illuminated by the sun light. For a 10 × 10 cm^2 lateral area of the LSC, emitted light is confined to edges having an area of 10 × 0.1 cm^2. For the measurements, we used polycrystalline silicon solar cells covered with an aperture matching the size of the LSC edge. Using Agilent parameter analyzer, we measured I-V curve of the solar cell under different LSC illuminations. For solar illumination Newport solar simulator with 1.3 inch working diameter is increased with a lens to match to the size of 10 × 10 cm^2 LSCs. Although light intensity decreased, spectral behavior remained the same. Maximum power output obtained by LSC attached solar cell response is divided to maximum power output of aperture covered solar cell under direct illumination. Then optical efficiency is calculated as:

$$\eta_{opt} = \frac{P_{LSC}}{P_{SC} G} \tag{5.5}$$

where P_{LSC} and P_{SC} are the power outputs of LSC attached solar and aperture covered bare solar cell. G is the geometrical gain coefficient. 'A' value is calculated by the integration of the overlap product of the luminophore absorption and the solar flux AM1.5:

$$A = \int S_{AM1.5}(\lambda)\left(1 - 10^{-abs(\lambda)}\right)d\lambda. \quad 5.6$$

where $S_{AM1.5}(\lambda)$ is the solar flux and $abs(\lambda)$ is the absorbance of LSC plates. Thanks to their preserved PL QEs (~70.0%) in PLMA matrix, the 3 ML NPLs showed η_{opt} =1.65% at 1.59×10^{20} photons $m^{-2}s^{-1}$, while the QDs showed η_{opt} =1.52% at 2.32×10^{20} photons $m^{-2}s^{-1}$. Despite the lower spectral overlap of 3 ML NPLs with the solar irradiation, higher loadings of the 3 ML samples absorbing less solar flux can generate higher outputs of electrical power. 4 ML NPLs showed relatively poor performance as compared to 3 ML NPLs due to their significantly lowered PL QE value (~ 40.0%) in PLMA matrix compared to their in-solution PL QEs (~92.0%). In Figure 5.22b and Figure 5.22c, calculated flux gains for the *G*=25 and *G*=250 cases (where *G* is the geometrical gain coefficient computed as the ratio of the lateral acceptance area of the LSC to the total area that solar cells can be attached around the periphery) are showing promising results for our highest measured in-solution PL QEs of 4 ML NPLs, which can reach above *FG*=0.2 value for *G*=25 and above *FG*=7.5 for *G*=250. In the case of *G*=250, effect of the 4 ML NPL step-like absorption profile provides a very steep *FG* enhancement for low absorbed photon flux values and after a certain *A* value, FG decreases very rapidly.

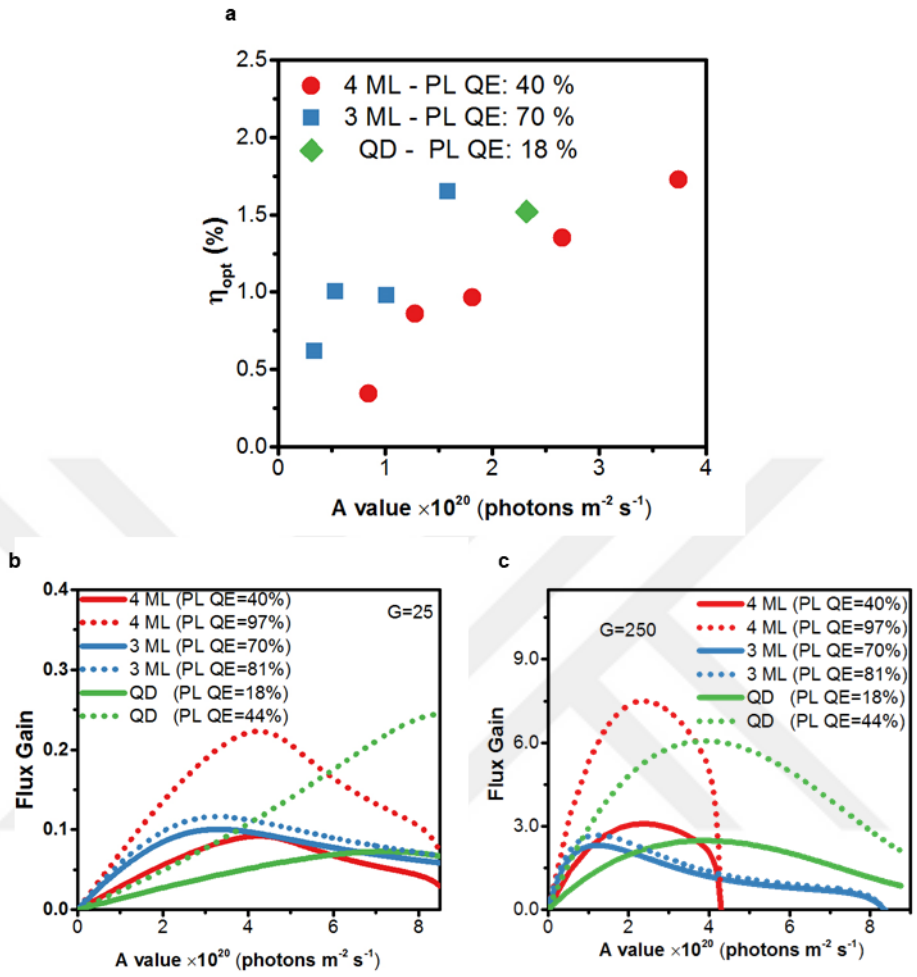

Figure 5.22 a) Measured optical efficiencies at different *A* values of the 3 ML and 4 ML samples and one concentration for the QD sample. Inset shows measured quantum efficiency of final devices using integrating sphere. b) Calculated flux gain values for *G*=25 case with the measured PL QEs in the PLMA polymer matrix and with in-solution PL QEs for determining upper performance limit. c) Similar calculated flux gain values for LSCs having *G*=250. Reprinted with permission from [126]. Copyright 2017 WILEY-VCH Verlag GmbH & Co. KGaA, Weinheim.

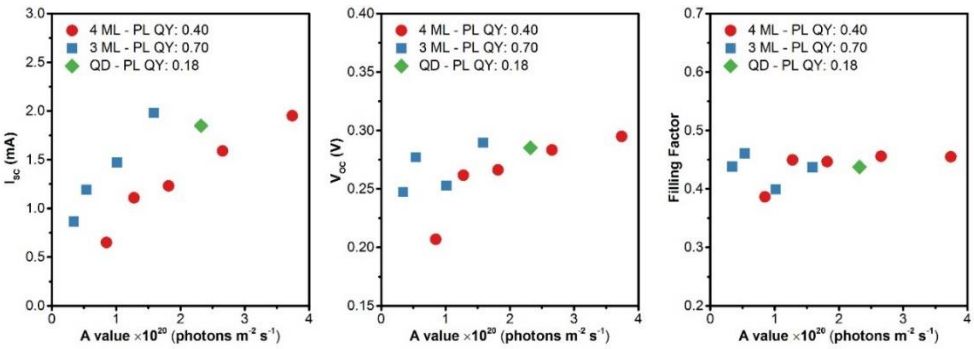

Figure 5.23 Measured short-circuit current (a), open-circuit voltage (b), and filling factor value (c) for the studied LSCs. Inset shows measured absolute quantum efficiency of final device using integrating sphere. Reprinted with permission from [126]. Copyright 2017 WILEY-VCH Verlag GmbH & Co. KGaA, Weinheim.

These results clearly show the great potential of these doped NPLs to be used in large-scale LSC applications. However, in order to obtain performance better than that of 3 ML doped NPLs, further optimization of process parameters of 4 ML Cu-doped NPLs is required to retain high PL QE in PLMA matrix. Recently, coating of colloidal QDs on glass slides using doctor blade technique has been shown to achieve high PL QE in 2D LSCs. [96] Thus, these newly shown Cu-doped NPLs possessing superior optical properties have the potential to be engineered with further optimization of fabrication procedures for retaining high PL QEs in the film form. Moreover, by extending this doping strategy in these 2D CQWs having slightly higher thickness (e.g., Cu-doped 5-11 ML CdSe, CdSe/CdS core-shell and core-crown architectures), the absorption spectrum can be further tuned to absorb more solar light and emit in the NIR. Therefore, the present work provides a solid platform for applying doping concepts in 2D colloidal quantum wells, which can be extended into different dopant/core and new 2D architectures for future solar light harvesting applications.

5.7 Summary

In conclusion, we have shown the first core doping of 2D CdSe colloidal quantum wells with Cu enabling exceptional optical properties including step-like optical absorption, tunable emission in the visible-to-NIR spectral region, large Stokes shift, near-unity PL QE and high absorption cross-section. Detailed HAADF-EDS, ICP, XPS, steady-state and time-resolved fluorescence spectroscopy studies confirm the copper doping in CdSe CQWs. The combination of stable and dominant dopant related emission having minimum self-absorption accompanied with significantly unchanged PL QE at higher optical densities augment the novelty and advantage of deep substitutional doping of Cu^{+} in CdSe CQWs. Under similar experimental and numerical conditions, these doped CQWs are shown to be excellent LSC emitters; outperforming typical doped QDs. Based on these unique properties, a prototype of LSC has been demonstrated. We believe that doping in CQWs can be extended to different types and thicknesses of materials, and different transition metal elements, which could expand potential applications in various optoelectronic and color conversion devices.

Chapter 6

Conclusions and Future Outlook

6.1 General Conclusions

In this thesis, we proposed and demonstrated innovative photon management techniques for photonic applications of colloidal semiconductor nanocrystals focusing on polarized color conversion and solar light concentration. To achieve polarized color conversion by using isotropic colloidal quantum dots, we studied the plasmonic interaction mechanisms that can modify the density of optical states. Strong dipole orientation dependence of surface plasmon coupled emission is utilized the in v-shaped grooves defined into the v-BLU structure. Forward scattering of Fano resonance effectively allowed for polarized light generation that can freely radiate into the farfield. Unlike many reports in the literature, our experimentally realized high contrast ratio of 9.70 for red quantum dots is measured at the farfield with a home-made measurement setup similar to LCD operation. This polarization response is a result of the linear polarization cancellation of the plasmonic surface. To analyze the origin of this polarization response, we investigated the emission kinetics of quantum dots using time resolved fluorescence measurements. Here the observed faster decay rate in the resonating polarization state

with higher emission intensity is a direct evidence of the strong modification in density of optical states as a part of Purcell enhancement. In addition, the oriented dipoles of coupled quantum dots to this v-BLU surface is observed using back focal plane imaging. The quantum dots coupled to v-BLU show a distinct back focal plane pattern, which is only reported for strong dipolar emissions observed in single molecule measurements. In contrast, the unpatterned films of isotropic quantum dots on fused silica and plain gold film show no sign of dipolar emission pattern in their back focal plane images. In the light of measurements unveiling the physics behind the polarized emission mechanism, we finally demonstrated a proof-of-concept display under v-BLU backillumination. Our fabrication includes a special mold and template stripping steps making the developed v-BLU structure commercially appealing. Also changing the plasmonic layer to silver in the v-BLU instead of gold enhances the spectral range of the v-BLU structure from the red to the green.

Also, in this thesis, efficient solar light concentration is successfully demonstrated using copper-doped colloidal nanoplatelets. Here, we exploited for the first time their inherent step-like absorption profile and large absorption cross-section of NPLs thanks to their atomically-flat two-dimensional structures. Using copper doping, we created a large Stokes shift in the emission spectra of NPLs to eliminate reabsorption losses observed in undoped NPLs, which prohibits their practical use in LSCs. We characterized light concentration performance of doped NPLs in terms of reabsorption losses experimentally and according to the developed models, we predicted flux gain performance of these emitters when incorporated in LSC panels. Our fabricated LSCs showed that copper-doped NPL LSCs outperform the undoped NPLs and benchmarked copper-doped quantum dots in terms of flux gain performance. Near-unity PL QE, large

Stokes shift, increased overlap with silicon photovoltaic peak efficiency curve of emission and large absorption cross-section make copper-doped NPLs a promising class of materials for the LSC applications.

In conclusion, we demonstrated effective photon management techniques for utilization of colloidal semiconductor nanocrystals in next-generation photonic applications. Conventional device designs cannot achieve the full potential of semiconductor nanocrystals that possess novel electronic and optical properties. Characterization and analysis techniques of this thesis are instrumental to exploit the unique properties of nanocrystals. Results presented in this thesis such as modification of optical density of states and artificially induced Stokes shift in the emission are important examples for the overall potential that colloidal semiconductor nanocrystals can offer. We believe that innovative methods in the device utilization of semiconductor nanocrystals will lead to efficient, cost-effective and high-performance photonic devices in the near future.

6.2 Outlook

Despite the significant achievements of colloidal semiconductor nanocrystals, many challenges are required to be overcome. Also, there is still room for improvement for the polarized color conversion and luminescent solar concentration applications. Here, the presented v-BLU unit is a practical application of density of optical states for linearly polarized light generation. However, metallic gold and silver layers in the designed v-BLU structures introduce an unavoidable loss to the system. Highly-doped semiconductors or next-generation low-loss plasmonic materials can overcome these losses. Also, while the color conversion in optically pumped semiconductor nanocrystals

showed substantial commercial success, electrical pumping nanocrystals holds a great promise for electronic display market. Many research groups work on the development of highly-efficient electrically-driven light-emitting diode architectures using semiconductor nanocrystals as an active medium. Considering these research efforts, it is not difficult to foresee commercialization of electrically driven light-emitting applications of semiconductor nanocrystals in the future. In this respect, v-BLU idea can be utilized in electrically-driven applications since continuous metallic layer v-BLU can serve as one of the electrical contacts. In this way, it could be possible to generate polarized light emission under electrical excitation, which could potentially boost the overall efficiency of the displays.

At the dawn of commercialization, innovative optical designs and novel materials can increase the optical efficiency of luminescent solar concentrators. Although we presented impressive efficiency values for the copper-doped NPLs thanks to their superior optical properties, two-dimensional semiconductor nanocrystals could offer high performance for LSCs. Shell coating over the doped core NPLs redshifts the copper state emission and absorption spectra of NPLs. This redshift in absorption and emission spectra increases the absorbed solar flux and photovoltaic cell peak efficiency overlap with the copper state emission, which would lead to an overall increase in the LSC efficiency. Also, utilization of Type II band alignment provides a large Stokes shift and high quantum efficiency, which are instrumental for a good LSC material. In this respect, Type II NPLs can be utilized in the LSCs. Finally, heavy-metal content of our highly-efficient nanoplatelets is another concern for commercialization of LSCs. Cd-free quantum dots having near-infrared emission hold a great promise for LSCs, however,

the development of heavy-metal free two-dimensional nanocrystals can make ultimate LSC materials.

6.3 Contributions of This Thesis to the Literature

Publications:

1. M. Sharma*, **K. Gungor***, A. Yeltik, M. Olutas, B. Guzelturk, Y. Kelestemur, T. Erdem, S. Delikanli, J. R. McBride, and H. V. Demir, "Near-Unity Emitting Copper-Doped Colloidal Semiconductor Quantum Wells for Luminescent Solar Concentrators," Adv. Mater., vol. 29, no. 30, p. 1700821, Aug. 2017. (* equal contribution)

2. **K. Güngör**, E. Ünal, and H. V. Demir, "Nanoplasmonic surfaces enabling strong surface-normal electric field enhancement," Opt. Express, vol. 21, no. 20, p. 23097, Oct. 2013.

3. L. V. Besteiro, **K. Gungor**, H. V. Demir, and A. O. Govorov, "Simple and Complex Metafluids and Metastructures with Sharp Spectral Features in a Broad Extinction Spectrum: Particle–Particle Interactions and Testing the Limits of the Beer–Lambert Law," J. Phys. Chem. C, vol. 121, no. 5, pp. 2987–2997, Feb. 2017.

4. S. Akhavan, **K. Gungor**, E. Mutlugun, and H. V. Demir, "Plasmonic light-sensitive skins of nanocrystal monolayers," Nanotechnology, vol. 24, no. 15, p. 155201, Apr. 2013.

5. B. Guzelturk, Y. Kelestemur, **K. Gungor**, A. Yeltik, M. Z. Akgul, Y. Wang, R. Chen, C. Dang, H. Sun, and H. V. Demir, "Stable and Low-Threshold Optical Gain in CdSe/CdS Quantum Dots: An All-Colloidal Frequency Up-Converted Laser," Adv. Mater., vol. 27, no. 17, pp. 2741–2746, May 2015.

6. Z. Soran-Erdem, T. Erdem, **K. Gungor**, J. Pennakalathil, D. Tuncel, and H. V. Demir, "High-Stability, High-Efficiency Organic Monoliths Made of Oligomer

Nanoparticles Wrapped in Organic Matrix," ACS Nano, vol. 10, no. 5, pp. 5333–5339, May 2016.

7. Y. Kelestemur, D. Dede, **K. Gungor**, C. F. Usanmaz, O. Erdem, and H. V. Demir, "Alloyed Heterostructures of $CdSe_xS_{1-x}$ Nanoplatelets with Highly Tunable Optical Gain Performance," Chem. Mater., vol. 29, no. 11, pp. 4857–4865, Jun. 2017.

8. S. Akhavan, C. Uran, B. Bozok, **K. Gungor**, Y. Kelestemur, V. Lesnyak, N. Gaponik, A. Eychmüller, and H. V. Demir, "Flexible and fragmentable tandem photosensitive nanocrystal skins," Nanoscale, vol. 8, no. 8, pp. 4495–4503, 2016.

9. M. Olutas, B. Guzelturk, Y. Kelestemur, **K. Gungor**, and H. V. Demir, "Highly Efficient Nonradiative Energy Transfer from Colloidal Semiconductor Quantum Dots to Wells for Sensitive Noncontact Temperature Probing," Adv. Funct. Mater., vol. 26, no. 17, pp. 2891–2899, May 2016.

10. Y. Kelestemur, B. Guzelturk, O. Erdem, M. Olutas, **K. Gungor**, and H. V. Demir, "Platelet-in-Box Colloidal Quantum Wells: CdSe/CdS@CdS Core/Crown@Shell Heteronanoplatelets," Adv. Funct. Mater., vol. 26, no. 21, pp. 3570–3579, Jun. 2016.

11. B. Liu, S. Delikanli, Y. Gao, D. Dede, **K. Gungor**, and H. V. Demir, "Nanocrystal light-emitting diodes based on type II nanoplatelets," Nano Energy, vol. 47, no. January, pp. 115–122, May 2018.

12. Y. Kelestemur, B. Guzelturk, O. Erdem, M. Olutas, T. Erdem, C. F. Usanmaz, **K. Gungor**, and H. V. Demir, "$CdSe/CdSe_{1-x}Te_x$ Core/Crown Heteronanoplatelets: Tuning the Excitonic Properties without Changing the Thickness," J. Phys. Chem. C, vol. 121, no. 8, pp. 4650–4658, Mar. 2017.

13. M. Sharma, M. Olutas, A. Yeltik, Y. Kelestemur, A. Sharma, S. Delikanli, B. Guzelturk, **K. Gungor**, J. R. McBride, and H. V. Demir, "Understanding the Journey of Dopant Copper Ions in Atomically Flat Colloidal Nanocrystals of CdSe Nanoplatelets Using Partial Cation Exchange Reactions," Chem. Mater., vol. 30, no. 10, pp. 3265–3275, May 2018.

14. N. Taghipour, P. L. Hernandez Martinez, A. Ozden, M. Olutas, D. Dede, **K. Gungor**, O. Erdem, N. Kosku Perkgoz, and H. V. Demir, "Near-Unity Efficiency Energy Transfer from Colloidal Semiconductor Quantum Wells of CdSe/CdS Nanoplatelets to a Monolayer of MoS_2", ACS Nano, Article ASAP, DOI: 10.1021/acsnano.8b04119.

Patents:

1. **K. Gungor**, S. Jun, H. V. Demir, E. Jang, B. Guzelturk, C. Uran, T. Erdem, "Optical elements and electronic devices including the same", US Patent US9997664B2.
2. **K. Gungor**, S. Jun, H. V. Demir, E. Jang, B. Guzelturk, C. Uran, T. Erdem, "Optical elements and electronic devices including the same", EP Patent EP2977798A1.
3. **K. Gungor**, S. Jun, H. V. Demir, E. Jang, B. Guzelturk, C. Uran, T. Erdem, "Optical elements and electronic devices including the same", KR Patent KR20160012843A.
4. **K. Gungor**, B. Guzelturk, O. Erdem, S. Jun, E. Jang, H. V. Demir, "Photoluminescent polarizers and electronic devices including the same", US20180188609A1, EP and KR Patent App.

Bibliography

[1] C. B. Murray, D. J. Norris, and M. G. Bawendi, "Synthesis and Characterization of Nearly Monodisperse CdE (E = S, Se, Te) Semiconductor Nanocrystallites," *J. Am. Chem. Soc.*, vol. 115, no. 19, pp. 8706–8715, 1993.

[2] Y. Kelestemur, M. Olutas, S. Delikanli, B. Guzelturk, M. Z. Akgul, and H. V. Demir, "Type-II colloidal quantum wells: CdSe/CdTe core/crown heteronanoplatelets," *J. Phys. Chem. C*, vol. 119, no. 4, pp. 2177–2185, 2015.

[3] M. A. Hines and P. Guyot-Sionnest, "Synthesis and characterization of strongly luminescing ZnS-capped CdSe nanocrystals," *J. Phys. Chem.*, vol. 100, no. 2, pp. 468–471, 1996.

[4] X. Peng, M. C. Schlamp, A. V. Kadavanich, and A. P. Alivisatos, "Epitaxial growth of highly luminescent CdSe/CdS core/shell nanocrystals with photostability and electronic accessibility," *J. Am. Chem. Soc.*, vol. 119, no. 30, pp. 7019–7029, 1997.

[5] Y. Kelestemur, B. Guzelturk, O. Erdem, M. Olutas, K. Gungor, and H. V. Demir, "Platelet-in-Box Colloidal Quantum Wells: CdSe/CdS@CdS Core/Crown@Shell Heteronanoplatelets," *Adv. Funct. Mater.*, vol. 26, no. 21, pp. 3570–3579, 2016.

[6] S. Kim, B. Fisher, H. J. Eisler, and M. Bawendi, "Type-II quantum dots: CdTe/CdSe(core/shell) and CdSe/ZnTe(core/shell) heterostructures," *J. Am. Chem. Soc.*, vol. 125, no. 38, pp. 11466–11467, 2003.

[7] H. Chen, J. He, and S.-T. Wu, "Recent Advances on Quantum-Dot-Enhanced Liquid Crystal Displays," *IEEE J. Sel. Top. Quantum Electron.*, vol. 23, no. 5, 2017.

[8] K. Bourzac, "Quantum dots go on display," *Nature*, vol. 493, no. 7432, p. 283, 2013.

[9] "Nanocrystals in their prime," *Nat. Nanotechnol.*, vol. 9, no. 5, p. 325, 2014.

[10] F. Meinardi, S. Ehrenberg, L. Dhamo, F. Carulli, M. Mauri, F. Bruni, R. Simonutti, U. Kortshagen, and S. Brovelli, "Highly efficient luminescent solar concentrators based on earth-abundant indirect-bandgap silicon quantum dots," *Nat. Photonics*, vol. 11, no. 3, pp. 177–185, Mar. 2017.

[11] A. Goetzberger and W. Greubel, "Applied Physics Solar Energy Conversion with Fluorescent Collectors," *Appl. Phys.*, vol. 14, pp. 123–139, 1977.

[12] L. R. Bradshaw, K. E. Knowles, S. McDowall, and D. R. Gamelin, "Nanocrystals for Luminescent Solar Concentrators," *Nano Lett.*, vol. 15, no. 2, pp. 1315–1323, Feb. 2015.

[13] F. Meinardi, A. Colombo, K. A. Velizhanin, R. Simonutti, M. Lorenzon, L. Beverina, R. Viswanatha, V. I. Klimov, and S. Brovelli, "Large-area luminescent solar concentrators based on `Stokes-shift-engineered' nanocrystals in amass-polymerized PMMA matrix," *Nat Phot.*, vol. 8, no. 5, pp. 1–8, 2014.

[14] M. R. Bergren, N. S. Makarov, K. Ramasamy, A. Jackson, R. Guglielmetti, and H. McDaniel, "High-Performance $CuInS_2$ Quantum Dot Laminated Glass Luminescent Solar Concentrators for Windows," *ACS Energy Lett.*, pp. 520–525, 2018.

[15] M. Fox, *Optical Properties of Solids*. New York, NY: Oxford University Press, 2001.

[16] S. L. Chuang, *Physics of Optoelectronic Devices*. New York, NY: John Wiley & Sons, Inc., 1995.

[17] A. I. Ekimov, A. L. Efros, and A. A. Onushchenko, "Quantum Size Effect in Semiconductor Mircrocrystals," *Solid State Commun.*, vol. 56, no. 11, pp. 921–924, 1985.

[18] G. Konstantatos, M. Badioli, L. Gaudreau, J. Osmond, M. Bernechea, F. P. G. de

Arquer, F. Gatti, and F. H. L. Koppens, “Hybrid graphene–quantum dot phototransistors with ultrahigh gain,” *Nat. Nanotechnol.*, vol. 7, no. 6, pp. 363–368, Jun. 2012.

[19] B. Ghosh and N. Shirahata, “Colloidal silicon quantum dots: synthesis and luminescence tuning from the near-UV to the near-IR range,” *Sci. Technol. Adv. Mater.*, vol. 15, no. 1, p. 014207, Feb. 2014.

[20] V. I. Klimov, “Optical Gain and Stimulated Emission in Nanocrystal Quantum Dots,” *Science*, vol. 290, no. 5490, pp. 314–317, Oct. 2000.

[21] D. V. Talapin, R. Koeppe, S. Götzinger, A. Kornowski, J. M. Lupton, A. L. Rogach, O. Benson, J. Feldmann, and H. Weller, “Highly Emissive Colloidal CdSe/CdS Heterostructures of Mixed Dimensionality,” *Nano Lett.*, vol. 3, no. 12, pp. 1677–1681, 2003.

[22] J. Hu, Li Ls, W. Yang, L. Manna, Wang Lw, and a P. Alivisatos, “Linearly polarized emission from colloidal semiconductor quantum rods.,” *Science*, vol. 292, no. 5524, pp. 2060–2063, 2001.

[23] S. Ithurria and B. Dubertret, “Quasi 2D colloidal CdSe platelets with thicknesses controlled at the atomic level,” *J. Am. Chem. Soc.*, vol. 130, no. 49, pp. 16504–16505, 2008.

[24] S. V Gaponenko, *Introduction to Nanophotonics*. Cambridge: Cambridge University Press, 2010.

[25] P. Harrison, *Quantum Wells, Wires and Dots*. Padstow: John Wiley & Sons Ltd, 2005.

[26] V. I. Klimov, S. A. Ivanov, J. Nanda, M. Achermann, I. Bezel, J. A. McGuire, and A. Piryatinski, “Single-exciton optical gain in semiconductor nanocrystals,” *Nature*, vol. 447, no. 7143, pp. 441–446, 2007.

[27] A. Klein, “Energy band alignment in chalcogenide thin film solar cells from

photoelectron spectroscopy," *J. Phys. Condens. Matter*, vol. 27, no. 13, p. 134201, Apr. 2015.

[28] D. Pines and D. Bohm, "A collective description of electron interactions: II. Collective vs individual particle aspects of the interactions," *Phys. Rev.*, vol. 85, no. 2, pp. 338–353, 1952.

[29] "The Lycurgus Cup." [Online]. Available: http://www.britishmuseum.org/explore/highlights/highlight_objects/pe_mla/t/the_lycurgus_cup.aspx.

[30] S. Maier, *Plasmonics: fundamentals and applications*. Springer, 2007.

[31] C. Powell and J. Swan, "Effect of oxidation on the characteristic loss spectra of aluminum and magnesium," *Phys. Rev.*, vol. 118, no. 3, pp. 640–643, 1960.

[32] G. P. Wiederrecht, *Handbook of Nanoscale Optics and Electronics*. Amsterdam: Elsevier B.V., 2010.

[33] G. Mie, "Contributions to the optics of turbid media, particularly of colloidal metal solutions," *Ann Phys*, vol. 25, pp. 377–442, 1908.

[34] C. F. Bohren and D. R. Huffman, *Absorption and scattering of light by small particles*. Wiley, 1983.

[35] L. V Besteiro, K. Gungor, H. V. Demir, and A. O. Govorov, "Simple and Complex Metafluids and Metastructures with Sharp Spectral Features in a Broad Extinction Spectrum: Particle–Particle Interactions and Testing the Limits of the Beer–Lambert Law," *J. Phys. Chem. C*, vol. 121, no. 5, pp. 2987–2997, Feb. 2017.

[36] P. N. Prasad, *Nanophotonics*. Hoboken: John Wiley & Sons, Inc., 2004.

[37] L. Novotny and B. Hecht, *Principles of nano-optics*. New York: Cambridge University Press, 2006.

[38] A. N. Oraevskii, “Spontaneous emission in a cavity,” *Uspekhi Fiz. Nauk*, vol. 164, no. 4, p. 415, 1994.

[39] P. P. Pompa, L. Martiradonna, a Della Torre, F. Della Sala, L. Manna, M. De Vittorio, F. Calabi, R. Cingolani, and R. Rinaldi, “Metal-enhanced fluorescence of colloidal nanocrystals with nanoscale control.,” *Nat. Nanotechnol.*, vol. 1, no. 2, pp. 126–30, Nov. 2006.

[40] E. Hwang, I. I. Smolyaninov, and C. C. Davis, “Surface plasmon polariton enhanced fluorescence from quantum dots on nanostructured metal surfaces.,” *Nano Lett.*, vol. 10, no. 3, pp. 813–20, Mar. 2010.

[41] J.-H. Song, T. Atay, S. Shi, H. Urabe, and A. V Nurmikko, “Large enhancement of fluorescence efficiency from CdSe/ZnS quantum dots induced by resonant coupling to spatially controlled surface plasmons.,” *Nano Lett.*, vol. 5, no. 8, pp. 1557–61, Aug. 2005.

[42] Y. Jiang, H.-Y. Wang, H. Wang, B.-R. Gao, Y. Hao, Y. Jin, Q.-D. Chen, and H.-B. Sun, “Surface Plasmon Enhanced Fluorescence of Dye Molecules on Metal Grating Films,” *J. Phys. Chem. C*, vol. 115, no. 25, pp. 12636–12642, Jun. 2011.

[43] T. B. Hoang, G. M. Akselrod, C. Argyropoulos, J. Huang, D. R. Smith, and M. H. Mikkelsen, “Ultrafast spontaneous emission source using plasmonic nanoantennas,” *Nat. Commun.*, vol. 6, pp. 1–7, 2015.

[44] D. V. Guzatov, S. V. Gaponenko, and H. V. Demir, “Plasmonic enhancement of electroluminescence,” *AIP Adv.*, vol. 8, no. 1, 2018.

[45] P. L. Stiles, J. a Dieringer, N. C. Shah, and R. P. Van Duyne, “Surface-enhanced Raman spectroscopy.,” *Annu. Rev. Anal. Chem. (Palo Alto. Calif).*, vol. 1, pp. 601–26, Jan. 2008.

[46] S. Dutta, M. Imran, P. Kumar, R. Pal, P. Datta, and R. Chatterjee, “Comparison of etch characteristics of KOH, TMAH and EDP for bulk micromachining of silicon (110),” *Microsyst. Technol.*, vol. 17, no. 10–11, pp. 1621–1628, Sep.

2011.

[47] "Anisotropic Silicon Etch Using KOH," *INRF application note, Process name: KOH01*, 2000. [Online]. Available: https://www.inrf.uci.edu/wordpress/wp-content/uploads/sop-wet-anisotropic-si-etch-using-koh.pdf.

[48] I. Zubel and M. Kramkowska, "The effect of isopropyl alcohol on etching rate and roughness of (100) Si surface etched in KOH and TMAH solutions," *Sensors Actuators A Phys.*, vol. 93, no. 2, pp. 138–147, Sep. 2001.

[49] K. P. Rola, K. Ptasiński, A. Zakrzewski, and I. Zubel, "Silicon 45° micromirrors fabricated by etching in alkaline solutions with organic additives," *Microsyst. Technol.*, vol. 20, no. 2, pp. 221–226, Jun. 2013.

[50] K. P. Rola and I. Zubel, "Triton Surfactant as an Additive to KOH Silicon Etchant," *J. Microelectromechanical Syst.*, vol. 22, no. 6, pp. 1373–1382, Dec. 2013.

[51] H. Seidel, L. Csepregi, A. Heuberger, and H. Baumgärtel, "Anisotropic Etching of Crystalline Silicon in Alkaline Solutions II: Influence of Dopants," *J. Electrochem. Soc.*, vol. 137, no. 11, pp. 3626–3632, 1990.

[52] M. D. Henry, "ICP Etching of Silicon for Micro and Nanoscale Devices," California Institute of Technology, 2010.

[53] A. S. Backer, M. P. Backlund, M. D. Lew, and W. E. Moerner, "Single-molecule orientation measurements with a quadrated pupil.," *Opt. Lett.*, vol. 38, no. 9, pp. 1521–3, 2013.

[54] Y. Gao, M. C. Weidman, and W. A. Tisdale, "CdSe Nanoplatelet Films with Controlled Orientation of their Transition Dipole Moment," *Nano Lett.*, vol. 17, no. 6, pp. 3837–3843, 2017.

[55] J. C. de Mello, H. F. Wittmannn, and R. H. Friend, "An Improved Experimental Determination of External Photoluminescence Quantum Efficiency," *Adv.*

Mater., vol. 9, no. 3, p. 230, 1997.

[56] J. M. Pietryga, Y. S. Park, J. Lim, A. F. Fidler, W. K. Bae, S. Brovelli, and V. I. Klimov, "Spectroscopic and device aspects of nanocrystal quantum dots," *Chem. Rev.*, vol. 116, no. 18, pp. 10513–10622, 2016.

[57] S. Kim and M. G. Bawendi, "Oligomeric Ligands for Luminescent and Stable Nanocrystal Quantum Dots," *J. Am. Chem. Soc.*, vol. 125, no. 48, pp. 14652–14653, 2003.

[58] B. G. Jeong, Y. S. Park, J. H. Chang, I. Cho, J. K. Kim, H. Kim, K. Char, J. Cho, V. I. Klimov, P. Park, D. C. Lee, and W. K. Bae, "Colloidal Spherical Quantum Wells with Near-Unity Photoluminescence Quantum Yield and Suppressed Blinking," *ACS Nano*, vol. 10, no. 10, pp. 9297–9305, 2016.

[59] E. Jang, S. Jun, H. Jang, J. Lim, B. Kim, and Y. Kim, "White-light-emitting diodes with quantum dot color converters for display backlights," *Adv. Mater.*, vol. 22, no. 28, pp. 3076–3080, 2010.

[60] V. Wood and V. Bulović, "Colloidal quantum dot light-emitting devices," *Nano Rev.*, vol. 1, no. 1, p. 5202, 2010.

[61] T. H. Kim, K. S. Cho, E. K. Lee, S. J. Lee, J. Chae, J. W. Kim, D. H. Kim, J. Y. Kwon, G. Amaratunga, S. Y. Lee, B. L. Choi, Y. Kuk, J. M. Kim, and K. Kim, "Full-colour quantum dot displays fabricated by transfer printing," *Nat. Photonics*, vol. 5, no. 3, pp. 176–182, 2011.

[62] Y. Wang, I. Fedin, H. Zhang, and D. V. Talapin, "Direct optical lithography of functional inorganic nanomaterials," *Science*, vol. 357, no. 6349, pp. 385–388, 2017.

[63] T. Erdem and H. V. Demir, "Semiconductor nanocrystals as rare-earth alternatives," *Nat. Photonics*, vol. 5, no. 3, pp. 126–126, Mar. 2011.

[64] T. Erdem, S. Nizamoglu, X. W. Sun, and H. V. Demir, "A photometric

investigation of ultra-efficient LEDs with high color rendering index and high luminous efficacy employing nanocrystal quantum dot luminophores.," *Opt. Express*, vol. 18, no. 1, pp. 340–7, Jan. 2010.

[65] S. Nizamoglu, T. Ozel, E. Sari, and H. V. Demir, "White light generation using CdSe/ZnS core-shell nanocrystals hybridized with InGaN/GaN light emitting diodes," *Nanotechnology*, vol. 18, no. 6, 2007.

[66] S. Nizamoglu, G. Zengin, and H. V. Demir, "Color-converting combinations of nanocrystal emitters for warm-white light generation with high color rendering index," *Appl. Phys. Lett.*, vol. 92, no. 3, 2008.

[67] B. T. Diroll, E. A. Gaulding, C. R. Kagan, and C. B. Murray, "Spectrally-Resolved Dielectric Functions of Solution-Cast Quantum Dot Thin Films," *Chem. Mater.*, vol. 27, no. 18, pp. 6463–6469, 2015.

[68] Z. Luo, J. Manders, and J. Yurek, "Television's Quantum dots will be the next darling of TV manufacturers," *IEEE Spectr.*, vol. 55, no. 3, pp. 28–35, Mar. 2018.

[69] J. Hu, L. Li, W. Yang, L. Manna, L.-W. Wang, and A. P. Alivisatos, "Linearly Polarized Emission from Colloidal Semiconductor Quantum Dots," *Science (80-.).*, vol. 292, no. 2001, pp. 2060–2063, 2001.

[70] R. A. M. Hikmet, P. T. K. Chin, D. V. Talapin, and H. Weller, "Polarized-light-emitting quantum-rod diodes," *Adv. Mater.*, vol. 17, no. 11, pp. 1436–1439, 2005.

[71] P. D. Cunningham, J. B. Souza, I. Fedin, C. She, B. Lee, and D. V. Talapin, "Assessment of Anisotropic Semiconductor Nanorod and Nanoplatelet Heterostructures with Polarized Emission for Liquid Crystal Display Technology," *ACS Nano*, vol. 10, no. 6, pp. 5769–5781, 2016.

[72] H. K. Fu, C. W. Chen, C. H. Wang, T. T. Chen, and Y. F. Chen, "Creating optical anisotropy of CdSe/ZnS quantum dots by coupling to surface plasmon polariton resonance of a metal grating.," *Opt. Express*, vol. 16, no. 9, pp. 6361–6367, 2008.

[73] M. Ma, D. S. Meyaard, Q. Shan, J. Cho, E. Fred Schubert, G. B. Kim, M. H. Kim, and C. Sone, “Polarized light emission from GaInN light-emitting diodes embedded with subwavelength aluminum wire-grid polarizers,” *Appl. Phys. Lett.*, vol. 101, no. 6, 2012.

[74] L. Zhang, J. H. Teng, S. J. Chua, and E. A. Fitzgerald, “Linearly polarized light emission from InGaN light emitting diode with subwavelength metallic nanograting,” *Appl. Phys. Lett.*, vol. 95, no. 26, pp. 2007–2010, 2009.

[75] R. Oulton, B. D. Jones, S. Lam, A. R. A. Chalcraft, D. Szymanski, D. O’Brien, T. F. Krauss, D. Sanvitto, A. M. Fox, D. M. Whittaker, M. Hopkinson, and M. S. Skolnick, “Polarized quantum dot emission from photonic crystal nanocavities studied under moderesonant enhanced excitation,” *Opt. Express*, vol. 15, no. 25, p. 17221, 2007.

[76] T. Ming, L. Zhao, H. Chen, K. C. Woo, J. Wang, and H. Q. Lin, “Experimental evidence of plasmophores: Plasmon-directed polarized emission from gold nanorod - Fluorophore hybrid nanostructures,” *Nano Lett.*, vol. 11, no. 6, pp. 2296–2303, 2011.

[77] M. Ren, M. Chen, W. Wu, L. Zhang, J. Liu, B. Pi, X. Zhang, Q. Li, S. Fan, and J. Xu, “Linearly polarized light emission from quantum dots with plasmonic nanoantenna arrays,” *Nano Lett.*, vol. 15, no. 5, pp. 2951–2957, 2015.

[78] E. De Leo, A. Cocina, P. Tiwari, L. V. Poulikakos, P. Marqués-Gallego, B. Le Feber, D. J. Norris, and F. Prins, “Polarization Multiplexing of Fluorescent Emission Using Multiresonant Plasmonic Antennas,” *ACS Nano*, vol. 11, no. 12, pp. 12167–12173, 2017.

[79] C. Uran, T. Erdem, B. Guzelturk, N. K. Perkgöz, S. Jun, E. Jang, and H. V. Demir, “Highly polarized light emission by isotropic quantum dots integrated with magnetically aligned segmented nanowires,” *Appl. Phys. Lett.*, vol. 105, no. 14, p. 141116, 2014.

[80] T. Ozel, S. Nizamoglu, M. A. Sefunc, O. Samarskaya, I. O. Ozel, E. Mutlugun,

V. Lesnyak, N. Gaponik, A. Eychmuller, S. V. Gaponenko, and H. V. Demir, “Anisotropic emission from multilayered plasmon resonator nanocomposites of isotropic semiconductor quantum dots,” *ACS Nano*, vol. 5, no. 2, pp. 1328–1334, 2011.

[81] J. R. Lakowicz, J. Malicka, I. Gryczynski, and Z. Gryczynski, “Directional surface plasmon-coupled emission: A new method for high sensitivity detection,” *Biochem. Biophys. Res. Commun.*, vol. 307, no. 3, pp. 435–439, 2003.

[82] I. Gryczynski, J. Malicka, W. Jiang, H. Fischer, W. C. W. Chan, Z. Gryczynski, W. Grudzinski, and J. R. Lakowicz, “Surface-plasmon-coupled emission of quantum dots.,” *J. Phys. Chem. B*, vol. 109, no. 3, pp. 1088–93, Jan. 2005.

[83] M. Hegner, P. Wagner, and G. Semenza, “Ultralarge atomically flat template-stripped Au surfaces for scanning probe microscopy,” *Surf. Sci.*, vol. 291, no. 1–2, pp. 39–46, 1993.

[84] D. Qin, Y. Xia, and G. M. Whitesides, “Soft lithography for micro- and nanoscale patterning.,” *Nat. Protoc.*, vol. 5, no. 3, pp. 491–502, Mar. 2010.

[85] P. Nagpal, N. C. Lindquist, S.-H. Oh, and D. J. Norris, “Ultrasmooth Patterned Metals for Plasmonics and Metamaterials,” *Science*, vol. 325, no. 5940, pp. 594–597, Jul. 2009.

[86] R. Nicolas, G. Lévêque, J. Marae-Djouda, G. Montay, Y. Madi, J. Plain, Z. Herro, M. Kazan, P. M. Adam, and T. Maurer, “Plasmonic mode interferences and Fano resonances in Metal-Insulator- Metal nanostructured interface,” *Sci. Rep.*, vol. 5, no. September, pp. 1–11, 2015.

[87] M. F. Limonov, M. V. Rybin, A. N. Poddubny, and Y. S. Kivshar, “Fano resonances in photonics,” *Nat. Photonics*, vol. 11, no. 9, pp. 543–554, 2017.

[88] G. D’Aguanno, N. Mattiucci, M. J. Bloemer, D. de Ceglia, M. A. Vincenti, and A. Alù, “Transmission resonances in plasmonic metallic gratings,” *J. Opt. Soc. Am. B*, vol. 28, no. 2, p. 253, 2011.

[89] A. Lovera, B. Gallinet, P. Nordlander, and O. J. F. Martin, “Mechanisms of fano resonances in coupled plasmonic systems,” *ACS Nano*, vol. 7, no. 5, pp. 4527–4536, 2013.

[90] J. A. Schuller, S. Karaveli, T. Schiros, K. He, S. Yang, I. Kymissis, J. Shan, and R. Zia, “Orientation of luminescent excitons in layered nanomaterials,” *Nat. Nanotechnol.*, vol. 8, no. 4, pp. 271–276, Apr. 2013.

[91] R. Scott, J. Heckmann, A. V Prudnikau, A. Antanovich, A. Mikhailov, N. Owschimikow, M. Artemyev, J. I. Climente, U. Woggon, N. B. Grosse, and A. W. Achtstein, “Directed emission of CdSe nanoplatelets originating from strongly anisotropic 2D electronic structure,” *Nat. Nanotechnol.*, vol. 12, no. 12, pp. 1155–1160, 2017.

[92] L. Novotny and B. Hecht, *Principles of Nano-Optics*. New York, NY: Cambridge University Press, 2006.

[93] D. Zhang, R. Badugu, Y. Chen, S. Yu, P. Yao, P. Wang, H. Ming, and J. R. Lakowicz, “Back focal plane imaging of directional emission from dye molecules coupled to one-dimensional photonic crystals,” *Nanotechnology*, vol. 25, no. 14, p. 145202, Apr. 2014.

[94] M. G. Debije and P. P. C. Verbunt, “Thirty years of luminescent solar concentrator research: Solar energy for the built environment,” *Adv. Energy Mater.*, vol. 2, no. 1, pp. 12–35, 2012.

[95] M. J. Currie, J. K. Mapel, T. D. Heidel, S. Goffri, and M. A. Baldo, “High-Efficiency Organic Solar Concentrators for Photovoltaics,” *Science (80-.).*, vol. 321, no. 5886, pp. 226–228, Jul. 2008.

[96] H. Li, K. Wu, J. Lim, H. J. Song, and V. I. Klimov, “Doctor-blade deposition of quantum dots onto standard window glass for low-loss large-area luminescent solar concentrators,” *Nat. Energy*, vol. 1, no. 12, 2016.

[97] F. Meinardi, H. McDaniel, F. Carulli, A. Colombo, K. A. Velizhanin, N. S.

Makarov, R. Simonutti, V. I. Klimov, and S. Brovelli, “Highly efficient large-area colourless luminescent solar concentrators using heavy-metal-free colloidal quantum dots,” *Nat. Nanotechnol.*, vol. 10, no. 10, pp. 878–885, 2015.

[98] K. E. Knowles, T. B. Kilburn, D. G. Alzate, S. McDowall, and D. R. Gamelin, “Bright CuInS2/CdS nanocrystal phosphors for high-gain full-spectrum luminescent solar concentrators,” *Chem. Commun.*, vol. 51, no. 44, pp. 9129–9132, 2015.

[99] J. Bomm, A. Büchtemann, A. J. Chatten, R. Bose, D. J. Farrell, N. L. A. Chan, Y. Xiao, L. H. Slooff, T. Meyer, A. Meyer, W. G. J. H. M. Van Sark, and R. Koole, “Fabrication and full characterization of state-of-the-art quantum dot luminescent solar concentrators,” *Sol. Energy Mater. Sol. Cells*, vol. 95, no. 8, pp. 2087–2094, 2011.

[100] C. S. Erickson, L. R. Bradshaw, S. McDowall, J. D. Gilbertson, D. R. Gamelin, and D. L. Patrick, “Zero-reabsorption doped-nanocrystal luminescent solar concentrators -SI,” *ACS Nano*, vol. 8, no. 4, pp. 3461–3467, 2014.

[101] I. Coropceanu and M. G. Bawendi, “Core/shell quantum dot based luminescent solar concentrators with reduced reabsorption and enhanced efficiency,” *Nano Lett.*, vol. 14, no. 7, pp. 4097–4101, 2014.

[102] N. D. Bronstein, Y. Yao, L. Xu, E. O’Brien, A. S. Powers, V. E. Ferry, A. P. Alivisatos, and R. G. Nuzzo, “Quantum Dot Luminescent Concentrator Cavity Exhibiting 30-fold Concentration,” *ACS Photonics*, vol. 2, no. 11, pp. 1576–1583, 2015.

[103] R. W. Meulenberg, T. van Buuren, K. M. Hanif, T. M. Willey, G. F. Strouse, and L. J. Terminello, “Structure and Composition of Cu-Doped CdSe Nanocrystals Using Soft X-ray Absorption Spectroscopy,” *Nano Lett.*, vol. 4, no. 11, pp. 2277–2285, 2004.

[104] A. H. Khan, A. Dalui, S. Mukherjee, C. U. Segre, D. D. Sarma, and S. Acharya, “Efficient Solid-State Light-Emitting CuCdS Nanocrystals Synthesized in Air,”

Angew. Chemie Int. Ed., vol. 54, pp. 2643–2648, Jan. 2015.

[105] A. Tang, L. Yi, W. Han, F. Teng, Y. Wang, Y. Hou, and M. Gao, "Synthesis, optical properties, and superlattice structure of Cu(I)-doped CdS nanocrystals," *Appl. Phys. Lett.*, vol. 97, no. 3, p. 033112, 2010.

[106] S. Jana, B. B. Srivastava, and N. Pradhan, "Correlation of dopant states and host bandgap in dual-doped semiconductor nanocrystals," *J. Phys. Chem. Lett.*, vol. 2, no. 14, pp. 1747–1752, 2011.

[107] W. Zhang, Q. Lou, W. Ji, J. Zhao, and X. Zhong, "Color-tunable highly bright photoluminescence of cadmium-free cu-doped Zn-In-S nanocrystals and electroluminescence," *Chem. Mater.*, vol. 26, no. 2, pp. 1204–1212, 2014.

[108] G. K. Grandhi, R. Tomar, and R. Viswanatha, "Study of surface and bulk electronic structure of II-VI semiconductor nanocrystals using Cu as a nanosensor," *ACS Nano*, vol. 6, no. 11, pp. 9751–9763, 2012.

[109] K. E. Knowles, K. H. Hartstein, T. B. Kilburn, A. Marchioro, H. D. Nelson, P. J. Whitham, and D. R. Gamelin, "Luminescent Colloidal Semiconductor Nanocrystals Containing Copper: Synthesis, Photophysics, and Applications," *Chem. Rev.*, vol. 116, no. 18, pp. 10820–10851, Sep. 2016.

[110] J. Liu, Q. Zhao, J.-L. Liu, Y.-S. Wu, Y. Cheng, M.-W. Ji, H.-M. Qian, W.-C. Hao, L.-J. Zhang, X.-J. Wei, S.-G. Wang, J.-T. Zhang, Y. Du, S.-X. Dou, and H.-S. Zhu, "Heterovalent-Doping-Enabled Efficient Dopant Luminescence and Controllable Electronic Impurity Via a New Strategy of Preparing II–VI Nanocrystals," *Adv. Mater.*, vol. 27, no. 17, pp. 2753–2761, 2015.

[111] A. Pandey, S. Brovelli, R. Viswanatha, L. Li, J. M. Pietryga, V. I. Klimov, and S. A. Crooker, "Long-lived photoinduced magnetization in copper-doped ZnSe–CdSe core–shell nanocrystals," *Nat. Nanotechnol.*, vol. 7, no. 12, pp. 792–797, Dec. 2012.

[112] J. W. Stouwdam and R. a J. Janssen, "Electroluminescent Cu-doped CdS

Quantum Dots," *Adv. Mater.*, vol. 21, no. 28, pp. 2916–2920, 2009.

[113] B. B. Srivastava, S. Jana, and N. Pradhan, "Doping Cu in semiconductor nanocrystals: Some old and some new physical insights," *J. Am. Chem. Soc.*, vol. 133, no. 4, pp. 1007–1015, 2011.

[114] R. Xie and X. Peng, "Synthesis of Cu-doped InP nanocrystals (d-dots) with ZnSe diffusion barrier as efficient and color-tunable NIR emitters," *J. Am. Chem. Soc.*, vol. 131, no. 30, pp. 10645–10651, 2009.

[115] A. Sahu, M. S. Kang, A. Kompch, C. Notthoff, A. W. Wills, D. Deng, M. Winterer, C. D. Frisbie, and D. J. Norris, "Electronic impurity doping in CdSe nanocrystals," *Nano Lett.*, vol. 12, no. 5, pp. 2587–2594, 2012.

[116] S. C. Erwin, L. Zu, M. I. Haftel, A. L. Efros, T. a Kennedy, and D. J. Norris, "Doping semiconductor nanocrystals," *Nature*, vol. 436, no. 7047, pp. 91–94, 2005.

[117] D. Mocatta, G. Cohen, J. Schattner, O. Millo, E. Rabani, and U. Banin, "Heavily doped semiconductor nanocrystal quantum dots.," *Science*, vol. 332, no. 6025, pp. 77–81, 2011.

[118] P. N. Tananaev, S. G. Dorofeev, R. B. Vasil'ev, and T. A. Kuznetsova, "Preparation of copper-doped CdSe nanocrystals," *Inorg. Mater.*, vol. 45, no. 4, pp. 347–351, 2009.

[119] A. M. Jawaid, S. Chattopadhyay, D. J. Wink, L. E. Page, and P. T. Snee, "Cluster-seeded synthesis of doped CdSe:Cu4 quantum dots," *ACS Nano*, vol. 7, no. 4, pp. 3190–3197, 2013.

[120] S. Ithurria, M. D. Tessier, B. Mahler, R. P. S. M. Lobo, B. Dubertret, and A. L. Efros, "Colloidal nanoplatelets with two-dimensional electronic structure.," *Nat. Mater.*, vol. 10, no. 12, pp. 936–41, Dec. 2011.

[121] M. Olutas, B. Guzelturk, Y. Kelestemur, A. Yeltik, S. Delikanli, and H. V. Demir,

"Lateral Size-Dependent Spontaneous and Stimulated Emission Properties in Colloidal CdSe Nanoplatelets," *ACS Nano*, vol. 9, no. 5, pp. 5041–5050, 2015.

[122] A. Yeltik, S. Delikanli, M. Olutas, Y. Kelestemur, B. Guzelturk, and H. V. Demir, "Experimental Determination of the Absorption Cross-Section and Molar Extinction Coefficient of Colloidal CdSe Nanoplatelets," *J. Phys. Chem. C*, vol. 119, p. 26768−26775, 2015.

[123] B. Guzelturk, Y. Kelestemur, M. Olutas, S. Delikanli, and H. V. Demir, "Amplified Spontaneous Emission and Lasing in Colloidal Nanoplatelets," *ACS Nano*, vol. 8, no. 7, pp. 6599–6605, 2014.

[124] C. She, I. Fedin, D. S. Dolzhnikov, P. D. Dahlberg, G. S. Engel, R. D. Schaller, and D. V Talapin, "Red , Yellow , Green , and Blue Amplified Spontaneous Emission and Lasing Using Colloidal CdSe Nanoplatelets," *ACS Nano*, vol. 9, no. (10), pp. 9475–9485, 2015.

[125] D. Chen, Y. Gao, Y. Chen, Y. Ren, and X. Peng, "Structure Identification of Two-Dimensional Colloidal Semiconductor Nanocrystals with Atomic Flat Basal Planes," *Nano Lett.*, vol. 15, no. 7, pp. 4477–4482, 2015.

[126] M. Sharma, K. Gungor, A. Yeltik, M. Olutas, B. Guzelturk, Y. Kelestemur, T. Erdem, S. Delikanli, J. R. McBride, and H. V. Demir, "Near-Unity Emitting Copper-Doped Colloidal Semiconductor Quantum Wells for Luminescent Solar Concentrators," *Adv. Mater.*, vol. 29, no. 30, p. 1700821, Aug. 2017.

[127] A. Radi, D. Pradhan, Y. Sohn, and K. T. Leung, "Nanoscale shape and size control of cubic, cuboctahedral, and octahedral Cu-Cu2O core-shell nanoparticles on Si(100) by one-step, templateless, capping-agent-free electrodeposition.," *ACS Nano*, vol. 4, no. 3, pp. 1553–60, 2010.

[128] Y. Wang, M. Zhukovskyi, P. Tongying, Y. Tian, and M. Kuno, "Synthesis of Ultrathin and Thickness-Controlled Cu 2– x Se Nanosheets via Cation Exchange," *J. Phys. Chem. Lett.*, vol. 5, no. 21, pp. 3608–3613, 2014.

[129] P. J. Whitham, K. E. Knowles, P. J. Reid, and D. R. Gamelin, "Photoluminescence Blinking and Reversible Electron Trapping in Copper-Doped CdSe Nanocrystals," *Nano Lett.*, vol. 15, pp. 4045–4051, 2015.

[130] K. E. Knowles, H. D. Nelson, T. B. Kilburn, and D. R. Gamelin, "Singlet–Triplet Splittings in the Luminescent Excited States of Colloidal Cu+:CdSe, Cu+:InP, and CuInS2 Nanocrystals: Charge-Transfer Configurations and Self-Trapped Excitons," *J. Am. Chem. Soc.*, vol. 137, no. 40, pp. 13138–13147, 2015.

[131] A. Suzuki and S. Shionoya, "Mechanism of the Green-Copper Luminescence in ZnS Crystals. I. Direct Evidence for the Pair Emission Mechanism," *J. Phys. Soc. Jpn.*, vol. 31, no. 5, pp. 1455–1461, 1971.

[132] J. T. Wright, K. Forsythe, J. Hutchins, and R. W. Meulenberg, "Implications of orbital hybridization on the electronic properties of doped quantum dots: the case of Cu:CdSe," *Nanoscale*, vol. 8, no. 17, pp. 9417–9424, 2016.

[133] L. Yang, K. E. Knowles, A. Gopalan, K. E. Hughes, M. C. James, and D. R. Gamelin, "One-Pot Synthesis of Monodisperse Colloidal Copper-Doped CdSe Nanocrystals Mediated by Ligand-Copper Interactions," *Chem. Mater.*, vol. 28, no. 20, pp. 7375–7384, 2016.

[134] S. Ithurria and D. V. Talapin, "Colloidal atomic layer deposition (c-ALD) using self-limiting reactions at nanocrystal surface coupled to phase transfer between polar and nonpolar media," *J. Am. Chem. Soc.*, vol. 134, no. 45, pp. 18585–18590, 2012.

[135] A. A. Earp, G. B. Smith, P. D. Swift, and J. Franklin, "Maximising the light output of a Luminescent Solar Concentrator," *Sol. Energy*, vol. 76, no. 6, pp. 655–667, 2004.

[136] H. Abitan, H. Bohr, and P. Buchhave, "Correction to the Beer-Lambert-Bouguer law for optical absorption.," *Appl. Opt.*, vol. 47, no. 29, pp. 5354–5357, 2008.

[137] H. Zhao, D. Benetti, L. Jin, Y. Zhou, F. Rosei, and A. Vomiero, "Absorption

Enhancement in ‘Giant’ Core/Alloyed-Shell Quantum Dots for Luminescent Solar Concentrator,” *Small*, vol. 12, no. 38, pp. 5354–5365, Oct. 2016.